

Quantum Cascade Lasers for Mid-Infrared Chemical Sensing

A Thesis

Presented to

The Academic Faculty

by

Christy Charlton

In Partial Fullfillment

of the Requirements for the Degree

Doctor of Philosophy in Chemistry

Georgia Institute of Technology

December, 2005

Quantum Cascade Lasers for Mid-Infrared Chemical Sensing

Approved by:

Dr. Boris Mizaikoff, Advisor
School of Chemistry and Biochemistry
Georgia Institute of Technology

Dr. Peter Hesketh
School of Mechanical Engineering
Georgia Institute of Technology

Dr. Jiri Janata
School of Chemistry and Biochemistry
Georgia Institute of Technology

Dr. Thomas Orlando
School of Chemistry and Biochemistry
Georgia Institute of Technology

Dr. Mohan Srinivasarao
School of Polymer, Textile, and Fiber
Engineering and
School of Chemistry and Biochemistry
Georgia Institute of Technology

Date Approved: November 10, 2005

ACKNOWLEDGEMENTS

I am deeply grateful to my supervisor Prof. Boris Mizaikoff for the endless opportunities provided to me throughout my Ph.D. studies and the endless ideas and enthusiasm that have been sent my way. He and Dr. Christine Kranz have put together an amazing team that has been great to work with. Thanks to past and present members of the ASL group here at Georgia Tech for their help and support throughout the work. A special thanks goes out to Nicola Menegazzo for his endless effort to help with anything and everything needed in the group.

This work has been a collaborative effort and I wish to thank all those who helped make it possible. The Optical Sensors Laboratory in the National Center for Sensor Research at Dublin City University was my host during research visit funded by the National Science Foundation. Special thanks are extended to Prof. Brian MacCraith, Kieran O'Dwyer, John Donohue, Robert Copperwhite, Dr. Conor Burke, and Nigel Kent. GaAs single-mode waveguides have been developed in collaboration with Prof. Jerome Faist and Dr. Marcella Giovanninni at the University of Neuchatel. I am grateful to everyone at OmniGuide Communications and particularly Burak Temelkuran and Gregor Dellemann for providing a photonic bandgap hollow waveguide. Prof. Abraham Katzir from Tel Aviv University for keeping us supplied with silver halide fibers and Prof. Nathan Croitoru, also from Tel Aviv University, for silica hollow waveguides.

Thanks to Dr. Lubos Hvozدارa for helping to begin this research project and for his continued support and the answers to the many questions I have posed to him over the years.

Personal support has also been instrumental in this work and I am grateful to the many friends and family members who have provided this in abundance. Thank you to Gozde Guler, Chiko Umeweni, and Jose Gonzalez for all the nights out (especially at our cinema) and the laughs. Thanks to my mom, Debbie, and to Billy for giving me somewhere I love coming home to and to Bill and Sharon for all of their support. Thank-you to John for always “being there” and for giving me something to work towards in finishing it all up.

TABLE OF CONTENTS

Acknowledgements	iii
List of Tables	xi
List of Figures	xii
List of Abbreviations	xvii
Summary	xix
1. Introduction	1
Thesis Goal	1
Original Contributions of this thesis	1
Chapter Overview	1
1.1 Optical Sensors	3
1.1.1 History	3
1.1.2 Infrared Optical Sensors	4
1.2 Infrared Lasers	6
1.2.1 History of Infrared Radiation	6
1.2.2 Principle of Lasers	7
1.2.3 Infrared Laser Coverage	8
1.2.4 Quantum Cascade Lasers	12
References	13

2. Quantum Cascade Lasers	15
2.1 Operation Principle	15
2.1.1 Quantum Heterostructure	15
2.1.2 QCL Composition	17
2.1.3 Fabry-Perot and Distributed Feedback Lasers	18
2.2 History	19
2.2.1 Operation Temperature	19
2.2.2 Continuous Wave Operation	20
2.2.3 Distributed Feedback QCLs	21
2.2.4 High Power Output	21
2.2.5 Wavelength Range	22
2.2.6 Novel QCL Structures	23
2.3 Availability of QCLs	25
2.3.1 Commercial Availability	25
2.4 QCL Characterization	27
2.4.1 Response Curve	27
2.4.2 Temperature Tuning	28
2.4.3 Pulse Shape Behavior	30
2.4.4 Beam Output Characteristics	32
2.5 System Electronics	33
2.5.1 Alpes Lasers Components	33
2.5.2 Detectors	35
2.5.3 Data Acquisition	36

References	37
3. Absorption-Based Optical sensors	40
3.1 Fundamentals of Transmission Absorption Spectroscopy	40
3.1.1 Lambert-Beer Law	41
3.1.2 Lambert-Beer Law in Chemical Sensing	42
3.2 Fundamentals of Evanescent Field Absorption Spectroscopy	44
3.2.1 Total Internal Reflection	44
3.2.2 Total Internal Reflection in Chemical Sensing	45
3.2.3 IR Evanescent Field Sensing Platforms	48
3.2.4 Evanescent Field Dependence on Waveguide Geometry	48
References	52
4. QCL-Based Gas Phase Sensing	53
4.1 Motivation	53
4.1.1 Breath Analysis	53
4.1.2 Atmospheric Monitoring	54
4.2 State-of-the-art in Laser-Based Gas Sensing	57
4.2.1 Multipass Transmission Absorption Spectroscopy	57
4.2.2 Photoacoustic Spectroscopy	57
4.2.3 Cavity Ring-down Spectroscopy	58
4.2.4 Integrated Cavity Output Spectroscopy	58
4.2.5 Differential Absorption LIDAR	59

4.2.6 Quantum Cascade Lasers in Gas Sensing	59
4.3 Hollow Waveguides	61
4.3.1 History	61
4.3.2 Photonic Bandgap Hollow Waveguides	64
4.3.3 Losses in Hollow Waveguides	67
4.3.4 Hollow Waveguides in IR Gas Sensing	68
4.4 Silica Hollow Waveguide Sensing System	71
4.4.1 Experimental	71
4.4.2 Results	74
4.5 Comparison of Bending Losses	80
4.5.1 Experimental	80
4.5.2 Results	81
4.6 Photonic Bandgap Hollow Waveguide Sensing System	83
4.6.1 Experimental	83
4.6.2 Results	87
4.7 Outlook	91
4.7.1 Long Pathlength Coiled PBG HWG	91
4.7.2 Miniaturization	92
4.8 Conclusion	95
References	96
5. Planar IR Waveguide Design	103
5.1 Beam Propagation Simulations	103

5.1.1 BPM Method Setup	103
5.1.2 BPM Results	108
5.1.3 Optimizing the Signal-to-Noise Ratio	116
5.2 Silver Halide Planar Waveguides	117
5.3 GaAs Planar Waveguides	118
5.4 Conclusion	120
5.5 Outlook – Waveguide Coupling	121
5.5.1 Theory on Blazed Angle Gratings	121
5.5.2 Hot Embossed Silver Halide Gratings	122
5.5.3 FIB Milled GaAs Gratings	124
6. QCL-Based Liquid Phase Sensing	128
6.1 Motivation	128
6.1.1 Environmental	128
6.1.2 Biological	129
6.2 State-of-the-art	131
6.2.1 ATR Waveguide Development	131
6.2.2 Lasers in Liquid Sensing	131
6.2.3 QCLs in Liquid Sensing	132
6.3 IR Solid Core Fibers	133
6.3.1 Silver Halide Fibers	133
6.4 Planar Silver Halide Waveguide Sensing Systems	135
6.4.1 Waveguide Preparation	135

6.4.2 Urea Experiments	136
6.4.3 Acetic Anhydride Experiments	143
6.4.4 Results	151
6.5 Planar Single-Mode GaAs Waveguides	154
6.5.1 Waveguide Preparation	154
6.5.2 Experimental	158
6.5.3 Results	159
6.6 Conclusions and Outlook	167
References	169
7. Conclusions and Outlook	175
7.1 Gas Sensing Summary	175
7.2 Liquid Sensing Summary	176
7.3 Outlook for QCLs in Chemical Sensing	177
Appendix A: Matlab Programs for BPM Simulations	179

LIST OF TABLES

Table 2-1:	Detector Specifications.	35
Table 4-1:	Selected compounds relevant to breath analysis.	54
Table 4-2:	Selected target gases for atmospheric monitoring.	55
Table 4-3:	Selected milestones in the development of HWG technology.	63
Table 4-4:	Comparison of bending results.	81
Table 6-1:	Absorption band positions for protein conformation.	130
Table 6-2:	Infrared fiber materials.	133

LIST OF FIGURES

Figure 1-1:	Superposition of HITRAN spectra for water vapor and CO ₂ .	4
Figure 1-2:	Laser operation principle.	8
Figure 1-3:	Spectral coverage of mid-infrared lasers.	12
Figure 2-1:	Operation principle of QCLs.	16
Figure 2-2:	QCL composition.	17
Figure 2-3:	Response curve of laser s1537 emitting at 974 cm ⁻¹ (10.3 μm).	27
Figure 2-4:	Temperature tuning for laser s1869.	28
Figure 2-5:	Temperature tuning for laser s1537.	29
Figure 2-6:	Driving pulse shape.	30
Figure 2-7:	QCL output with increasing pulse width.	31
Figure 2-8:	Block diagram of Alpes Laser QCL driving electronics.	33
Figure 2-9:	Laser housing electronics.	34
Figure 3-1:	Transmission Absorption Measurement Setup.	40
Figure 3-2:	Total Internal Reflection (TIR) shown from a ray optics perspective (top) and a modal perspective (bottom).	44
Figure 3-3:	Penetration depth as a function of wavelength per incoupling angle for a waveguide with refractive index of 2.1 and a refractive index of 1 for the surrounding medium.	46
Figure 3-4:	Penetration depth as a function of wavelength by refractive index 2.1 (AgX) and 3.3 (GaAs).	47
Figure 4-1:	Photonic crystal structures with periodicity in 1-D (left), 2-D (center), and 3-D (right).	64

Figure 4-2:	Schematic PBG HWG cross sections of (a) honeycomb type structures (light is confined to the central defect hole) and (b) omnidirectional guide (light is confined by cylindrical 1D photonic crystal layers).	65
Figure 4-3:	Transmission spectrum of a commercially produced OmniGuide Fiber designed to transmit light at 10.6 μm with OmniGuide schematic (inset). (Image courtesy of OmniGuide Communications Inc.)	66
Figure 4-4:	Glass HWG Cross Section.	71
Figure 4-5:	HWG gas cells.	72
Figure 4-6:	Experimental setup.	73
Figure 4-7:	FTIR spectra of emission (curve a) and ethyl chloride absorption (curve b) band overlap.	75
Figure 4-8:	Damping of laser signal in presence of analyte for ethyl chloride in air concentration a) 0 ppm, b) 1 ppm, c) 5 ppm, d) 10 ppm, e) 15 ppm, f) 20 ppm.	76
Figure 4-9:	Percentage signal damping as a function of concentration of ethyl chloride in air present in the waveguide.	77
Figure 4-10:	Experimental setup for the comparison of bending losses.	80
Figure 4-11:	FT-IR spectra of the overlap between ethyl chloride absorption band (top) and laser emission band (bottom) with the OmniGuide fiber transmission range shown in yellow.	83
Figure 4-12:	Microscope image of hollow waveguide cross sections with 10 X magnification of (left) OmniGuide fiber and (right) silica hollow waveguide.	85
Figure 4-13:	Experimental setup.	85
Figure 4-14:	Schematic of an exponential dilution flask.	87
Figure 4-15:	System response curve to an exponential dilution series.	88
Figure 4-16:	System noise level (red line) relative to signal change with time.	89
Figure 4-17:	Fiber-HWG-Fiber coupling with system signal throughput.	92

Figure 4-18:	Gold coated microchannel waveguides 500 μm wide by 500 μm fabricated into epoxy resin block substrates for testing losses in folded (left) and curved (center) waveguides. (right) Channel roughness of these first prototypes.	93
Figure 5-1:	Refractive index profile for BPM simulations.	104
Figure 5-2:	Waveguide with a thickness, which does not support any mode.	105
Figure 5-3:	Waveguide with a thickness supporting a single mode.	106
Figure 5-4:	Waveguide with a thickness supporting multiple modes.	107
Figure 5-5:	Integration regions for evanescent field intensity calculation of planar waveguides.	108
Figure 5-6:	Evanescent field intensity as a function of waveguide thickness for various wavelengths of light.	109
Figure 5-7:	Dependence of the optimum waveguide thickness on the wavelength of light.	109
Figure 5-8:	Maximum evanescent field intensity dependence on the wavelength of light.	110
Figure 5-9:	In-coupling angle.	111
Figure 5-10:	3-D plot of intensity in the evanescent field as a function of waveguide thickness and source tilt.	111
Figure 5-11:	Intensity in the evanescent field as a function of the waveguide thickness for various source tilt angles.	112
Figure 5-12:	Maximum evanescent intensity dependence on source tilt angle.	113
Figure 5-13:	Optimum waveguide thickness by refractive index.	114
Figure 5-14:	Dependence of the optimum waveguide thickness on the waveguide refractive index.	115
Figure 5-15:	Dependence of the maximum evanescent field intensity on the waveguide refractive index.	115
Figure 5-16:	Calculated mode profile for GaAs thin film waveguides.	118
Figure 5-17:	Blazed angle grating profile.	121

Figure 5-18:	Optical profile of grating at AgX waveguide surface.	123
Figure 5-19:	X-direction period profile of grating at the AgX fiber surface.	124
Figure 5-20:	Bitmap pattern for FIB milling of blazed angle grating.	125
Figure 5-21:	FIB milled grating structure on GaAs.	126
Figure 5-22:	Cross sectional view of FIB milled grating structure on GaAs.	126
Figure 6-1:	Planar silver halides with a thickness of 100 μm (top), 300 μm (middle), and a cylindrical fiber with diameter of 700 μm .	135
Figure 6-2:	Planar silver halide fiber end facet after polishing with a) 3 μm , b) 1 μm , and c) 0.5 μm diamond slurries.	136
Figure 6-3:	FTIR PWG experimental setup.	137
Figure 6-4:	QCL-PWG experimental setup.	138
Figure 6-5:	Bare AgX fiber surface (left) and urea crystals at AgX waveguide surface after deposition and evaporation of 30 μL and 40 μL of methanol-urea solution, respectively.	139
Figure 6-6:	FT-IR urea band increases with increasing deposition of material.	140
Figure 6-7:	Overlap of QCL emission and urea absorption frequency.	141
Figure 6-8:	QCL pulse damping due to urea absorption.	142
Figure 6-9:	Response curve to urea surface deposition.	143
Figure 6-10:	Acetic anhydride QCL experimental setup.	144
Figure 6-11:	Acetic anhydride deposition at the waveguide surface.	145
Figure 6-12:	FT-IR evanescent absorption spectra for acetic anhydride.	146
Figure 6-13:	Overlap of QCL emission and acetic anhydride absorption band.	147
Figure 6-14:	Transmission cell measurements.	148
Figure 6-15:	QCL Damping due to acetic anhydride absorption due to: from the top 0, 0.01, 0.1, 0.2, and 1 μL droplets at the waveguide surface.	149

Figure 6-16:	QCL response curve for acetic anhydride surface deposition.	150
Figure 6-17:	Coupling efficiency.	152
Figure 6-18:	QCL damping by different coupling methods. The scale for these two sets of curves does not correspond; and they have been placed on the same graph only for comparison.	153
Figure 6-19:	Waveguide composition.	155
Figure 6-20:	GaAs thin-film strip waveguides with silicon nitride protective overlayer (right), and without (left).	156
Figure 6-21:	SEM images of a GaAs waveguide end facet.	157
Figure 6-22:	Experimental setup of QCL coupled to GaAs thin-film waveguide.	159
Figure 6-23:	FTIR single beam spectra through GaAs thin-film waveguides showing reference without waveguide (top), waveguide without silicon nitride overlayer (middle) and waveguide with silicon nitride overlayer (bottom).	160
Figure 6-24:	FT-IR coupled to GaAs thin-film waveguides absorption spectra for bare waveguide (dark blue), 5 μ L drop of acetic anhydride on waveguide surface (light blue), 10 μ L drop of acetic anhydride on waveguide surface (green) and surface drops evaporated (red).	161
Figure 6-25:	System response for GaAs and AgX waveguides coupled to QCL.	163
Figure 6-26:	Mode profile for GaAs and AgX waveguides.	165

LIST OF ABBREVIATIONS

AgX	Silver Halide
ATR	Attenuated Total Reflection
BPM	Beam Propagation Method
CRD	Cavity Ring-down
Cw	Continuous Wave
dB	Decibel
DFB	Distributed Feedback
DFG	Difference Frequency Generation
DIAL	Differential Absorption LIDAR
FIB	Focused Ion Beam
FT-IR	Fourier Transform Infrared
GaAs	Gallium Arsenide
HPLC	High Performance Liquid Chromatography
HWG	Hollow Waveguide
ICOS	Integrated Cavity Output Spectroscopy
LIDAR	Light Detection and Ranging
LED	Light Emitting Diode
LO	Longitudinal-Optic
LOD	Limit of Detection
MBE	Molecular Beam Epitaxy

MCT	Mercury-Cadmium-Telluride
MIR	Mid-Infrared
NIR	Near-Infrared
OAPM	Off-Axis Parabolic Mirror
OPO	Optical Parametric Oscillator
PBG	Photonic Bandgap
PWG	Planar Waveguide
ppb	Parts per billion
ppm	Parts per million
ppt	Part per trillion
QCL	Quantum Cascade Laser
SEM	Scanning Electron Microscopy
TIR	Total Internal Reflection
TDL	Tunable Diode Laser
TM	Transverse Magnetic
TSE	Transmissible Spongiform Encephalopathies
UV	Ultraviolet
Vis	Visible

SUMMARY

The mid-infrared (MIR) spectral range (2-20 μm) is particularly useful for chemical sensing due to the excitation of fundamental rotational and vibrational modes. In the ‘fingerprint region’ (10-20 μm), most organic analytes have unique absorption patterns; absorption measurements in this region provide molecule-specific information with high sensitivity.

Quantum cascade lasers (QCLs) present an ideal light source for (MIR) chemical sensing due to their narrow linewidth, high spectral density, compact size, and ease of fabrication of nearly any MIR wavelength. As the emission wavelength is dependent on layer size within the heterostructure rather than material composition, various wavelengths in the MIR can be achieved through bandstructure engineering.

High sensitivity measurements have been achieved in both gas and liquid phase by developing integrated sensing systems. The laser emission frequency is selected to match a strong absorption feature for the analyte of interest where no other interfering bands are located. A waveguide is then developed to fit the application and wavelength used.

Gas sensing applications incorporate silica hollow waveguides (HWG) and an OmniGuide fiber which consists of a one dimensional photonic crystal wrapped into a cylindrical shape to create a photonic bandgap HWG. Analyte gas is injected into the hollow core allowing the HWG or OmniGuide to serve simultaneously as a waveguide

and miniaturized gas cell. Sensitivities of parts per billion (ppb) are achieved with a response time of 8 s and a sample volume of approximately 1 mL.

Liquid sensing is achieved via evanescent wave measurements with novel planar waveguides of silver halide (AgX) and gallium arsenide (GaAs). GaAs waveguides developed in this work are grown via molecular beam epitaxy on a GaAs wafer substrate and have a thickness on the order of the wavelength of light to achieve a single-mode waveguide, providing a significant improvement in evanescent field strength over conventional multimode fibers or attenuated total reflection elements used in infrared spectroscopy. Liquid samples of μL volume at the waveguide surfaces are detected and waveguide mode calculations indicate high evanescent intensity at the waveguide surface, which leads to monolayer sensing applications.

QCLs have begun to be utilized as a light source in the MIR regime over the last decade. The next step in this field is the establishment of useful chemical and biological sensing applications, along with compact and highly integrated device platforms which take full advantage of this technology. The demonstrations of both gas and liquid phase MIR chemical sensing in this work advance the field towards finding key applications in medical, biological, environmental, and atmospheric measurements.

CHAPTER 1

INTRODUCTION

Thesis Objective: Development of devices which demonstrate the full potential of quantum cascade lasers for mid-infrared chemical sensing on miniaturized platforms.

Original contributions of this thesis:

- Demonstration of gas sensing inside a photonic bandgap waveguide (chapter 4)
- Demonstration of evanescent field measurements with quantum cascade lasers (chapter 6)
- Development and characterization of thin film single mode waveguides, for IR evanescent field sensing, deposited by molecular beam epitaxy (chapters 5 and 6)

Chapter 2 of this thesis will provide an overview on quantum cascade lasers (QCLs) including the history of their development, characterization of the lasers used in this thesis, and the electronics implemented for driving these lasers.

Chapter 3 focuses on the theory of absorption measurements including both transmission measurements based on the Lambert-Beer law and attenuated total reflection (ATR) measurements based on a modified Lambert-Beer law. Furthermore, opportunities for increasing the sensitivity of ATR measurements by alternative waveguide geometries are discussed.

Chapter 4 presents QCL gas sensing studies using transmission absorption spectroscopy inside miniaturized hollow waveguide gas cells. State-of-the-art mid-infrared (MIR) gas sensing is surveyed along with potential applications.

Chapter 5 discusses the design of planar waveguides with a view to improving sensitivity of evanescent field QCL liquid-phase sensing systems.

Chapter 6 presents QCL liquid sensing studies using ATR spectroscopy with planar waveguides. State-of-the-art MIR liquid sensing is surveyed, along with potential applications.

Chapter 7 provides summarized conclusions on the studies in this thesis and an outlook on the future potential of QCLs in the field of chemical sensing.

1.1 Optical Sensors

The field of chemical sensing can be divided into four main areas: thermal, mass, electrochemical, and optical sensors. Optical chemical sensors are based on the interaction between light and a chemical species causing a change in a property (amplitude, polarization, phase, or wavelength) of light. This work focuses strictly on optical chemical sensors, using changes in amplitude as the monitored property. The sensors developed in this work will exclusively utilize radiation in the mid-infrared region (MIR, wavelengths of 2.5 – 20 μm) of the electromagnetic spectrum.

1.1.1 History

Chemical sensors are devices capable of continuously monitoring a chemical or physical property without the need for additional processing step such as sample preparation. The field of chemical sensing emerged as a heavily-researched topic in the mid 1980's and has since been steadily gaining importance¹⁻⁴.

In general, chemical sensors comprise of four main components: the input interface, the transducer, the signal processing unit, and the output interface. The input interface of the sensor is exposed to the sample matrix of interest. A transducer then produces a detectable signal based on a molecular recognition event, which is subsequently processed and converted into the final output signal from the system.

1.1.2 Infrared Optical Sensors

Fundamental rotational and vibrational transitions in the mid-infrared (MIR) provide strong and molecular specific absorption bands, rendering infrared optical sensing both sensitive and selective. However, in order to achieve maximum selectivity, the analyte of interest should provide a characteristic absorption band which does not overlap with the absorptions of other compounds present in the sample.

For gas sensing applications in the MIR region, absorption from water vapor and CO₂ in air cause significant interference. Therefore, atmospheric windows free from absorbances of major atmospheric constituents provide ideal spectral sensing regimes. Figure 1-1 shows superimposed HITRAN⁵ spectra of water and CO₂ with atmospheric windows indicated in yellow.

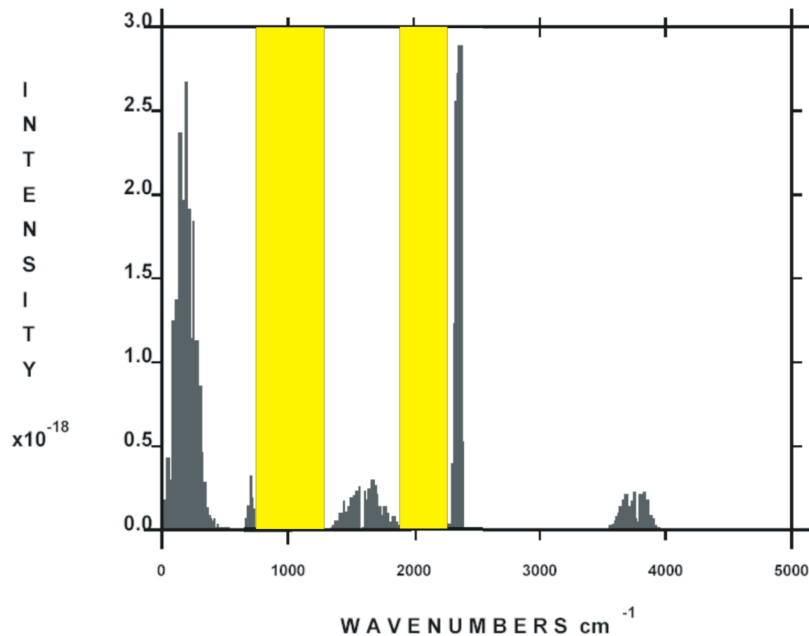


Figure 1-1: Superposition of HITRAN spectra for water vapor and CO₂.

In MIR liquid-phase sensing applications, the main interfering species is water with a broad absorption feature from 3000 to 4000 cm^{-1} (2.5 – 3.3 μm) due to stretching vibrations (ν_1 and ν_3) and a sharper band at approximately 1650 cm^{-1} (6 μm) due to bending vibrations (ν_2). As most applications, including biological and environmental sensing, involve aqueous matrices, the strong absorption of water is a limitation for conventional MIR sensing without chemical surface modification of the waveguide such as polymer enrichment layers.

Note about wavelengths and wavenumbers:

By convention, infrared wavelengths are typically reported in wavenumbers (cm^{-1}) for absorption spectra, and in units of length (μm) for the laser emission. As this work is a combination of these fields, wavelengths will be reported in both units for clarity.

1.2 Infrared Lasers

The disadvantage of working in the MIR is the limited availability of light sources, waveguide materials, and detectors in contrast to the visible or near IR regime, where the telecommunications industry has driven extensive technical development. The following section provides a summary of laser sources available at MIR wavelengths.

1.2.1 History of Infrared Radiation

Infrared radiation was discovered in 1800 by Fredrick William Herschel while investigating the heat produced by different colors of light resulting from sunlight passing through a glass prism. He found that the temperatures increased going from violet to red and decided to measure the region beyond red light, which he found to have an even higher temperature. Herschel had discovered what would eventually be known as infrared radiation, and with this discovery had shown that light existed beyond radiation visible to human optical perception.

The fundamentals of infrared spectroscopy were developed by Harrison Randall at the University of Michigan where, in 1915, a high resolution prism based spectrometer capable of measuring infrared spectra to a wavelength of 14 μm was constructed. The fundamental principle of infrared spectroscopy is that light in this spectral region excites rotations and vibrations in molecules. If these rotations and vibrations cause a net change in the dipole moment of the molecule, the frequency where resonant energy transfer occurs is absorbed. Due to the fundamental nature of the vibrational and rotational modes, molecules have strong and unique absorption patterns in the infrared, particularly

in the fingerprint region (8 to 20 μm) rendering IR sensing particularly sensitive and selective⁶.

Mid-infrared spectroscopy is typically performed with a broadband source such as a Nernst glower, globar, or incandescent wire utilizing an interferometer or grating to resolve the spectrum by wavelength. This provides the advantage of measuring the entire spectrum at once and gives a high selectivity for a specific compound. IR spectroscopic measurements can also be performed with a laser light source emitting a single wavelength or narrow wavelength band. Laser light sources provide a more intense output at their specific emission wavelength and thus potentially provide a higher sensitivity.

1.2.2 Principle of Lasers

The laser was invented in 1958 by Charles Townes and Arthur Schawlow⁷. “Laser” is an acronym for Light Amplification by Stimulated Emission of Radiation. Lasers produce an intense, coherent beam of light of a particular wavelength by exciting atoms or molecules in the cavity of the laser resulting in more atoms in the excited state than in the ground state creating population inversion. As a photon of energy corresponding to the bandgap (difference between the excited and ground states) strikes an excited atom, that atom releases a second photon matching the excitation photon in energy, phase, and direction as it returns to the ground state in a process called ‘stimulated emission’. Mirrors at each end of the cavity cause photons to bounce back and forth, thereby

amplifying the generated laser light over time producing a large amount of coherent radiation.

The operating principle of a conventional laser is depicted in Figure 1-2 below.

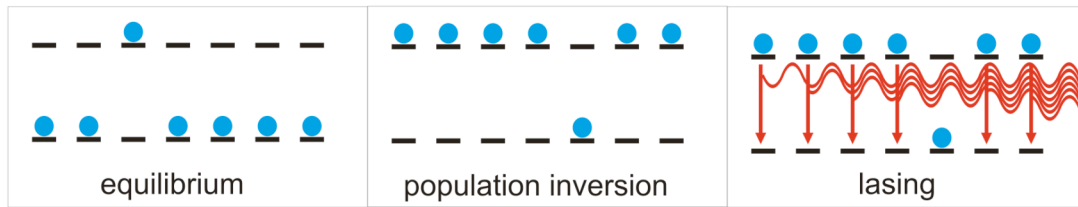


Figure 1-2: Laser operation principle.

In Figure 1-2, a scheme of the high and low energy level at equilibrium conditions is shown on the left. Initially, electrons are primarily populating the lower energy level. The middle scheme shows population inversion achieved by (usually optic or electronic) pumping of the laser, where the majority of the carriers are in an excited state enabling electrons to relax into the ground state, thus emitting their excess energy as photons. Lasing is depicted in the scheme at the right, where a carrier relaxes from the higher to the lower energy level releasing a photon and stimulating other carriers, thereby amplifying the radiation output.

1.2.3 Infrared Laser Coverage

The most popular IR laser is the CO₂ laser, which was first demonstrated in 1964 by Patel at Bell Labs⁸. Gas lasers operate by exciting a gas in a tube to a high-energy state using dc discharge power and N₂ gas as a pump⁹ creating population inversion. As the gas

returns to its ground state, a photon is released, which is reflected inside the tube by mirrors at each end of the cavity. Photons inside the gas tube stimulate emission from other molecules and light builds up until it is released as coherent radiation. Emission wavelengths of gas lasers are based on the transition energies available in the gas of choice.

CO₂ emission is tunable over the range of 9.2 – 10.8 μm based on the emission lines of CO₂ and is therefore not continuous unless operated at high gas pressures only available in pulsed mode.¹⁰ CO₂ lasers are capable of emitting continuous powers in the tens of kilowatts range.

Another commonly used MIR gas laser is the CO laser, which emits from 5 – 6 μm utilizing fundamental CO emissions, and can be extended to discrete lines at 2.7 μm using overtone vibrations¹¹. Typical output powers in the 5 – 6 μm range are in the hundreds of watts regime.

Difference frequency generation (DFG)¹² utilizes two laser light sources and a nonlinear medium to produce MIR radiation. The two sources combine in the nonlinear medium to produce a wavelength that is the difference of the pump and signal wavelength used for generation. The tunability of the generated MIR radiation is limited by the tunability of the pump and the signal source. The use of different pump and signal wavelengths and the choice of nonlinear medium with transparency at both input and output wavelengths enables DFG to be used across nearly the entire MIR band from 2 – 17 μm. The power

output of these systems depends on both the power of the pump laser and the conversion efficiency of the nonlinear medium. However, this technique requires extensive optical setups, limiting its utility in portable or miniaturized systems. DFG typically provides linewidths of approximately 1 MHz¹³.

Optical parametric oscillators (OPO)¹⁴ operate as a reverse of the DFG process. Here, a pump beam enters a nonlinear optic crystal and decays into two separate wavelengths whose sum equals that of the pump. The key to an OPO is achieving a phase matching condition through a periodic structure in the nonlinear optic material. By changing the period by temperature or crystal angle, the ratio of the output wavelengths can be altered providing wavelength tunability. As in DFG, the choice of the input wavelength and crystal transparency allows wavelengths over the entire MIR from 2 – 20 μm to be generated. Power outputs of up to 10 W (average power) are possible with typical values of 1 kW peak or 1 W average power depending on the intensity of the pump beam and the conversion efficiency of the nonlinear optic crystal. Typical OPO outputs have a linewidth from 1 cm^{-1} to 100 cm^{-1} , primarily depending on the phase matching acceptance of the nonlinear optic crystal. The need for only a single input beam allows this technique to be utilized with significantly smaller systems than DFG. However, the overall system size is still considerably larger than that of solid state lasers.

Lead salt lasers generate MIR emission via a p-n junction formed by materials such as PbTe, PbSe, PbS, SnSe, SnTe, and CdS¹³. Electrons are injected into the p-n junction populating the conduction band and creating stimulated emission across the bandgap.

The emission energy is dependent on the bandgap energy of the material, which requires a different material system to create new emission wavelengths. Using compositional variations of the material systems listed above, emissions of 3 – 30 μm can be achieved in a compact laser format (laser diode). Typical power outputs reaching several tens of mW are produced. Lead salt lasers are capable of tuning over a few wavenumbers by temperature and have linewidths from 1 to 1000 MHz¹³.

In general, laser diodes are classified into three main types based on the band alignment at the interface of the barrier and well.¹⁵ Type I lasers have nested bands in which the electrons and holes are confined in the same material. In type II lasers, the bands are staggered with carriers separated into two adjacent layers. Type III lasers use a broken gap with the conduction band of the well and the valence band of the barrier aligned such that – similar to type I - the carriers are separated into adjacent layers. The latter lasers are typically fabricated from III-V materials and cover the spectral range of 2 – 5 μm producing peak powers up to the single Watt range. MIR laser diodes typically produce linewidths of 50 MHz¹³.

Lasers emitting in the MIR widely vary in their power output, tunability, and spectral coverage. Figure 1-3 summarizes the spectral coverage of each MIR laser source discussed above.

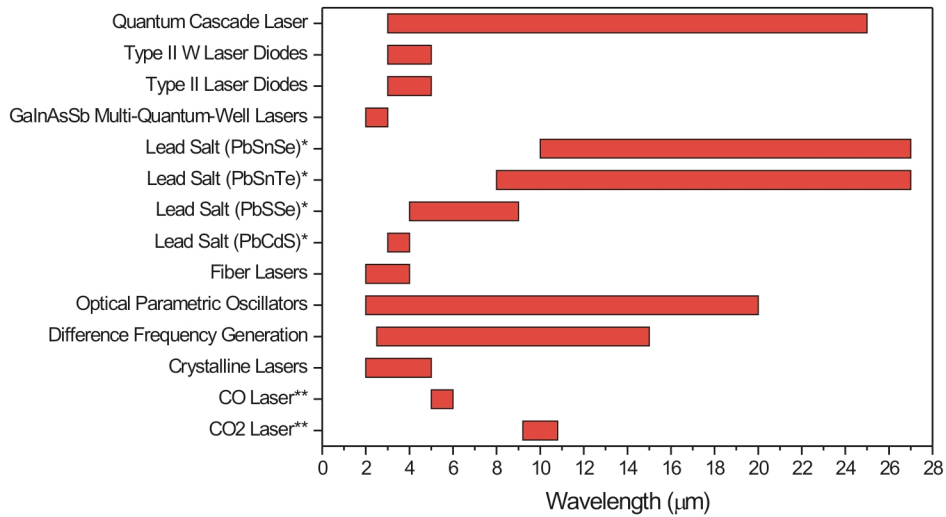


Figure1-3: Spectral coverage of mid-infrared lasers.¹⁶

As shown in Figure 1-3, quantum cascade lasers are the only MIR laser source able to cover the entire spectrum with a single material system.

1.2.4 Quantum Cascade Lasers

The structure of a quantum cascade laser (QCL) was originally proposed in 1971 by Kazarinov and Suris¹⁷. 23 years later, the structure was experimentally realized by Faist et. al.¹⁸ at the Bell Laboratories in 1994. The operation principles, development, and current commercial availability of QCLs will be discussed in detail in Chapter 2 of this thesis.

REFERENCES

1. Janata, J.; Bezegh, A., Chemical Sensors. *Analytical Chemistry* **1988**, 60, (12), 62R-74R.
2. Janata, J., Chemical Sensors. *Analytical Chemistry* **1990**, 62, (12), 33R-44R.
3. Janata, J.; Josowicz, M.; DeVaney, D. M., Chemical Sensors. *Analytical Chemistry* **1994**, 66, (12), 207R-28R.
4. Janata, J.; Josowicz, M.; Vanysek, P.; DeVaney, D. M., Chemical Sensors. *Analytical Chemistry* **1998**, 70, (12), 179R-208R.
5. Hitran Database. In 2004.
6. Mizaikoff, B., Mid-Ir Fiber-Optic Sensors *Analytical Chemistry* **2003**, 75, (11), 258A-267A.
7. Schawlow, A. L.; Townes, C. H., Infrared and Optical Masers. *Physical Review* **1958**, 112, 1940-9.
8. Patel, C. K. N., Interpretation of CO₂ Optical Maser Experiments. *Physical Review Letters* **1964**, 12, (21), 588-590.
9. Patel, C. K. N., Cw High Power N₂-Co₂ Laser. *Applied Physics Letters* **1965**, 7, (1), 15-17.
10. Repound, P.; Sigrist, M. W., Continuously Tunable High-Pressure Co₂ Laser for Spectroscopic Studies on Trace Gases. *IEEE Journal of Quantum Electronics* **1996**, 32, (9), 1549-1559.
11. Urban, W., Physics and Spectroscopic Applications of Carbon Monoxide Lasers, a Review. *Infrared Physics & Technology* **1995**, 36, (2), 465-473.
12. Fischer, C.; Sigrist, M. W., Mid-Ir Difference Frequency Generation. In *Solid-State Mid-Infrared Laser Sources*, Sorokina, I. T.; Vodopyanov, K. L., Eds. Springer-Verlag: Berlin, 2003; Vol. 89.
13. Tittel, F. K.; Richter, D.; Fried, A., Mid-Infrared Laser Applications in Spectroscopy. In *Solid-State Mid-Infrared Laser Sources*, Sorokina, I. T.; Vodopyanov, K. L., Eds. Springer Verlag: Berlin, 2003; Vol. 89.
14. Vodopyanov, K. L., Pulsed Mid-Ir Optical Parametric Oscillators. In *Solid-State Mid-Infrared Laser Sources*, Sorokina, I. T.; Vodopyanov, K. L., Eds. Springer-Verlag: Berlin, 2003; Vol. 89.

15. Joulle, A.; Christol, P.; Baranov, A.; Vicet, A., Mid-Infrared 2-5 Micron Heterojunction Laser Diodes. In *Solid-State Mid-Infrared Laser Sources*, Sorokina, I. T.; Vodopyanov, K. L., Eds. Springer-Verlag: Berlin, 2003; Vol. 89.
16. Sorokina, I. T.; Vodopyanov, K. L., *Solid-State Mid-Infrared Laser Sources*. Springer-Verlag: Berlin, 2003; Vol. 89.
17. Kazarinov, R. F.; Suris, R. A., Possible Amplification of Electromagnetic Waves in a Semiconductor with a Superlattice. *Fizika i Tekhnika Poluprovodnikov (Sankt-Peterburg)* **1971**, 5, (4), 797-800.
18. Faist, J.; Capasso, F.; Sivco, D. L.; Sirtori, C.; Hutchinson, A. L.; Cho, A. Y., Quantum Cascade Laser. *Science (Washington, D. C.)* **1994**, 264, (553-556).

CHAPTER 2

QUANTUM CASCADE LASERS

Currently, the most promising laser light sources in the mid-infrared regime are quantum cascade lasers (QCLs), as they provide a compact, high power radiation source, which is capable of operating across the MIR spectral range.

2.1 Operation Principle

In contrast to conventional laser technology, these QCLs make use of intersubband transitions rather than electron-hole recombination for generating photon emission.

2.1.1 Quantum Heterostructure

In conventional semiconductor lasers, emission is generated by electron-hole recombination between the valence and conduction band, making the emission wavelength dependent on the bandgap of the material. In a QCL, a quantum heterostructure is designed to create quantized states within the conduction band. Electronic transition between these states causes photon emission with a wavelength determined by the energies of the states rather than the bandgap energy of the material.

Bandstructure engineering used in the design of the heterostructure dictates the thickness of the required material layers to produce a given emission wavelength. The layer thicknesses can be controlled with atomic precision by epitaxial growth using molecular beam epitaxy (MBE) techniques. Figure 2-1 shows a scheme of a quantum heterostructure under bias with its electronic transitions.

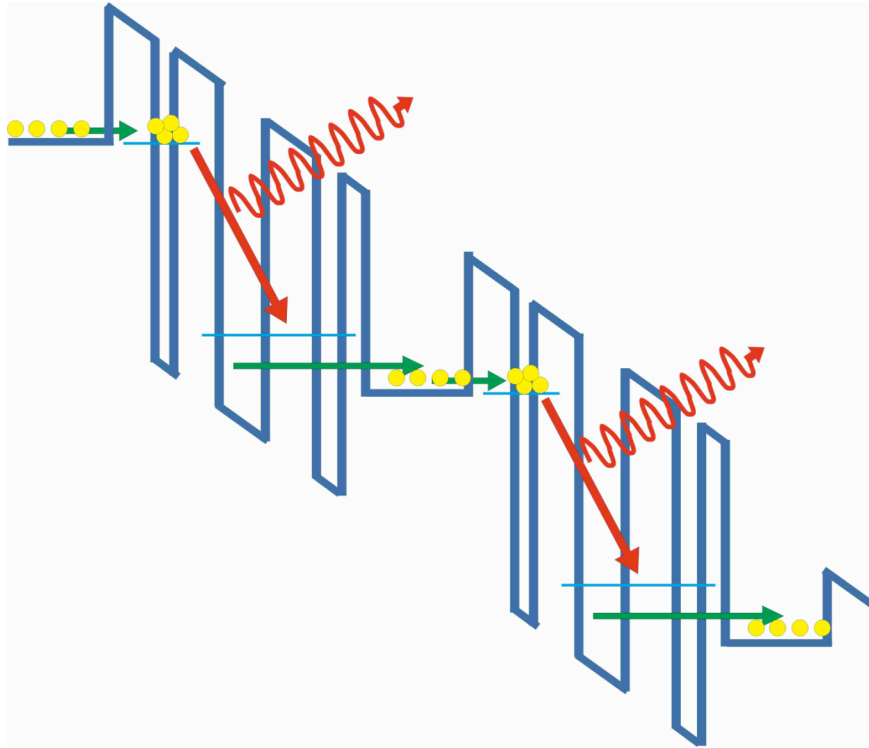


Figure 2-1: Operation principle of QCLs.

Electrons enter the heterostructure through an injector region at the left of the heterostructure in Figure 2-1 and relax into the lower energy state (shown by red arrow) releasing a photon. Population inversion is achieved, if the electron is rapidly removed from the well by a longitudinal-optic (LO) phonon transition (indicated by the green arrow), and enters into a second injector region. This process is repeated for each period of the QCL providing a cascade effect and allowing a single electron to produce multiple photons for increasing the output power of the laser. A single laser typically has on the order of 40 periods.

2.1.2 QCL Composition

The most common material system for QCLs is InGaAs/AlInAs on an InP substrate; all lasers used in this thesis are of this composition. QCLs have also been demonstrated using the GaAs/AlGaAs¹ materials system, however, the focus of this discussion will be on InGaAs/AlInAs materials. Figure 2-2 schematically shows the composition of the lasers used in this thesis.

A typical laser structure consists of an InP wafer substrate with a bottom waveguide layer of InGaAs grown on top of the wafer. The waveguide is followed by the gain medium consisting of alternating layers of InGaAs and AlInAs, whose thickness determines the properties of the quantum heterostructure. A top waveguide layer covers the gain medium followed by a silicon nitride insulation layer and a grating (in the case of DFB lasers, see discussion below) and a lateral contact. The top layer is a contact material, usually titanium and gold.

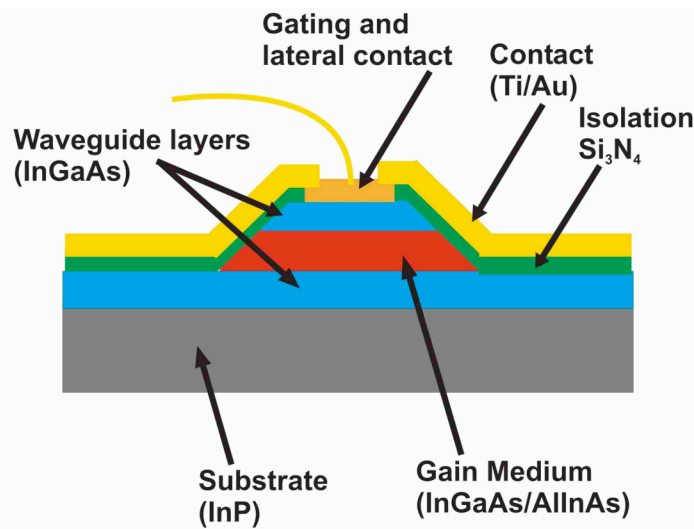


Figure 2-2: QCL composition.

In the structure shown in Figure 2-2, electrons would be injected through the wire bonds shown on the lateral contact layer and would then tunnel through the gain medium. Photon generation would occur in the gain medium layer and emission would be out of the plane of the schematic, toward the reader.

2.1.3 Fabry-Perot and Distributed Feedback Lasers

QCLs are fabricated as two main types: (i) Fabry-Perot, and (ii) distributed feedback (DFB) devices, with the difference being a grating layer incorporated either buried² in the top waveguide layer or at the layer surface³ for DFB lasers. This grating forces DFB lasers to emit a single light mode providing a much more narrow linewidth than Fabry-Perot lasers. Hence, the selection of overlapping analyte bands associated with gaseous or liquid phase analytes is facilitated for the development of absorption based optical IR sensor with inherent molecular selectivity.

2.2 History

The concept of the QCL was described in 1971 by Kazarinov and Suris⁴, and was first experimentally realized by Faist et. al.⁵ at the Bell Laboratories more than twenty years later. As with the development of any laser, the first QCL demonstration occurred in pulsed mode and at low operating temperatures (10 K). Subsequent research then aimed at achieving continuous wave (cw) operation and raising the operating temperature. Since then, QCL development has also included increasing the power output and the wavelength coverage range.

2.2.1 Operation Temperature

Due to the inverse dependence of the quantum efficiency on the device operating temperature, there is a compromise between operating temperature and laser output power. The achievement of high power operation at two different temperatures becomes key to convenient laser use: operation at a temperature of 77 K allows use at liquid nitrogen conditions, while room temperature (or near room temperature) operation allows using thermoelectric temperature stabilization. Liquid nitrogen operation avoids the use of costly and inconvenient liquid helium (achieving 10 K operating temperatures), while thermoelectric cooling avoids the need for consumables completely. The first QCL demonstrated a power output of nearly 10 mW at a temperature of 10 K⁵. Room temperature operation was then achieved through the incorporation of a funnel-shaped injector region with output powers of 15 mW at 274 K and 1.5 mW at 300 K⁶. These lasers were both operated in pulsed mode allowing the laser to dissipate heat between the pulses.

2.2.2 Continuous Wave Operation

Continuous wave (cw) operation is desirable for sensing applications as it eliminates pulse-to-pulse amplitude variations, achieves higher average powers, and allows for the implementation of more sophisticated noise reduction techniques. Operation in cw mode was first demonstrated at 80 K in 1995⁷ with a laser producing an output power of 2 mW in continuous mode. Room temperature cw QCL operation was achieved in 2002⁸ by introducing a buried heterostructure providing improved heat dissipation. This laser was able to produce powers of up to 17 mW in continuous wave mode at a temperature of 292 K.

In order to achieve cw operation with both high (room) temperature and high power output, efficient heat dissipation must be achieved. The nature of the structure in the gain medium of a QCL presents a challenge in this area. The interfaces of many material layers and the ternary alloys used to create the quantum heterostructure cause the gain medium to typically have a much higher temperature than the substrate⁹. As the thermal resistance of air is considerably high, QCL structures are frequently buried⁸ or mounted top side down (or epilayer down) on a heat sink in order to allow more efficient dissipation of heat from the gain medium to the substrate, which enabled cw operation at room temperature resulting from more efficient heat dissipation.

2.2.3 Distributed Feedback QCLs

DFB QCLs were first demonstrated in 1997³ by incorporating a grating on the top of the laser ridge using wet chemical etching techniques. This structure gave a linewidth of less than 0.3 cm^{-1} for pulses of 10 ns operated at 300 K, while producing an output power of 60 mW. This laser showed a tuning range of 60 nm by changing the operating temperature between 100 and 320 K. The first continuous wave operation of a DFB QCL¹⁰ was demonstrated with a laser providing an output power of 10 mW at 120 K and a tuning range of 140 nm from 20 to 120 K.

The initial demonstrations of DFB structures discussed above utilized gratings fabricated on the top of the waveguide layer, which is disadvantageous as it places the grating in the evanescent tail of the waveguide mode, although closer contact would be desirable¹¹. Therefore, gratings buried in the waveguide core were subsequently demonstrated.¹²

Currently, most QCLs are fabricated as DFB type, as the narrow linewidth is ideal, in particular for gas sensing applications.

2.2.4 High Power Output

Due to the requirement of dissipating heat from the laser structure, there is a compromise between duty cycle, operating temperature, and power output to be achieved. The fabrication of high power QCLs has primarily been investigated by the Razeghi group at Northwestern University. Recent notable achievements of this group in high power emission from QCLs are lasers emitting an average power of 600 mW from pulsed lasers

at 293 K with 50 % duty cycle¹³, and an average power output of 424 mW in continuous wave mode at 293 K¹⁴.

2.2.5 Wavelength Range

QCLs composed of InGaAs/AlInAs lattice matched to an InP substrate cover the spectral range from 4 to 25 μm ¹⁵. Wavelengths from 8 to 15 μm require the addition of an insulation layer between the top waveguide cladding layer and the metal contact to reduce losses into the metal layer¹⁶. Wavelengths above 15 μm usually apply top waveguides based on surface plasmons by confining the light to the interface between a metal and the semiconductor^{17, 18}. This avoids the use of very thick waveguide layers needed for conventional dielectric waveguides used at shorter wavelengths, which allows lower laser thresholds to be reached at acceptable operating conditions.

The use of a double surface plasmon waveguide¹⁹ in which both the top and bottom cladding layers confine light at a metal-semiconductor interface has allowed the emission range of QCLs to be extended into the THz regime. Lasers have been demonstrated at 69 μm (4.4 THz)²⁰ and 66 μm (4.5 THz)²¹ with output powers of a few mW at temperatures of 44 K and 12 K, respectively. Lasers using a bound-to-continuum structure (discussed below) achieved emission at 87 μm with powers of up to 10 mW at 77 K²². Continuous wave operation has been achieved in a laser emitting at 94 μm at 78 K producing 400 μW of output power²³.

In QCL technology, wavelengths below 4 μm are considered relatively short. Wavelengths between 3 and 4 μm are of great interest to sensing applications due to the presence of an atmospheric window between 3 and 5 μm , as discussed in Chapter 1. In this range, QCLs must be developed using strain compensated layers. This provides a sufficiently large conduction band discontinuity to achieve higher energy photon emission. Lasers of InGaAs/InAlAs composition have been demonstrated at 3.4 μm with peak powers of 120 mW at 15 K, and approximately 5 mW of output power at 280 K²⁴. QCLs with a composition of InGaAs/AlAs have demonstrated operation at 3.8 μm with an operating temperature of 296 K, emitting peak powers of up to 240 mW²⁵.

2.2.6 Novel QCL Structures

Most QCLs emit from the end facet, as described in section 2.1.2. However, partial emission has also been demonstrated, which occurs vertically from the top surface of the laser²⁶. Further improvements by developing a window region at the laser surface enabled emission from the top surface to exceed that from the laser end facet, providing a first step toward the vertical integration of IR laser light sources²⁷.

Multicolor QCLs have been fabricated using two separate gain medium areas emitting at 8.0 and 5.2 μm ²⁸, as well as using a single gain medium with two types of active regions producing slightly different emission wavelengths at 9.5 and 8.0 μm ²⁹. A QCL has also been demonstrated, which emits at a wavelength of 6.3 or 6.5 μm depending on the direction of the bias voltage³⁰.

Bound-to-continuum QCLs³¹ allow a broad gain spectrum to be achieved with a single laser. These lasers utilize a single initial state with transitions to several final states, which allows for a larger range of emission energies.

QCLs coupled to external cavities provide a significantly increased tuning range for the laser rendering them of substantial interest for sensing applications. A recent demonstration by the Faist group utilized a bound-to-continuum laser grating-coupled to an external cavity resulting in a tuning range of over 150 cm^{-1} ($1.45 \text{ }\mu\text{m}$)³².

2.3 Availability of QCLs

The advantage of QCLs over other MIR laser sources is their potential for complete spectral coverage within a single materials system. In theory, creating a new emission wavelength is as simple as changing the thickness of the layers in the gain medium as determined by bandstructure engineering. However, in practice it is difficult to achieve a target wavelength with precision and repeatability due to the limited control of the layer growth. Creation of new emission wavelengths also requires re-optimization of the waveguides and gratings (in the case of DFB lasers) the practical implementation is again more complex than theory predicts.

2.3.1 Commercial Availability

Alpes Laser is the only company currently producing QCLs for commercial sale. Lasers are available with both Fabry-Perot (multimode) and DFB (single mode) output. Most lasers produced are operated in pulsed mode at room temperature. Continuous wave lasers are available for operation at 80 K.

Currently, in-stock room temperature pulsed DFB lasers partially cover the emission range of 865 cm^{-1} to 2351 cm^{-1} . As of October 2005, the list of in-stock lasers comprises over 150 lasers, each with a tuning range of a few wavenumbers throughout this range.

Available cryogenic continuous wave DFB lasers partially cover the spectral range from 1033 cm^{-1} to 2375 cm^{-1} . Currently, approximately 20 lasers are available covering a few wavenumbers each.

Upon request, custom-built pulsed lasers in the range of 4 to 16 μm (625 cm^{-1} to 2500 cm^{-1}) or continuous wave lasers in the range of 5 to 5 μm (1100 cm^{-1} to 2000 cm^{-1}) are available. However, custom-built lasers are currently produced at prohibitively higher cost and require a substantial lead time (> 6 months) as they require the entire growth process to be designed and optimized for the requested laser heterostructure and the DFB grating.

2.4 QCL Characterization

The following section describes the characteristics of the QCLs used in this thesis, which were DFB lasers purchased from Alpes Laser and operated in pulsed mode at or near room temperature and stabilized with Peltier cooling.

2.4.1 Response curve

A typical laser power output curve as a function of driving pulse amplitude is shown in Figure 2-3.

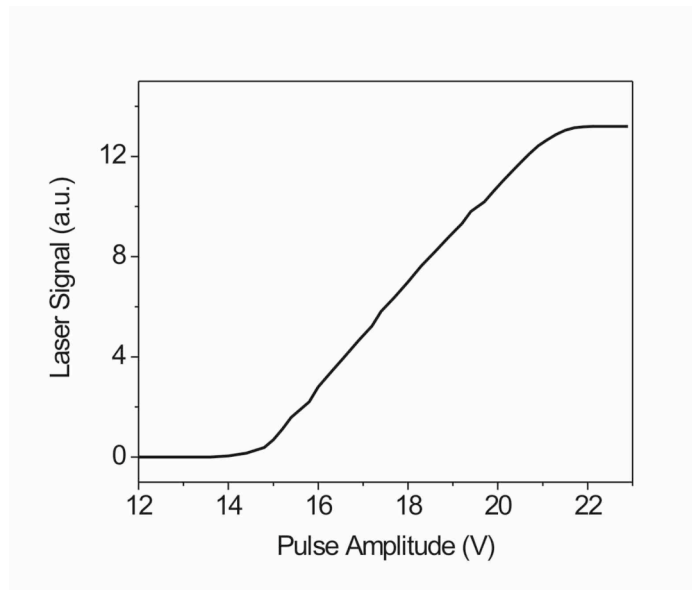


Figure 2-3: Response curve of laser s1537 emitting at 974 cm^{-1} ($10.3\text{ }\mu\text{m}$).

Figure 2-3 shows the lasing threshold to be at 15 V. From this threshold, the laser output power linearly increases through 21 V of applied amplitude, after which the output levels off. If increased past this plateau, the laser would be damaged due to excess heating of the heterostructure.

2.4.2 Temperature Tuning

Wavelength tuning in DFB lasers as a function of temperature is achieved due to the grating incorporated in the laser structure, which selects the emission wavelength. As the temperature of the structure increases, the grating expands and the spacing of the grating features increases, thereby shifting the emission wavelength selected by the grating towards longer wavelengths.

The output wavelength as a function of laser operating temperature for laser (serial number s1869) with peak emission at 1848 cm^{-1} ($5.4 \mu\text{m}$) is shown in Figure 2-4.

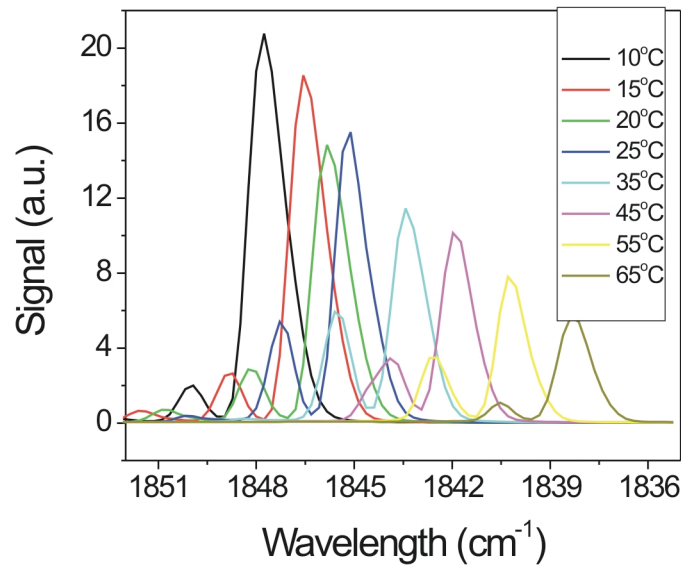


Figure 2-4: Temperature tuning for laser s1869.

As shown in Figure 2-4, laser s1869 is tunable over 10 cm^{-1} (from 1848 cm^{-1} to 1838 cm^{-1}) by changing the temperature of the laser heat sink from $10 \text{ }^\circ\text{C}$ to $65 \text{ }^\circ\text{C}$. Temperature

control is achieved by Peltier cooling elements as discussed in section 2.5.1 below. Figure 2-4 also reveals that the laser emission at each temperature includes a small side mode next to the main emission frequency, which is common to DFB lasers. However, the output is nearly single mode.

Laser s1537 was also characterized for temperature tuning of the output wavelength, showing very different results to the behavior of laser s1869. Figure 2-5 shows the tuning characteristics for laser s1537.

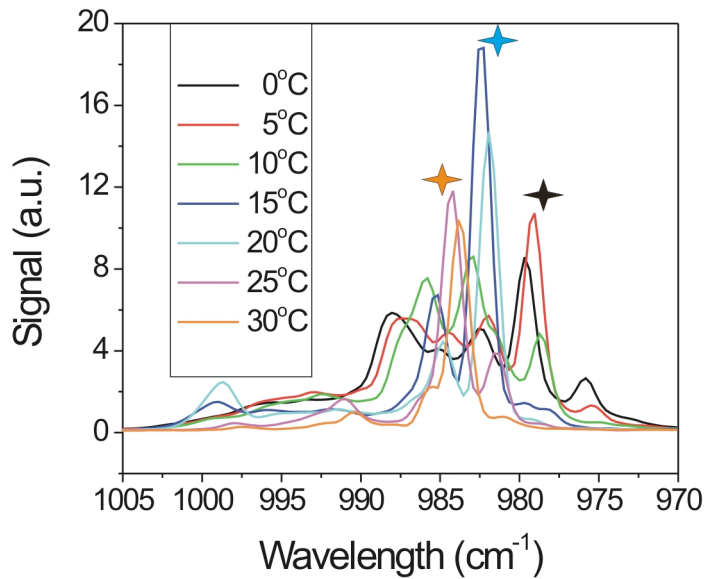


Figure 2-5: Temperature tuning for laser s1537.

As shown in Figure 2-5, output from this laser has a significant multimode component. At each operating temperature, one mode is emitted at significantly higher intensity than others. However, the mode of highest emission changes with temperature. Three different strong emission modes are indicated by stars in Figure 2-5. At temperatures of

0 and 5 °C, the strongest emission is observed at approximately 979 cm^{-1} . The strongest emission is achieved at approximately 982 cm^{-1} for 15 and 20 °C, and at 984 cm^{-1} for 25 and 30 °C. Within each of these mode hops, tuning appears to occur normally with higher temperatures shifting the output emission towards longer wavelengths.

2.4.3 Pulse Shape Behavior

The shape of the pulse driving the QCL is shown in Figure 2-6.

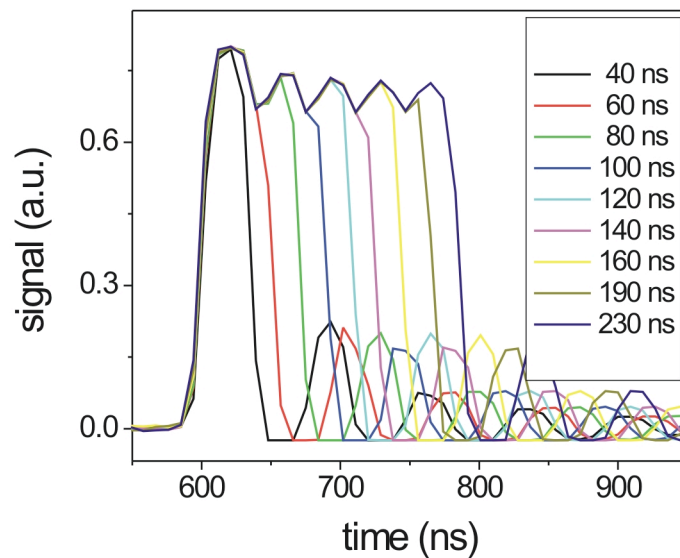


Figure 2-6: Driving pulse shape.

The pulses shown in Figure 2-6 are the electrical pulses used to drive the QCL as directly measured from the pulse generator. It is evident from these pulses that the amplitude is slightly higher at the beginning of the pulse and decreases within the longer pulses after

the initial spike. Therefore, we expect to see the same shape in the optical pulse, if a QCL is driven with these electrical pulses.

However, due to the 20 MHz bandwidth of the detector (discussed below in section 2.5.2), this shape is not resolved on pulses with a short duration (100 ns or less). Instead, the pulse takes the shape of a Gaussian, as shown in Figure 2-7.

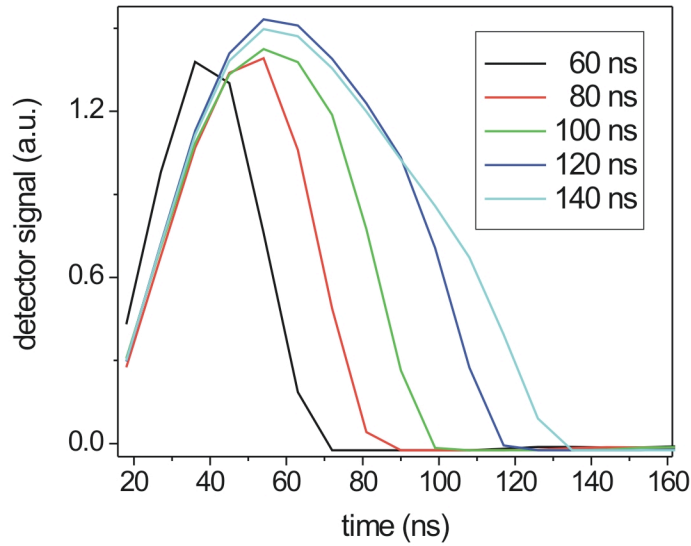


Figure 2-7: QCL output with increasing pulse width.

Figure 2-7 shows that for longer pulses (> 100 ns), the pulse begins to reflect the shape of the larger amplitude at the pulse onset, which decreases in amplitude after the initial spike. Both lasers s1537 and s1869 were characterized and revealed the same pulse shape characteristics indicating that this shape results from the driving electronics.

2.4.4 Beam Output Characteristics

Lasers emit an elliptical beam that is divergent with 40° in the horizontal direction and 60° in the vertical direction.

Beam divergence was confirmed by measuring the laser signal using a room-temperature mercury-cadmium-telluride (MCT) detector without window in front of the detector element. Hence, the detector element could be placed directly in the radiation cone emitted from the QCL to determine the beam shape. The disadvantage of the used room-temperature MCT detector is the decreased sensitivity in contrast to cooled devices (with IR transparent window) due to thermal noise. The room temperature MCT detector has a maximum detectivity 3 orders of magnitude smaller than that of liquid nitrogen-cooled MCT devices used during the sensing applications, which are discussed in section 2.5.2.

The radiation output cone was measured to be divergent at 40° in the horizontal direction and 60° in the vertical plane with a Gaussian intensity profile in both directions.

2.5 System Electronics

This section describes the electronics used for all measurements in this thesis, including laser driving and signal recovery instrumentation.

2.5.1 Alpes Lasers Components

Laser driving electronics purchased from Alpes Laser are shown in a block diagram in Figure 2-8.

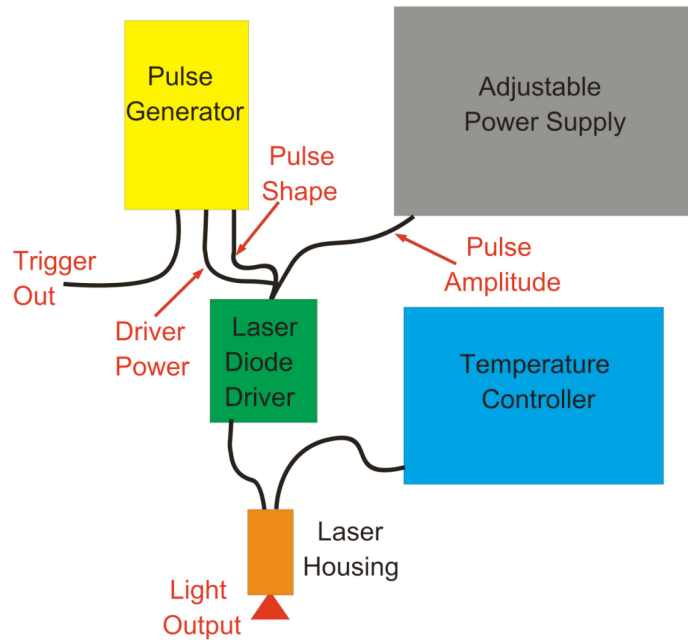


Figure 2-8: Block diagram of Alpes Laser QCL driving electronics.

The system consists of a pulse generator (TPG128, Alpes Laser, Neuchâtel, Switzerland) providing the pulse shape, as well as a trigger signal to synchronize the detection electronics, and a ± 12 V signal to power the laser diode driver. A 2-channel external

adjustable power supply (Shenzhen Mastech, HY3002D-2, Shanghai, China) with an output of 0 – 30 V per channel controls the pulse amplitude. A laser diode driver (LDD100, Aples Laser, Neuchâtel, Switzerland) is used to combine the pulse shape and amplitude and sends the full pulse to the laser housing via a low impedance line. The temperature controller (TC51, Alpes Laser, Neuchâtel, Switzerland) reads and adjusts the laser heat sink temperature via Peltier coolers inside the laser housing.

The laser housing transmits the electrical driving pulse to the laser and controls its operating temperature, as shown in Figure 2-9.

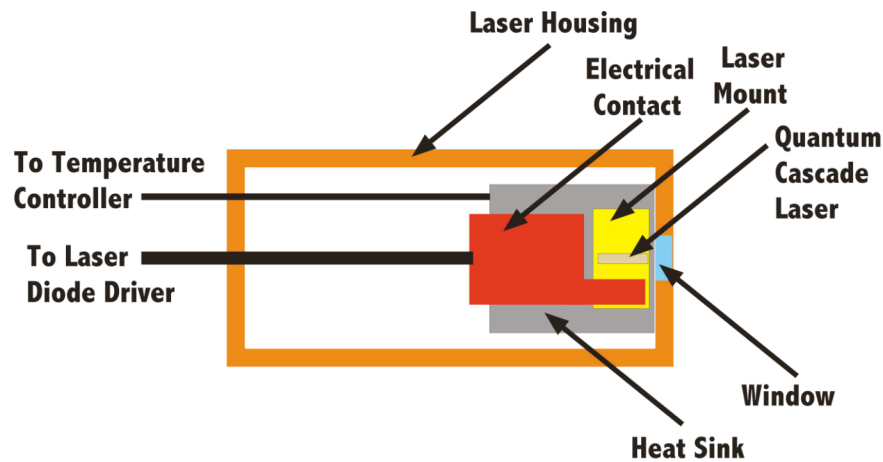


Figure 2-9: Laser housing electronics.

The laser is mounted in the housing as shown in Figure 2-9. Beneath the laser mount is a heat sink, which is connected to Peltier cooling elements and the external temperature controller. The electrical pulse signal is sent to the housing electronics by the laser diode driver and reaches the laser via wire bonds (not shown in schematic) connected to the electrical top contact of the laser diode. Light emission occurs from the cleaved and

polished laser end facet and exits the housing via a MIR transparent window (AR-coated ZnSe) at the front.

The pulse generator used to drive the lasers in this setup produces amplitude fluctuations in the pulse signal. As sensing systems in this work detect the presence of a chemical based on a decrease in laser pulse amplitude caused by absorption, pulse-to-pulse amplitude fluctuations are detrimental to the system sensitivity. A variety of data acquisition systems discussed below were used to overcome this problem decreasing the system noise and improving the sensitivity.

Temperature control is achieved by Peltier cooling elements in the laser housing connected to an external temperature control unit. The manufacturer-specified range for the system is -40 °C to +80 °C. Additional water cooling is needed to achieve the lower end of the temperature range (< 0 °C).

2.5.2 Detectors

Detectors used for all studies in this work were liquid nitrogen-cooled mercury-cadmium-telluride (MCT) detectors purchased from Kolmar Technologies (Newburyport, MA). Two identical detectors (model number KMPV11-1-LJ2) were purchased allowing 2-channel setups with similar detectors. These detectors include an integrated signal preamplifier. Table 2-1 below shows the specifications for these detectors.

Table 2-1: Detector Specifications

Detector Parameter	Value
Detector Element Area	1 mm ²
Responsivity	4.75 Amps/Watt
Peak Wavelength	9.7 μm
Cutoff Wavelength	12.0 μm
Signal Rise Time	19 ns
Bandwidth	20 MHz
Detectivity (at 20 MHz)	2.13 e ¹⁰ Jones

The bandwidth of this detector and preamplifier is higher than conventional liquid nitrogen cooled MCT detectors which are typically available in the range of 1 Hz to 1 MHz³³. However, the true peak shape of the laser output is still not fully resolved, as discussed in section 2.4.4.

2.5.3 Data Acquisition

Early studies in this work utilize a digital oscilloscope (TDS3032, Tektronix, Beaverton, OR) for data acquisition. This oscilloscope has a bandwidth of 300 MHz and was used for detector signal readout of individual laser pulses by triggering from the pulse generator. Pulse-to-pulse fluctuations were improved by averaging 512 curves, which is the maximum averaging capability available on the oscilloscope.

Further reduction of noise due to pulse-to-pulse fluctuations was achieved using the Saturn data acquisition system purchased from AMO (Aachen, Germany). This system provides externally triggered simultaneous recording of two channels at 100 MHz on each channel. This system is also capable of providing averaging of 10⁶ curves in approximately 8 s, and was used in some of the later studies of this thesis.

REFERENCES

1. Sirtori, C.; Page, H.; Becker, C.; Ortiz, V., Gaas-Algaas Quantum Cascade Lasers: Physics, Technology, and Prospects. *IEEE Journal of Quantum Electronics* **2002**, 38, (6), 547-558.
2. Gmachl, C.; Faist, J.; Baillargeon, J. N.; Capasso, F.; Sirtori, C.; Chu, S. N. G.; Cho, A. Y., *IEEE Photonics Technological Letters* **1997**, 9, 1090-1092.
3. Faist, J.; Gmachl, C.; Capasso, F.; Sirtori, C.; Sivco, D. L.; Baillargeon, J. N.; Cho, A. Y., Distributed Feedback Quantum Cascade Lasers. *Applied Physics Letters* **1997**, 70, (20), 2670-2.
4. Kazarinov, R. F.; Suris, R. A., Possible Amplification of Electromagnetic Waves in a Semiconductor with a Superlattice. *Fizika i Tekhnika Poluprovodnikov (Sankt-Peterburg)* **1971**, 5, (4), 797-800.
5. Faist, J.; Capasso, F.; Sivco, D. L.; Sirtori, C.; Hutchinson, A. L.; Cho, A. Y., Quantum Cascade Laser. *Science (Washington, D. C.)* **1994**, 264, (553-556).
6. Faist, J.; Capasso, F.; Sirtori, C.; Sivco, D. L.; Hutchinson, A. L.; Cho, A. Y., Room Temperature Mid-Infrared Quantum Cascade Lasers. *Electronics Letters* **1996**, 32, (6), 560-661.
7. Faist, J.; Capasso, F.; Sirtori, C.; Sivco, D. L.; Hutchinson, A. L.; Cho, A. Y., Continuous Wave Operation of a Vertical Transition Quantum Cascade Laser above T=80k. *Applied Physics Letters* **1995**, 67, (21), 3057-3059.
8. Beck, M.; Hofstetter, D.; Aellen, T.; Faist, J.; Oesterel, U.; Ilegems, M.; Gini, E.; Melchior, H., Continuous Wave Operation of a Mid-Infrared Semiconductor Laser at Room Temperature. *Science (Washington, D. C.)* **2002**, 295, 301-304.
9. Spagnolo, V.; Scamarcio, G.; Marano, D.; Troccoli, M.; Capasso, F.; Gmachl, C.; Sergent, A. M.; Hutchinson, A. L.; Sivco, D. L.; Cho, A. Y.; Page, H.; Becker, C.; Sirtori, C., Thermal Characteristics of Quantum-Cascade Lasers by Micro-Probe Optical Spectroscopy. *IEE Proceedings: Optoelectronics* **2003**, 150, (4), 298-305.
10. Gmachl, C.; Capasso, F.; Faist, J.; Hutchinson, A. L.; Tredicucci, A.; Sivco, D. L.; Baillargeon, J. N.; Chu, S. N. G.; Cho, A. Y., Continuous-Wave and High-Power Pulsed Operation of Index-Coupled Distributed Feedback Quantum Cascade Laser at ≈ 8.5 Mm. *Applied Physics Letters* **1998**, 72, (12), 1430-1432.
11. Gmachl, C.; Straub, A.; Colombelli, R.; Capasso, F.; Sivco, D. L.; Sergent, A. M.; Cho, A. Y., Single-Mode, Tunable Distributed-Feedback and Multiple-

- Wavelength Quantum Cascade Lasers. *IEEE Journal of Quantum Electronics* **2002**, 38, (6), 569-581.
12. Gmachl, C.; Faist, J.; Baillargeon, J. N.; Capasso, F.; Sirtori, C.; Sivco, D. L.; Chu, S. N. G.; Cho, A. Y., Complex-Coupled Quantum Cascade Distributed Feedback Laser. *IEEE Photonics Technological Letters* **1997**, 9, 1090-1092.
 13. Evans, A.; Yu, J. S.; Slivken, S.; Razeghi, M., Continuous-Wave Operation of Wavelength Approx. 4.8 Mm Quantum Cascade Lasers at Room Temperature. *Applied Physics Letters* **2004**, 85, (12), 2166-2168.
 14. Yu, J. S.; Evans, A.; David, J.; Slivken, S.; Razeghi, M., High-Power Continuous-Wave Operation of Quantum Cascade Lasers up to 60 Degrees C. *IEEE Photonics Technological Letters* **2004**, 16, (3), 747-749.
 15. Capasso, F.; Gmachl, C.; Sivco, D. L.; Cho, A. Y., Quantum Cascade Lasers. *Physics Today* **2002**, 55, (5), 34-45.
 16. Sirtori, C.; Faist, J.; Capasso, F.; Sivco, D. L.; Hutchinson, A. L.; Cho, A. Y., Quantum Cascade Lasers with Plasmon-Enhanced Waveguide Operating at 8.4 Mm Wavelength. *Applied Physics Letters* **1995**, 66, 3242-3244.
 17. Capasso, F.; Paiella, R.; Martini, R.; Colombelli, R.; Gmachl, C.; Myers, T. L.; Taubman, M. S.; Williams, R. M.; Bethea, C. G.; Unterrainer, K.; Hwang, H. Y.; Sivco, D. L.; Cho, A. Y.; Sergent, M.; Liu, H. C.; Whittaker, E. A., Quantum Cascade Lasers: Ultrahigh-Speed Operation, Optical Wireless Communication, Narrow Linewidth, and Far-Infrared Emission. *IEEE Journal of Quantum Electronics* **2002**, 38, (6), 511-532.
 18. Sirtori, C.; Gmachl, C.; Capasso, F.; Faist, J.; Sivco, D. L.; Hutchinson, A. L.; Cho, A. Y., Long Wavelength ($\approx 8 - 11.5$ Mm) Semiconductor Lasers with Waveguides Based on Surface Plasmons. *Optics Letters* **1998**, 24, (1366-1368).
 19. Unterrainer, K.; Colombelli, R.; Gmachl, C.; Capasso, F.; Hwang, H. Y.; Sivco, D. L.; Cho, A. Y., Quantum Cascade Lasers with Double Metal Semiconductor Waveguide Resonators. *Applied Physics Letters* **2001**, 80, 3060-3062.
 20. Koehler, R.; Tredicucci, A.; Beltram, F.; Beere, H. E.; Linfield, E. H.; Davies, A. G.; Ritchie, D. A.; Iotti, R. C.; Rossi, F., Terahertz Semiconductor-Heterostructure Laser. *Nature (London, United Kingdom)* **2002**, 417, 156-159.
 21. Rochat, M.; Ajili, L.; Willenberg, H.; Faist, J.; Beere, H. E.; Davies, G.; Linfield, E. H.; Ritchie, D. A., Low-Threshold Terahertz Quantum-Cascade Lasers. *Applied Physics Letters* **2002**, 81, (6), 1381-1383.

22. Scalari, G.; Ajili, L.; Faist, J.; Beere, H.; Linfield, E.; Ritchie, D.; Davies, G., Far-Infrared (≈ 87 Mm) Bound-to-Continuum Quantum-Cascade Lasers Operating up to 90 K. *Applied Physics Letters* **2003**, 82, (19), 3165-3167.
23. Kumar, S.; Williams, B. S.; Kohen, S.; Hu, Q.; Reno, J. L., Continuous-Wave Operation of Terahertz Quantum-Cascade Lasers above Liquid-Nitrogen Temperature. *Applied Physics Letters* **2004**, 84, (11), 2494-2496.
24. Faist, J.; Capasso, F.; Sivco, D. L.; Hutchinson, A. L.; Chu, S. N. G.; Cho, A. Y., Short Wavelength (≈ 3.4 Mm) Quantum Cascade Laser Based on Strained Compensated InGaAs/AlInAs. *Applied Physics Letters* **1998**, 72, (6), 680-682.
25. Semtsiv, M. P.; Ziegler, M.; Dressler, S.; Masselink, W. T.; Georgiev, N.; Dekorsy, T.; Helm, M., Above Room Temperature Operation of Short Wavelength (3.8 Mm) Strain-Compensated In_{0.73}Ga_{0.27}As-AlAs Quantum-Cascade Lasers. *Applied Physics Letters* **2004**, 85, (9), 1478-1480.
26. Hofstetter, D.; Faist, J.; Beck, M.; Oesterel, U., Surface-Emitting 10.1 Mm Quantum-Cascade Distributed Feedback Lasers. *Applied Physics Letters* **1999**, 75, (24), 3769-3771.
27. Schrenk, W.; Finger, N.; Gianordoli, S.; Hvozdar, L.; Strasser, G.; Gornik, E., Surface-Emitting Distributed Feedback Quantum-Cascade Lasers. *Applied Physics Letters* **2000**, 77, (14), 2086-2088.
28. Gmachl, C.; Sivco, D. L.; Baillargeon, J. N.; Hutchinson, A. L.; Capasso, F.; Cho, A. Y., Quantum Cascade Lasers with a Heterogeneous Cascade: Two-Wavelength Operation. *Applied Physics Letters* **2001**, 79, (5), 572-574.
29. Straub, A.; Mosely, T. S.; Gmachl, C.; Colombelli, R.; Troccoli, M.; Capasso, F.; Sivco, D. L.; Cho, A. Y., Threshold Reduction in Quantum Cascade Lasers with Partially Undoped Dual-Wavelength Interdigitated Cascades. *Applied Physics Letters* **2002**, 80, (16), 2845-2847.
30. Gmachl, C.; Tredicucci, A.; Sivco, D. L.; Hutchinson, A. L.; Capasso, F.; Cho, A. Y., Bidirectional Semiconductor Laser. *Science (Washington, D. C.)* **1999**, 286, 749-752.
31. Faist, J.; Beck, M.; Aellen, T.; Gini, E., Quantum-Cascade Lasers Based on a Bound-to-Continuum Transition. *Applied Physics Letters* **2001**, 78, (2), 147-149.
32. Maulini, R.; Beck, M.; Faist, J.; Gini, E., Broadband Tuning of External Cavity Bound-to-Continuum Quantum-Cascade Lasers. *Applied Physics Letters* **2004**, 84, (10), 1659-1661.
33. IR Associates, www.irassociates.com

CHAPTER 3

ABSORPTION-BASED OPTICAL SENSORS

The absorption-based optical sensors described in this work can be categorized into two types: (i) transmission absorption measurements, and (ii) evanescent field absorption measurements. The principles governing each type of measurement will be described in this chapter, along with their implications to chemical sensing.

3.1 Fundamentals of Transmission Absorption Spectroscopy

The simplest absorption measurements are performed in a transmission configuration with light passing directly through the sample and being absorbed at frequencies where resonant energy transfer occurs. The measurement setup for transmission absorption spectroscopy is shown in Figure 3-1.

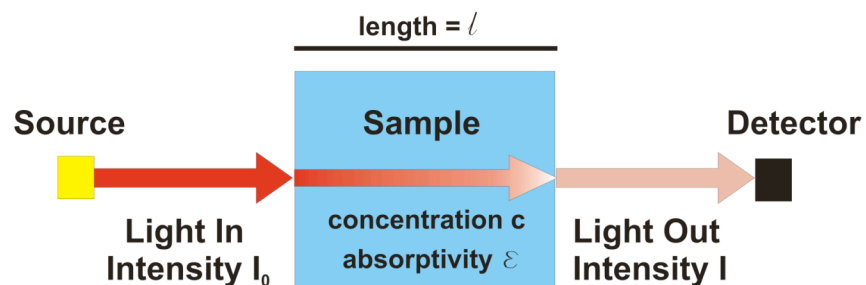


Figure 3-1: Transmission Absorption Measurement Setup.

In Figure 3-1, light from a source with an intensity I_0 passes through a sample of thickness l , concentration c and molar absorptivity ϵ , and is partially absorbed by the sample giving an exiting intensity of I measured by a detector.

3.1.1 Lambert-Beer Law

For the system shown in Figure 3-1, the absorbance (A) of the measurement is governed by the Lambert-Beer law:

$$A = \epsilon c l \quad (\text{Eqn 3.1})$$

where ϵ is the molar absorptivity, c is the concentration, and l is the optical path length of the radiation through the sample.

Absorbance can also be defined by the change in intensity as light passes through the sample:

$$A = -\log (I/I_0) = \epsilon c l \quad (\text{Eqn 3.2})$$

where I_0 is the intensity of light entering the sample and I is the intensity exiting. Equation 3.2 allows concentration data to be directly calculated from a change in absorbance signal.

The Lambert-Beer law shows a linear dependence of the absorbance (A) on the concentration (c). However, this is only valid at low concentrations (approximately $< 0.01\text{M}$). At high concentrations, the relationship becomes non-linear, primarily due to deviations in ϵ arising from electrostatic interactions between molecules in close proximity.

3.1.2 Lambert-Beer Law in Chemical Sensing

The goal of most chemical sensors is to achieve the highest possible sensitivity, i.e. to detect the lowest possible concentration for the species of interest. As absorption measurements are dependent on a limited number of variables related by the Lambert-Beer law, a discrete list of parameters determines the optimization space for sensitivity improvements.

The molar absorptivity (ϵ) describes the absorption strength for a particular molecular species at a given wavelength and is an inherent material property. ϵ primarily becomes a factor in chemical sensing for the initial selection of a wavelength regime for optical sensing (e.g. UV, Vis, NIR, MIR, etc.), and for the selection of a particular operating wavelength within the selected band. The fundamental rotational and vibrational transitions excited by radiation in the mid infrared (2.5 - 20 μm) regime are much stronger than e.g. the overtone vibrations excited in the near infrared (NIR, 0.7 – 2.5 μm). Hence, it is advantageous operating optical sensors in the MIR range despite the more limited availability of light sources, detectors, and waveguide materials compared with the NIR range. In laser-based sensing systems, operating at a single wavelength ensuring

overlap between the laser emission frequency and a strong absorption band of the analyte will lead to high sensitivity. In addition, as rotational and vibrational modes reflect the molecular composition of the illuminated species, inherent molecular selectivity is provided in this frequency regime.

As an increase in optical path length provides a higher degree of interaction between photons and sample, a longer path length will lead to a higher sensitivity in an absorption measurement. This circumstance is frequently utilized in gas sensing using multi-pass transmission gas cells providing an extended optical path length by folding the beam in a compact optical configuration. This leads to significantly decreased limits of detection (low ppb to ppt (v/v) range).

The last parameter to be optimized for the detection of low concentrations in chemical sensing is the absorption measurement. As a low concentration leads to a small change in intensity due to absorption, the ability of a sensing system to discriminate between very small signal changes will determine the ultimate sensitivity. This is typically accomplished by choice of an appropriate optical detector with a high detectivity (D^*) corresponding to a high output signal for a small number of photons incident at the detector element, which can be achieved through amplification of the detector signal.

3.2 Fundamentals of Evanescent Field Absorption Spectroscopy

Evanescent field spectroscopy allows light confined inside a waveguide to probe the waveguide surface via a leaky mode without direct transmission of light through the sample rendering it particularly useful for opaque or highly scattering samples.

3.2.1 Total Internal Reflection

An evanescently guided field is generated at the interface between an optically denser waveguide (refractive index n_1) and an optically rarer adjacent medium (refractive index n_2 ; with $n_1 > n_2$) if the condition of total internal reflection (TIR) is fulfilled¹. In TIR, light is coupled into a waveguide of higher refractive index than the surrounding medium and is internally guided by total internal reflection as shown in Figure 3-2 from both a ray and mode optics perspective.

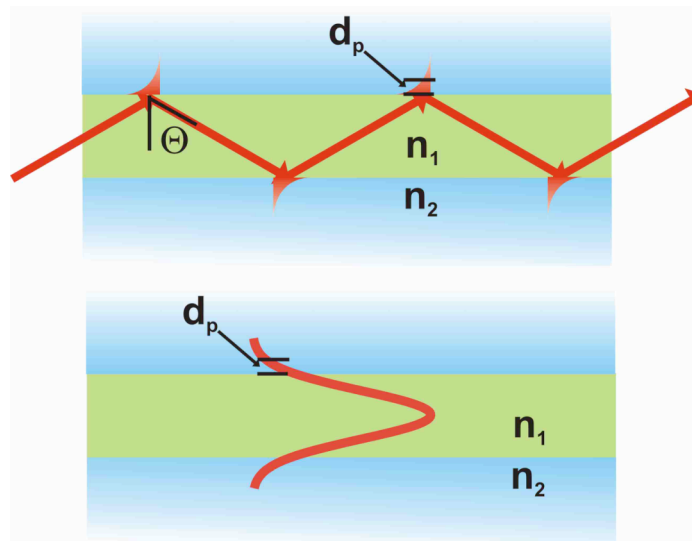


Figure 3-2: Total Internal Reflection (TIR) shown from a ray optics perspective (top) and a modal perspective (bottom).

The guided mode extends beyond the waveguide surface into the surrounding medium generating an evanescent field propagating along this interface. Absorbing species present within the penetration depth of the evanescent field interact with evanescently guided radiation similar to conventional transmission absorption spectroscopy resulting in attenuation total reflection (ATR)² for the frequencies where resonant energy transfer to vibrational or rotational transitions may occur.

The penetration depth of the evanescent field can be calculated by:

$$d_p = \frac{\lambda}{2\pi\sqrt{n_1^2 \sin^2 \theta - n_2^2}} \quad (\text{Eqn 3.3})$$

where d_p is the penetration depth, λ is the wavelength of the in-coupled radiation, n_1 is the refractive index of the waveguide, n_2 is the refractive index of the surrounding medium, and θ is the in-coupling angle.

3.2.2 Total Internal Reflection in Chemical Sensing

Due to the dependence of the penetration depth on the wavelength as evident from Eqn 3.3, evanescent field sensing based on broadband light sources is characterized by a distribution of penetration depths, while lasers emitting a single frequency or a narrow emission band provide a well characterized penetration depth (e.g. d_p is approx. 2 μm for a silver halide waveguide with $n_1 = 2.1$, $\theta = 45^\circ$, and $\lambda = 10 \mu\text{m}$). Figure 3-3 shows the change in penetration depth by wavelength across the MIR spectral range.

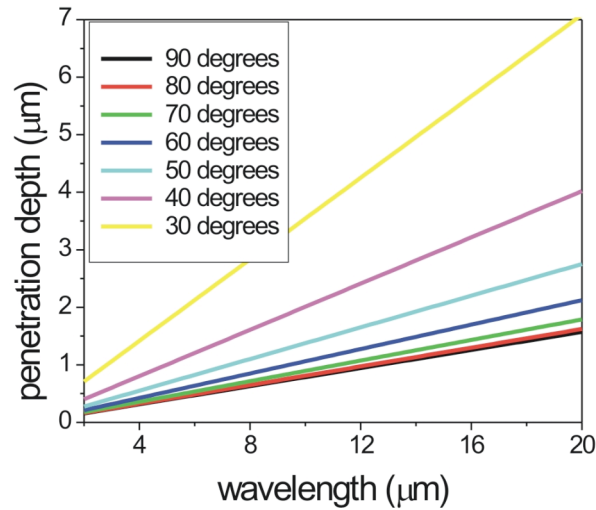


Figure 3-3: Penetration depth as a function of wavelength per in-coupling angle for a waveguide with refractive index of 2.1 and a refractive index of 1 for the surrounding medium.

The penetration depth for a given optical system is also dependent on the in-coupling angle of the radiation as shown in Figure 3-3, which provides curves for the penetration depth as a function of wavelength at angles of 30 ° (near the critical angle for the considered refractive index contrast) to 90 °. As a typical multimode fiber can accept a large range of in-coupling angles, the distribution of the evanescent field penetration depth changes significantly with the coupling conditions.

The refractive index contrast between the waveguide and the surrounding matrix dictates the confinement of the radiation and, therefore, affects the penetration depth of the evanescent field as shown in Figure 3-4.

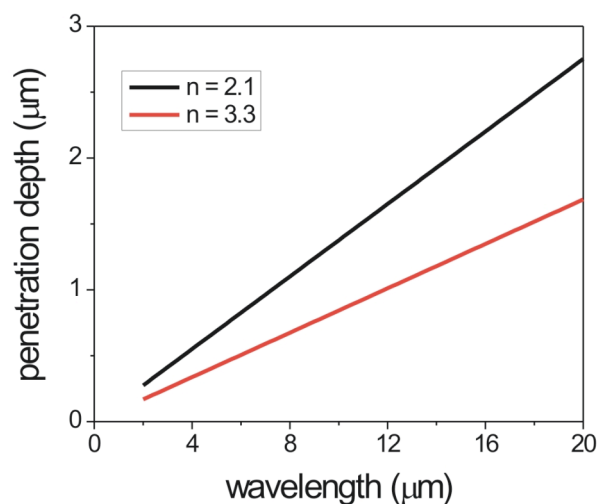


Figure 3-4: Penetration depth as a function of wavelength by refractive index 2.1 (AgX) and 3.3 (GaAs).

As shown in both Figure 3-4 and Eqn 3.3, a larger contrast in refractive index will give a shallower penetration of the evanescent field into the surrounding medium. As refractive indices are typically approximated as constant during an ATR measurement, quantitative results are not affected by a change of refractive index. In cases where the refractive index of the surrounding material changes significantly (such as for large concentration changes or sensors with a polymer membrane which swells during the measurement), a background absorption is typically measured. This background gives a ratio measurement and allows any changes in light intensity due to a refractive index change to be neglected. However, this parameter can be useful in waveguide design considerations as discussed in Chapter 5.

3.2.3 IR Evanescent Field Sensing Platforms

Typical platforms for evanescent field or ATR sensing in the MIR are ATR prisms and solid core cylindrical fibers. ATR prisms are typically rods or trapezoidal shaped, and fabricated from materials such as zinc selenide (ZnSe) or germanium (Ge) with a refractive index (at 10 μm) of 2.4 and 4, respectively. Other materials available for MIR transparent ATR rod or prism fabrication include thallium bromide-iodide (KRS-5), thallium bromide-chloride (KRS-6), and silicon (Si).

MIR transparent fibers are typically made from materials such as polycrystalline silver halides, crystalline sapphires, or chalcogenide glasses, and will be discussed in more detail in Chapter 6.

3.2.4 Evanescent Field Dependence on Waveguide Geometry

Next to the coupling conditions and the refractive index contrast, the intensity of the evanescent field strongly depends on the waveguide geometry^{3,4}, such as the fiber diameter in case of fiberoptic evanescent field sensors, or the waveguide thickness in case of a planar waveguide geometry. Many studies have shown that decreasing the fiber diameter or tapering a section of the fiber increases the intensity of the evanescent field, and thereby improves the sensitivity for the determination of molecular species present within the penetration depth of the evanescent field⁵⁻¹⁰.

The Lambert-Beer law as shown in Eqn 3.2 applies to evanescent field sensing systems with a modification defined as follows:

$$-\log I/I_0 = (\epsilon c l) r \quad (\text{Eqn 3.4})$$

where I/I_0 and ϵ are as described above, c is the concentration of absorbing analyte in the solution at the waveguide surface, l is the contact length along the waveguide, and r is the fractional power of the radiation guided outside the core of the waveguide in the evanescent field. This fractional power can be defined as¹¹:

$$r = \frac{4\sqrt{2}}{3V} \quad (\text{Eqn 3.5})$$

where V is the normalized frequency parameter defined as “V number”. For cylindrical fibers, V is defined as:

$$V = \frac{2\pi\rho}{\lambda} NA \quad (\text{Eqn 3.6})$$

where ρ is the fiber radius, λ is the wavelength of light, and NA is the numerical aperture of the fiber ($NA = (n_1^2 - n_2^2)^{1/2}$, where n_1 is the core refractive index and n_2 is the cladding or surrounding layer refractive index).

Planar waveguides follow similar principles as cylindrical fibers. However, a planar waveguide geometry does not have radial symmetry causing equations governing properties of radiation in the waveguide to be more complex than those of cylindrical

fibers. As the definition of fractional power outside the fiber core and V number presented here are qualitatively the same for planar waveguides, they will be used throughout this thesis to explain their dependence on waveguide geometry parameters. Beam propagation simulations will be presented in chapter 5 providing quantitative analysis of planar slab waveguides.

As the fractional power in the core inversely depends on the V number, minimizing this number will give the highest intensity in the evanescent field at a fiber interface and, therefore, the most sensitive measurements of molecules at the fiber surface. Minimizing the V number can be achieved by minimizing the fiber radius. The dependence of the V number on the wavelength of light indicates that for a broadband light source the system would have a distribution of V numbers and, therefore, of fractional powers in the core. This represents an advantage for single mode light sources over broadband sources, as a distribution of evanescent field intensities is not ideal for quantitative sensing applications.

A single mode waveguide matched to the emission frequency of a corresponding DFB laser light source would maximize the intensity of the radiation guided outside the waveguide in the evanescent mode. As the thickness of a waveguide supporting a single light mode varies with the wavelength, waveguides need to be designed for each wavelength of interest for maximizing the achievable sensitivity, which is the inherent potential of laser-based evanescent field sensing systems.

QCLs emitting monomode (TM₀₀) radiation are an ideal platform component for highly integrated on-chip IR evanescent field sensing systems with frequency-matched waveguides. The design of such waveguides will be discussed in Chapter 5 with demonstration of their application to chemical sensing presented in Chapter 6.

REFERENCES

1. Harrick, N. J., *Internal Reflection Spectroscopy*. Harrick: Ossining, N.Y., 1979.
2. Fahrenfort, J., Attenuated Total Reflection. A New Principle for the Production of Useful Infrared Reflection Spectra of Organic Compounds. *Spectrochimica Acta* **1961**, 17, 698-709.
3. Simhony, S.; Schnitzer, I.; Katzir, A.; Kosower, E. M., Evanescent Wave Infrared Spectroscopy of Liquids Using Silver Halide Optical Fibers. *Journal of Applied Physics* **1988**, 64, (7), 3732-4.
4. Messica, A.; Greenstein, A.; Katzir, A., Theory of Fiber-Optic, Evanescent-Wave Spectroscopy and Sensors. *Applied Optics* **1996**, 35, (13), 2274-2284.
5. Plunkett, S. E.; Propst, S.; Braiman, M. S., Supported Planar Germanium Waveguides for Infrared Evanescent-Wave Sensing. *Applied Optics* **1997**, 36, (18), 4055-4061.
6. Karlowatz, M.; Kraft, M.; Eitenberger, E.; Mizaikoff, B.; Katzir, A., Chemically Tapered Silver Halide Fibers: An Approach for Increasing the Sensitivity of Mid-Infrared Evanescent Wave Sensors. *Applied Spectroscopy* **2000**, 54, (11), 1629-1633.
7. Le Coq, D.; Michel, K.; Fonteneau, G.; Hocde, S.; Boussard-Pledel, C.; Lucas, J., Infrared Chalcogen Glasses: Chemical Polishing and Fiber Remote Spectroscopy. *International Journal of Inorganic Materials* **2001**, 3, (3), 233-239.
8. Vongsvivut, J.; Shilov, S. V.; Ekgasit, S.; Braiman, M. S., Symmetrically Tapered <30-Mm-Thick Quasi-Planar Germanium Waveguides as Chemical Sensors for Microanalysis. *Applied Spectroscopy* **2002**, 56, (12), 1552-1561.
9. Vongsvivut, J.; Shilov, S. V.; Ekgasit, S.; Braiman, M. S., Symmetrically Tapered <30-Micron-Thick Quasi-Planar Germanium Waveguides as Chemical Sensors for Microanalysis. *Applied Spectroscopy* **2002**, 56, (12), 1552-1561.
10. MacDonald, S.; Michel, K.; LeCoq, D.; Boussard-Pledel, C.; Bureau, B., Optical Analysis of Infrared Spectra Recorded with Tapered Chalcogenide Glass Fibers. *Optical Materials (Amsterdam, Netherlands)* **2004**, 25, (2), 171-178.
11. Ruddy, V.; MacCraith, B. D.; Murphy, J. A., Evanescent Wave Absorption Spectroscopy Using Multimode Fibers. *Journal of Applied Physics* **1990**, 67, (10), 6070-4.

CHAPTER 4

QCL-BASED GAS PHASE SENSING

In this chapter, gas sensing systems using glass and photonic bandgap hollow waveguides are presented along with background on applications of gas sensing, the state-of-the-art techniques, and the development and theory of the waveguides utilized.

4.1 Motivation

Due to the strong and distinct absorption features of organic compounds in the MIR, gas sensing in this spectral region is useful to many applications, and it has the potential to be sensitive as well as selective. QCL-based gas phase sensing is particularly applicable to applications which simultaneously require high sensitivity, compact devices, simple operation, and fast response times such as breath analysis and atmospheric monitoring.

4.1.1 Breath Analysis

Breath analysis is a non-invasive medical diagnostic technique, which has been steadily attracting interest in recent years. There are over 200 compounds present in exhaled breath¹, many of which are amenable to the diagnosis of various medical conditions when measured accurately at very low concentration levels (typically low ppb range). Breath analysis studies are currently performed using techniques such as chemiluminescence, electrochemical sensors, and gas chromatography². Furthermore, recent efforts using compact ion mobility spectrometers have been reported³. Table 4-1 shows examples of

gaseous compounds found in breath, the condition affecting their levels, and the sensitivity required for monitoring.

Table 4-1: Selected compounds relevant to breath analysis.

Gas	Condition affecting concentration	Normal concentration	Abnormal concentration
Nitric Oxide (NO) ²	Airway inflammation/ Asthma	10 ppb	> 15 ppb
Carbon Dioxide (CO ₂) ²	Cystic Fibrosis	2 ppm	5 ppm
Isoprene ⁴	Chronic Heart Failure	1.2 ppb	0.7 ppb
Ethane ⁵	Liver disease	100 ppt	400 ppt
Dimethylsulfide ⁵	Liver disease	1 ppb	5 ppb

The analytical challenge in breath analysis is achieving the high sensitivities needed for accurate diagnosis, while maintaining a small sample volume and simple-to-use system. Many gas sensing techniques are capable of achieving the necessary sensitivity levels using large multipass gas cells, which would be impractical for exhaled breath as their volumes are typically on the order of several hundreds of milliliters to liters.

4.1.2 Atmospheric Monitoring

Atmospheric monitoring requires sensitive detection of gases over large spatial regions due to perturbations in the chemical composition of the atmosphere particularly of carbon containing gases which affect air quality and climate change. The need for quantitative measurement techniques of these gases has been outline by the *Strategic Plan of the U.S. Climate Change Science Program*⁶. This program outlines the need for monitoring of pollutant emission, atmospheric transport, climate change, and air quality. Table 4-2

shows examples of atmospheric gases of interest along with concentration levels, precision levels, and response times needed for monitoring of each gas.

Table 4-2: Selected target gases for atmospheric monitoring

Atmospheric gas	Concentration level	Precision level	Required response time [s]
Carbon dioxide (CO ₂)	350 ppmv	± 1 ppmv	100
Carbon monoxide (CO)	60 ppbv	± 10 ppbv	100-10
Methane (CH ₄)	1.7 ppmv	± 50 ppbv	100-10

Selected target gases shown in table 4-2 were identified through collaboration with Judith Curry, David Tan, and Greg Huey from the Earth and Atmospheric Sciences department at Georgia Tech. From a list of many environmentally interesting atmospheric gases, these compounds were determined to be well-suited to monitoring with a QCL-based sensing system due to their relatively high concentration and precision levels as well as response times.

Frequently, monitoring is performed using unmanned aerial vehicles (UAVs)⁷ for applications such as plume tracing above urban areas and in the atmospheric boundary layer. Currently, atmospheric gas sensing is often performed with optical sensing techniques such as tunable diode laser (TDL) spectrometers⁸⁻¹³ due to their compact size and ability to achieve the required low detection limits. As QCLs are characterized by similar advantages while additionally providing greater flexibility in the availability of appropriate emission wavelengths, their application to the field of atmospheric monitoring is of significant interest. The analytical challenge in sensing of atmospheric

gases is not only achieving the required sensitivity, but also the demanded high precision level as comparatively small changes in concentration are highly relevant in this field.

4.2 State-of-the-art in Laser-Based Gas Sensing

At its most sensitive, gas sensing in the mid-infrared (MIR) spectral range is able to achieve sensitivities in the ppb and sometimes ppt range. The most sensitive techniques used are briefly discussed below.

4.2.1 Multipass Transmission Absorption Spectroscopy

The most common IR gas sensing technique utilizes multipass transmission cell such as a Herriott¹⁴ or White¹⁵ cell. These cells consist of a chamber filled with analyte gas with mirrors at the ends, which fold the beam back and forth through the cell creating an extended yet defined optical pathlength in a small volume providing both high sensitivity and a relatively compact overall size of the system. Multipass cells have the disadvantage of comparatively large volumes (typically on the order of liters), which leads to extended sample residence times and, consequently, an inadequate system response times for continuous sensing applications aiming at resolving concentration fluctuations at small time scales.

4.2.2 Photoacoustic Spectroscopy

Photoacoustic spectroscopy¹⁶ relies on the photoacoustic effect for the detection of absorbing analytes. The sample gas is sealed into a confined space where modulated (e.g. chopped) light can enter via an IR transparent window to be absorbed by IR-active molecular species. Thereby, the temperature of the gas increases leading to periodic expansion and contraction of gas volume synchronous with the modulation frequency of the radiation. This produces a pressure wave, which can be acoustically detected via

simple microphones providing high sensitivity measurements and small sample volumes . A significant disadvantage to this technique is its sensitivity to vibrational noise. As measurements are based on an acoustic signal, external vibrations cause noise in the system reducing the sensitivity achievable.

4.2.3 Cavity Ring-down Spectroscopy

Cavity ring-down (CRD) spectroscopy¹⁷ confines gas in an optically reflective cavity where radiation is introduced by a laser. The amplitude of the radiation is monitored, which decays at a certain rate in the absence of absorption. Once absorbing sample gas is introduced, the rate of decay increases indicating the presence of an absorbing species. This technique provides high sensitivity, but involves a delicate optical set-up as well as difficult data interpretation. As the measured parameter is the rate of decay of the light intensity, the decay due to absorption from the analyte of interest must be separated from decay due to mirror and other cavity dependent losses.

4.2.4 Integrated Cavity Output Spectroscopy

A variation of CRD spectroscopy is integrated cavity output spectroscopy (ICOS)¹⁸. In this technique, the cavity output is integrated providing an absorption spectrum as the source is scanned across wavelengths. This technique provides sensitivity levels comparable to that of CRD, but with a simpler data analysis.

4.2.5 Differential Absorption LIDAR

Light detection and ranging (LIDAR) is a technique commonly used in atmospheric sensing where light from a source is transmitted over a distance to a target and is partially reflected back to a detector. Changes in the light properties return information about the target or compounds in the distance between the source and target. Differential absorption LIDAR (DIAL) can be used to measure atmospheric gases or pollutants¹⁹ by a ratio of the intensity of a beam which is absorbed to one which is not.

4.2.6 Quantum Cascade Lasers in Gas Sensing

Despite their comparatively young history, QCLs have already successfully been applied in various gas sensing formats due the wide range of available emission frequencies^{20-21, 22}. Sensitive detection of gaseous species with QCL technology has been reported by photoacoustic spectroscopy²³⁻²⁵ as well as by quartz-enhanced photoacoustic spectroscopy²⁶. The latter technique demonstrated the detection of N₂O down to a concentration of 4 ppb. Demonstration of QCLs in cavity ringdown spectroscopy has lead to a detection limit of 0.7 ppb of NO in N₂²⁷. Application of these laser sources in integrated cavity output spectroscopy has achieved detection of less than 1 ppb of NO in human breath samples^{28, 29}.

QCLs have also been applied in gas sensing for transmission spectroscopy including applications such as atmospheric monitoring³⁰, cigarette smoke analysis³¹, NO detection^{32, 33-36}, and vehicle emission analysis^{37, 38}. Most QCL transmission spectroscopy measurements utilize a multipass gas cell to achieve the desired sensitivities, however,

hollow waveguides (HWGs) have recently been applied as well, and will be discussed below.

Consequently, QCL-based sensing systems have become commercially available for a limited set of analytes. Aerodyne Research, Inc.³⁹ (Billerica, MA) produces a gas analyzer with room-temperature pulsed QCLs coupled to a 56 m pathlength multipass gas cell capable of detecting N₂O, CH₄, and NH₃ down to low ppb levels. Physical Sciences, Inc.⁴⁰ (Andover, MA) provides two QCL systems with wavelengths at 5.2 μm and 4.6 μm capable of detecting 10 ppb concentrations of NO and CO gas, respectively, with pathlengths of 1 m. Cascade Technologies⁴¹ (Glasgow, Scotland) is producing a Micro Gas Sensor capable of sub ppm detection with a compact size of 200 x 400 x 200 mm and an Ultra Gas Sensor capable of ppt level detection.

4.3 Hollow Waveguides

Hollow waveguides were originally developed as a power delivery system for surgical lasers, such as the CO₂ laser operating at 10.6 μm, and were later applied to gas sensing⁴². These guides consist of a reflective tube with a hollow air core, which transmits radiation by reflection off the HWG inner wall. This air core allows usage with high power lasers needed in surgical applications without the concern of melting at the high temperatures created upon heating by MIR radiation, as e.g. in solid core fibers. The typical transmission range of 2 to 15 μm^{43, 44} renders HWGs ideally suited for MIR sensing applications.

Conventional HWGs are classified in two distinct types depending on the light guiding mechanism: (i) attenuated total reflection (ATR) waveguides, and (ii) leaky mode waveguides. ATR guides consist of a tube made from material with refractive index (n) less than that of the air core ($n=1$), while leaky guides are composed of a tube coated on the inside with material of $n>1$. Leaky guides are much more common and are exclusively used during the studies presented here.

4.3.1 History

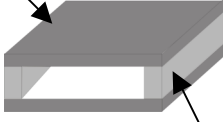
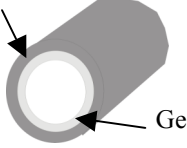
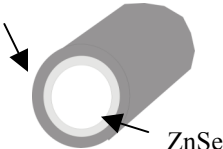
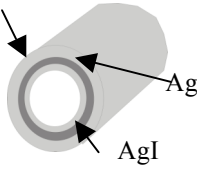
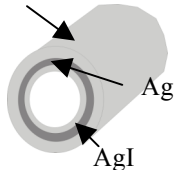
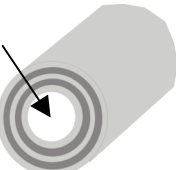
HWGs were first produced by Garmire⁴⁵ in the late 1970's consisting of two strips of aluminum separated by dielectric spacers as shown in table 4-3. The rectangular cross-section of these waveguides was responsible for substantial optical losses not only during bending but also during twisting of the waveguides.

Miyagi⁴⁶ produced the first cylindrical HWGs by plating nickel and then sputtering germanium inside an aluminum pipe, which was then removed leaving a nickel tube coated with germanium at the inside. Layering a dielectric coating on top of the reflective metal provided an increase in reflectivity due to an interference pattern established as a result of the dielectric film. Thin-films are deposited at a thickness which interacts with the wavelength of operation causing interference and therefore minimized losses at that wavelength. This type of structure was used for all future waveguide structures of similar architecture.

Miyagi's Ni/Ge design was later improved by using a silver tube coated at the inside with zinc selenide (ZnSe)⁴⁷ yielding a waveguide with much lower losses. HWGs based on plastic structural tubes were first presented by Croitoru⁴⁸. These guides had reflective layers of silver and silver iodide, which provided a distinct processing advantage as they could be formed by passing iodine gas over the silver layer already present at the inside of the waveguide reducing the number of deposited layers and processing steps.

Glass structural tubes with Ag/AgI were introduced by Harrington⁴⁹, which have the advantage of a very smooth inner surface for the deposition of the silver layer resulting in a lower surface roughness of the final HWG, which in turn leads to lower optical losses. The latest generation of HWGs utilizes an architecture consisting of cylindrical layers of glass and plastic, which creates a one-dimensional photonic bandgap material promising lower bending losses in contrast to conventional HWGs. These waveguides will be discussed in the next section.

Table 4-3: Selected milestones in the development of HWG technology.

Year	Authors	HWG description	HWG schematic	Losses (@ 10.6 μm)	Improvement
1976	Garmire <i>et al.</i> ⁴⁵	Al strip with dielectric spacers; rectangular	Al Strip  Dielectric spacer	0.22dB/m	First HWG; higher powers can be transmitted
1983	Miyagi <i>et al.</i> ⁴⁶	Ge coated Ni tube; cylindrical	Ni Tube  Ge	0.5dB/m	Eliminated losses due to twisting of
1990	Matsuura <i>et al.</i> ⁴⁷	ZnSe coated Ag tube	Ag tube  ZnSe	0.021dB/m	Much lower losses with silver compared to nickel
1992	Dahan <i>et al.</i> ⁴⁸	Ag/AgI coated plastic tube	Plastic tube  Ag AgI	0.5dB/m	Very flexible; simple and cheap in fabrication
1994	Abel <i>et al.</i> ⁴⁹	Ag/AgI coated glass tube	Glass tube  Ag AgI	0.15dB/m	Smooth inner surface
1999	Fink <i>et al.</i> ⁵⁰	Alternating plastic and glass layers	PBG material 		Lower bending losses

4.3.2 Photonic Bandgap Hollow Waveguides

Photonic bandgap (PBG) fibers are a fundamentally new type of HWGs. PBG materials (also known as ‘photonic crystals’) are periodic structures of dielectric materials where the periodicity enables controlling light inside the crystal in a way analogous to that of electrons in a semiconductor material. The periodic dielectric constant creates diffraction patterns prohibiting photons of certain frequencies from propagating inside the crystal. Resulting, the PBG acts as a perfectly reflecting mirror for these frequencies, which can be tailored (in frequency) by changing the crystal feature size. Figure 4-1 shows an example of one-, two-, and three-dimensional photonic crystal structures.

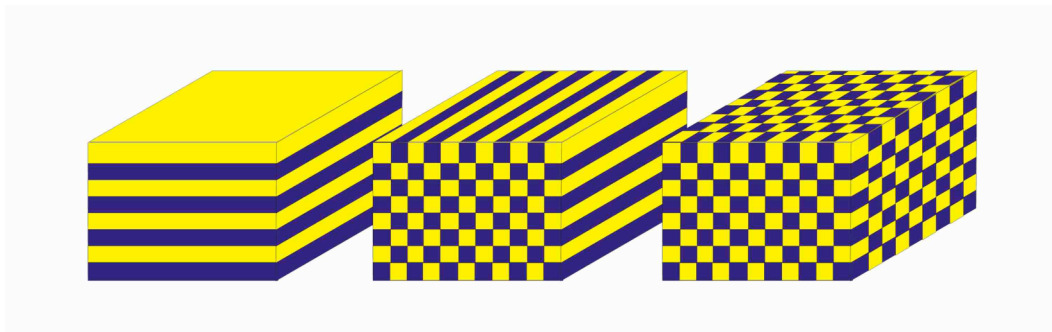


Figure 4-1: Photonic crystal structures with periodicity in 1-D (left), 2-D (center), and 3-D (right).

To create a complete PBG where light is controlled in all directions, a three-dimensional crystal is needed. A linear defect in a 3-D crystal would act as a waveguide, however, this is difficult to manufacture.

Cregan *et al*⁵¹ developed the first PBG fibers in 1999, which guided light in an air core. These waveguides utilized a honeycomb structure made from silica with air gaps. The structure of the fiber cross-section is shown in Figure 4-2a . The honeycomb pattern creates the periodic refractive index modulation leading to a photonic bandgap with radiation confined to the central defect air hole and guided along the length of the fiber. Another type of PBG fiber is the omnidirectional guide developed in 2002 by the Fink group^{52,53} and the Miyagi group⁵⁴. The cross-section structure of these materials is shown in Figure 4-2b consisting of materials with alternating refractive index forming a cylindrical layer stack. This configuration creates a one-dimensional photonic crystal wrapped into a cylindrical shape with a hollow center in which light is guided.

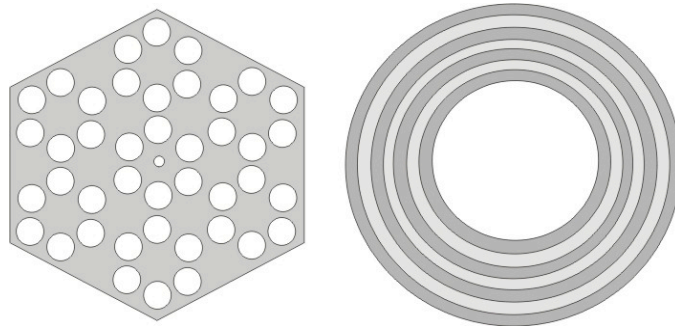


Figure 4-2: Schematic PBG HWG cross sections of (a) honeycomb type structures (light is confined to the central defect hole) and (b) omnidirectional guide (light is confined by cylindrical 1D photonic crystal layers).

While light in honeycomb type structures^{55,56} is confined to the small central air hole, the omnidirectional guides feature a large open hollow core whose dimensions are uncritical to the frequency of light reflected from the HWG walls. The latter structure is therefore more useful in sensing applications where the waveguide simultaneously serves as a gas

cell accommodating the gas sample in the hollow core. Photonic crystal fibers have also been demonstrated using a honeycomb structure with a large central defect hole⁵⁷. These fibers also have potential in gas sensing applications.

The thickness of the dielectric cylinders in an omnidirectional guide can be varied enabling tuning of the bandgap to confine selected frequencies of light. These omnidirectional guides are currently being commercially produced by OmniGuide Communications Inc. (Cambridge, Mass.) for use with CO₂ laser frequencies (10.6 μm) in surgical applications. The transmission spectrum of these fibers is shown in Figure 4-3.

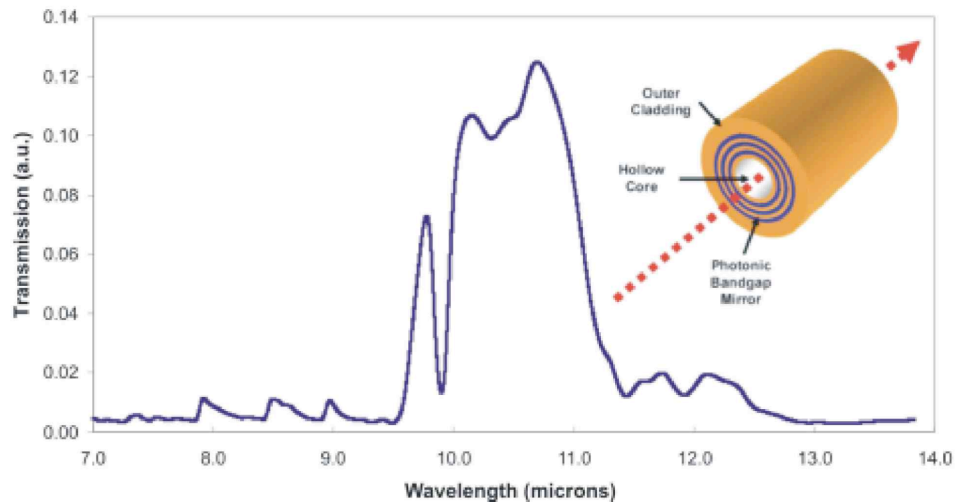


Figure 4-3: Transmission spectrum of a commercially produced OmniGuide Fiber designed to transmit light at 10.6 μm with OmniGuide schematic (inset). (Image courtesy of OmniGuide Communications Inc.)

The area of high transmission centered around 10.6 μm shown in Figure 4-3 corresponds to the bandgap created by the cylindrical layers forming the waveguide structure. Light in this frequency range would be reflected off the walls of the fiber and transmitted along the hollow core.

As the production of these fibers is easily tunable for other frequencies, OmniGuide fibers are ideal for laser-based integrated gas sensing devices, where the emission frequency of the light source is matched with a selective absorption line of an analyte.

4.3.3 Losses in Hollow Waveguides

Attenuation in HWGs has been extensively studied and is most frequently reported based on the fundamental studies of Marcatili and Schmeltzer⁵⁸. However, these studies use microwave wavelengths and are of limited value in the IR⁵⁹. Miyagi et. al. have studied losses in HWGs at IR wavelengths for both metallic and dielectric coated metallic waveguides⁶⁰.

Losses in HWGs depend on many factors, which have to be considered in their design including the coated layers (metallic and dielectric) and their properties (thickness, surface roughness, and refractive indices), bore size or inner diameter, and transmitted radiation (mode and phase). Additional losses appear when the waveguide is bent. For the purpose of the present work, the two aspects of interest are the bore size dependence and the bending losses as these are factors which are currently controllable until dedicated waveguides will be manufactured.

To determine the dependence on bore size, we use the general loss equation developed by Miyagi and Kawakami⁶⁰ for dielectric coated metallic HWGs:

$$\alpha = n_0 k_0 \frac{u_0^2}{(n_0 k_0 T)^3} F \quad (\text{Eqn 4.1})$$

where α is the attenuation coefficient, T is the bore radius, n is the refractive index, k and u are parameters from the film and mode, and F is a loss factor based on the phase and mode of the light. This equation shows that the dependence of attenuation on the bore radius is $\alpha \propto 1/T^3$ and, therefore, the attenuation decreases rapidly as the inner diameter of the hollow waveguide increases.

Miyagi et. al.⁵⁹ have also described bending losses according to wave theory by:

$$\alpha_B = \alpha \left\{ 1 - \frac{1}{6} \left(\frac{n_0 k_0 T}{u_0} \right)^4 \left(\frac{T}{R} \right)^2 \right\} \quad (\text{Eqn 4.2})$$

where α_B is the loss due to bending, R is the radius of the bend, and all other variables are as described above. Hence, the bending losses are directly proportional to $1 - 1/R^2$ or, as the radius of the bend decreases (the bend becomes tighter), the losses due to bending increase.

4.3.4 Hollow Waveguide in IR Gas Sensing

In our studies HWGs are used in gas sensing devices as both a waveguide and gas transmission cell. Similar to multipass cells, they provide an extended optical pathlength yielding high sensitivity measurements. Their advantage over conventional multipass gas

cells is that they have a much smaller sample volume (typically on the order of one mL) and, therefore, provide a smaller dead volume and a faster response time.

Spectroscopy inside a HWG⁶¹ was first demonstrated in the 1980's in GC/IR measurements using 'light-pipe' technology^{62, 63}. Harrington et. al.⁶⁴ recorded a spectrum of CO₂ inside a HWG in 1991, and Saito et. al. introduced the use of a HWG as a gas transmission cell in 1993 by measuring NH₃ gas with a CO₂ laser.⁶⁵ Following these works, HWGs were applied in FT-IR spectroscopy for the detection of aromatics extracted from soil⁶⁶ and pollutants extracted from water⁶⁷⁻⁶⁹, as well as for cigarette smoke analysis. HWGs have also been coupled to CO₂ lasers for sensing of ethylene^{70, 71} and NH₃⁶⁵.

HWGs coupled to QCLs were first demonstrated in gas sensing by Hvozdar et. al.⁷² detecting ethylene gas down to a concentration of 250 ppm. This system utilized a waveguide with an inner diameter of 2 mm with an FTIR spectrometer coupled to the distal end of the waveguide to resolve the measurements by wavenumber.

Fetzer et. al. demonstrated HWG-QCL³⁶ sensing with a 1 mm inner diameter waveguide building on their previous works with tunable diode lasers coupled to a HWG⁷³. This system utilized a coiled waveguide with a length of 9 m, and was able to detect nitric oxide down to a concentration of 60 ppb.

The studies in this thesis demonstrate gas sensing with a QCL coupled to both a silica HWG⁷⁴ and a PBG HWG⁷⁵. Silica HWG work is performed as a follow-up to the works

by Hvozدارa et. al.⁷² and was performed simultaneous to that of Fetzer et. al.³⁶ The PBG HWG system was developed as the next generation device concept after the silica HWG studies, and is the first demonstration of sensing inside a PBG material. These works are discussed in the following sections.

4.4 Silica Hollow Waveguide Sensing System

The gas sensing system developed in this study⁷⁴ uses a silica HWG as both a waveguide and a miniaturized gas cell demonstrating gas sensing with a QCL at high sensitivity levels and with rapid response times.

4.4.1 Experimental

The HWG used in this study was developed by Croitoru et al^{76,77} at Tel Aviv University and consists of a silica glass tube coated at the inside with a reflective silver layer and a thin layer of silver iodine to create a stable and inert infrared reflective coating for leaky mode waveguiding. A polymer coating around the outside of the silica structural tube improves mechanical robustness. The HWG had a length of 4 m and an inside diameter of 700 μm resulting in an internal volume of approximately 1.5 mL. A schematic of the waveguide cross section is shown in Figure 4-4.

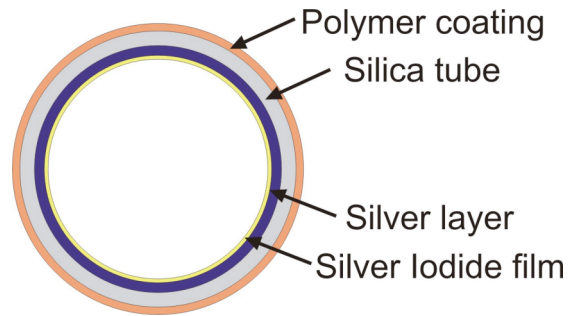


Figure 4-4: Glass HWG Cross Section.

The quantum cascade laser (laser s1537) was operated at a pulse width of 200 ns using a repetition rate of 22 kHz. The pulse amplitude was set to 11 V, which is sufficiently low

to avoid saturating the detector. The temperature of the laser was kept constant at 283 K via Peltier cooling throughout all experiments.

Custom made gas cells (shown in Figure 4-5) are sealed around each end of the hollow waveguide, which provide an inlet and outlet for the analyte gas and feature infrared transparent ZnSe windows for simultaneously coupling laser radiation into and out of the HWG. The dead volume inside the gas cells is $< 5 \text{ mm}^3$ allowing gas to be injected directly into the HWG.

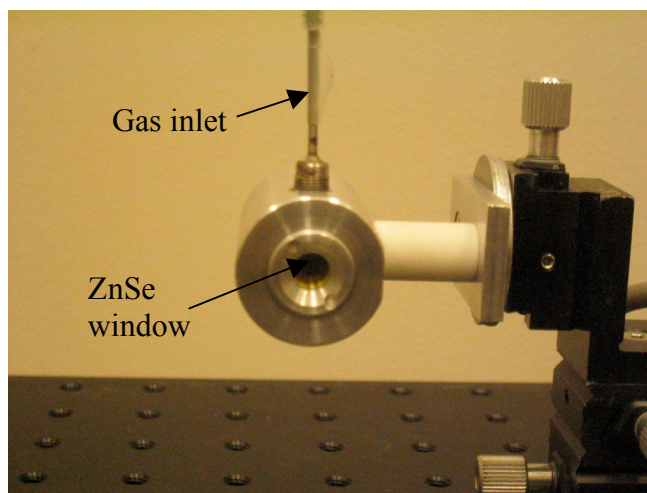


Figure 4-5: HWG gas cells.

The experimental setup for the gas sensing system is shown in Figure 4-6. The QCL is collimated and focused into the HWG through the window of the gas cell using a pair of off-axis parabolic mirrors (OAPMs) with a focal length of 2.54 cm. Radiation emitted from the distal end of the HWG was collected and focused onto the MCT detector element with a second pair of OAPMs.

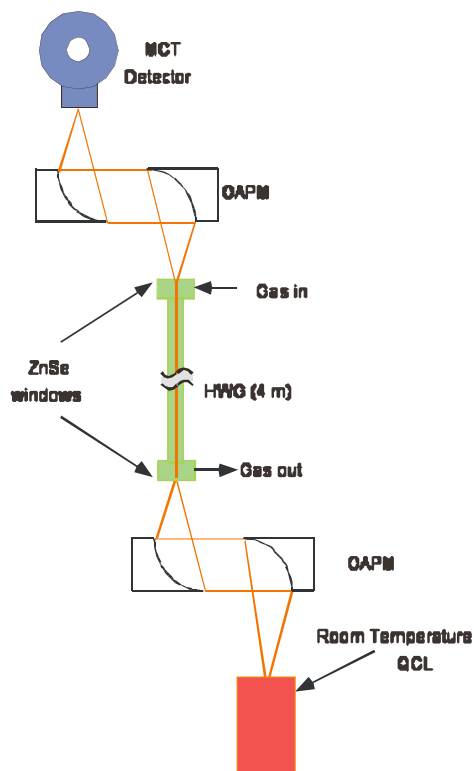


Figure 4-6: Experimental setup.

The fast response of the detector (bandwidth of 50 MHz) enabled the signal from a single laser pulse to be monitored with minimal time delay of the detector and preamplifier, while the signal was evaluated using an oscilloscope.

Ethyl chloride obtained from Airgas (Radnor, PA) was mixed with ambient air at different concentration levels, and was injected into the HWG gas cell. Gas concentrations were prepared by injecting a small volume of ethyl chloride collected from a gas sampling bag into a sealed glass vial with a volume of 211 mL using a gastight syringe. Each injection used 8 mL of gas mixture to ensure that the entire waveguide with a total internal volume 1.5 mL including the gas cells was filled with

sample gas. Damping of the laser signal due to absorption by the ethyl chloride molecules was then detected with the MCT detector and read out by the oscilloscope.

4.4.2 Results

The experimental setup described above provides a high optical throughput transmitting sufficient light through the entire system to saturate the detector in the absence of absorbing species. This strong signal through a long waveguide can be attributed to the emission power of the QCL (average power of 2 to 10 mW; peak power of 100 to 500 mW) as well as the efficient light guiding properties of the HWG (attenuation losses approx. 0.5 dBm^{-1} for straight guides). This efficient combination enables light-guiding over considerably large distances and has substantial potential for guiding infrared radiation to remote locations for sensing applications, such as environmental and process monitoring, and medical/biomedical applications of QCL technology. For the current application, the laser was driven with current pulses of low enough amplitude to avoid saturating the detector, enabling small changes in the signal to be detected.

The analyte concentration is determined by damping of the laser signal due to absorption of light inside the hollow waveguide at vibrational resonance frequencies of analyte molecules. Ethyl chloride gas has a strong absorption band at 974 cm^{-1} due to the ν_9 stretching vibration, which overlaps with the QCL emission line as shown in Figure 4-7 illustrating the transmission spectrum of ethyl chloride gas in comparison to the emission spectrum of the QCL.

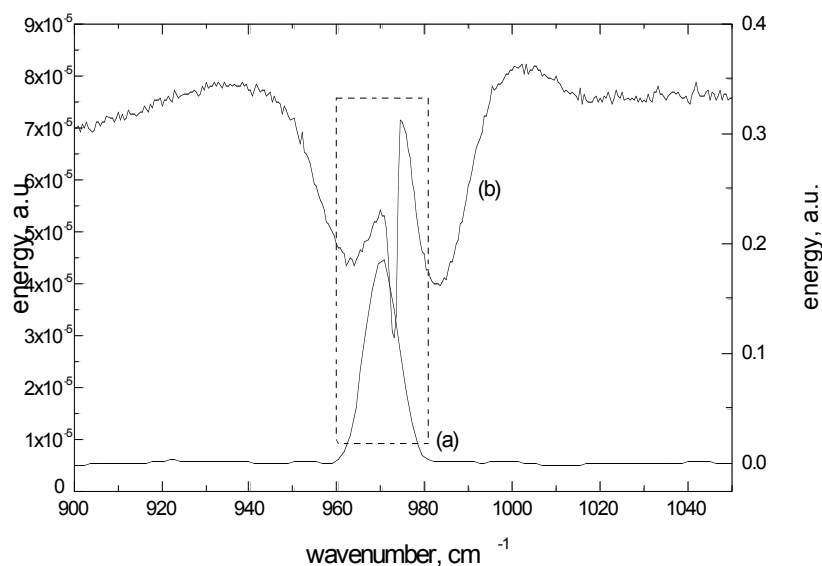


Figure 4-7: FTIR spectra of emission (curve a) and ethyl chloride absorption (curve b) band overlap.

The laser emission frequency best matches the absorption of ethyl chloride at 283 K. Therefore, the QCL was kept constant at that temperature throughout the measurements. The laser line at 971 cm^{-1} does not perfectly correspond to the analyte absorption band with the peak maximum located at 974 cm^{-1} , as shown in Figure 4-7. A QCL providing perfect overlap with the analyte absorption band would provide an improvement of the limit of detection by approximately 20 %.

Laser emission line overlap with the ethyl chloride absorption band causes increasing concentrations of ethyl chloride inside the waveguide to decrease the measured laser signal due to absorption of infrared radiation as governed by the Lambert-Beer law.

Figure 4-8 shows damping of the measured laser signal as the ethyl chloride concentration increases from 5 ppm (v/v) to 100 ppm (v/v) inside the waveguide.

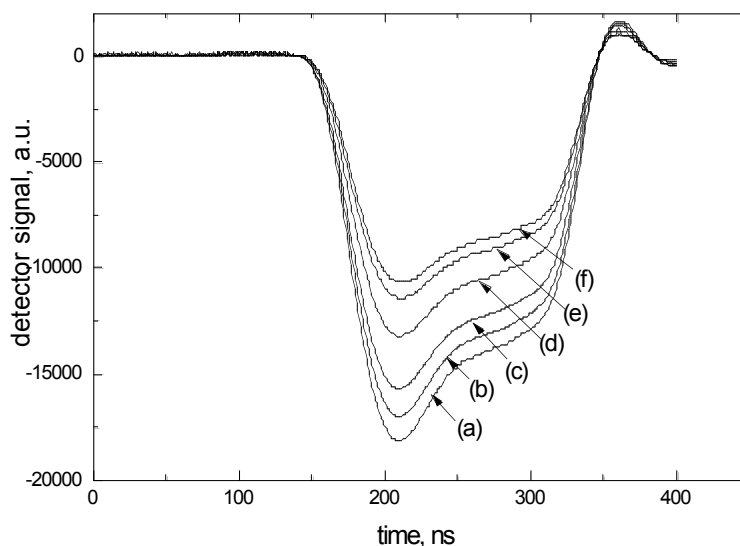


Figure 4-8: Damping of laser signal in presence of analyte for ethyl chloride in air concentration a) 0 ppm, b) 1 ppm, c) 5 ppm, d) 10 ppm, e) 15 ppm, f) 20 ppm.

Each curve represents a single laser pulse for a different concentration as measured by the oscilloscope. The non-Gaussian pulse shape is likely due to electronics as discussed in chapter 2, while the peak above zero is due to back-reflection from the ZnSe windows of the gas cells, as it is not observed with a simple system consisting of the laser and a room temperature MCT detector without a window in between. Higher concentrations of ethyl chloride gas inside the HWG give a larger absorption and therefore less light transmitted through the waveguide. This produces a smaller voltage signal, which is in accordance with Lambert-Beer's law demonstrating the feasibility of this measurement technique.

Calibration graphs correlating the concentration of the analyte to the integrated area of the laser signal are generated from the measurements shown in Figure 4-9. The absorbance is plotted as function of ethyl chloride concentration in Figure 4-9.

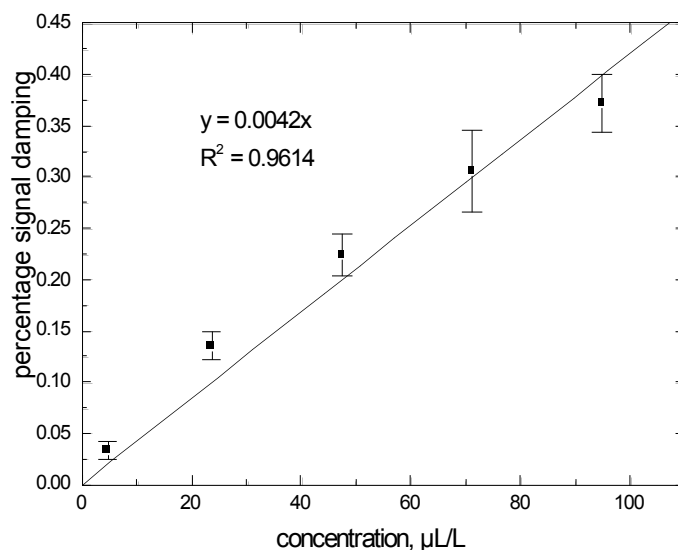


Figure 4-9: Percentage signal damping as a function of concentration of ethyl chloride in air present in the waveguide.

The system shows a linear response over the evaluated concentration range of 5 ppm (v/v) to 100 ppm (v/v). A linear regression line was fitted to the points and forced through the origin since the absence of analyte in the waveguide causes no damping, which fit with an R^2 value of 0.9614. Error bars indicate the reproducibility for each data point based on 5 measurements of individually prepared samples at each concentration. Larger error bars, as found for the signal corresponding to the concentration of 15 ppm

(v/v), are attributed to inaccuracy during manual preparation of the gas mixtures. This error is larger at the higher gas concentrations, as would be expected due to mixing of the gas mixture with ambient air during injection to the system. Based on the 3σ criterion with σ representing the average noise, the limit of detection for this system was calculated as 0.5 ppm (v/v). The main source of noise in the system results from pulse-to-pulse variations of the laser output power. With a laser emission frequency corresponding more precisely to the peak absorption of the analyte, the LOD would be lowered to approximately 0.4 ppm (v/v).

Previous studies by Hvozda et al⁷² utilized cryogenically cooled GaAs/AlGaAs QCLs coupled to a glass hollow waveguide with a length of 434 mm for gas phase infrared spectroscopy, and found a limit of detection of 250 ppm (v/v) for ethylene. The 4 m long hollow waveguide used here provides a significantly increased optical path length, which enables enhanced interaction between the laser light and absorbing molecules inside the volume of the HWG. The reported increased limit of detection with the current experimental configuration is mainly attributed to the increase of the optical path length. However, as the two setups are based on different QCLs and optical configurations, and probe different analytes, quantitative comparison of the results is not possible.

This increase in system sensitivity based on the increase of optical path length leads to consideration of utilizing yet longer waveguides. However, this would significantly increase the overall footprint of the sensing system. An extended optical path length yet maintaining a compact system would require utilizing a coiled or bent waveguide

geometry. Due to the high attenuation losses in bent silica HWGs resulting from coupling into the wall material, this configuration will not provide a significant improvement once the overall lower optical throughput is considered. Therefore, a new generation of HWGs based on photonic bandgap materials has been implemented for gas sensing.

4.5 Comparison of Bending Losses

Experiments to compare the bending losses of the glass HWG used above to the losses encountered in a photonic bandgap HWG were performed during a research stay at OmniGuide Communications Inc. in Cambridge, Massachusetts.

4.5.1 Experimental

A variety of waveguides were compared with a QCL source and a CO₂ laser in the configuration shown in Figure 4-10.

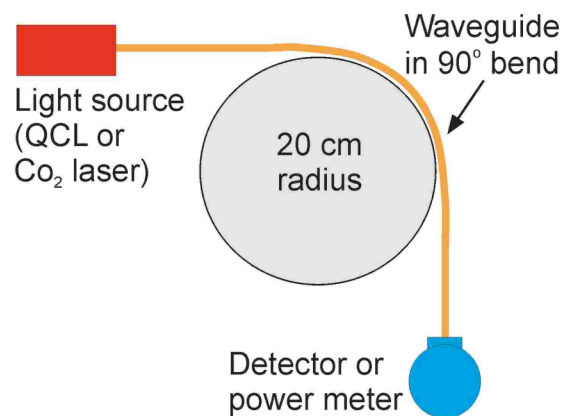


Figure 4-10: Experimental setup for the comparison of bending losses.

The laser light source was coupled into the waveguide, which was bent at 90° bend with a radius of curvature of 20 cm. The distal end of the waveguide was then coupled to a liquid nitrogen cooled MCT detector for the QCL configuration, or a power meter for studies using the CO₂ laser. Both the glass HWG and the PBG fiber had inner diameters of 700 μm and a length of 1 m enabling a direct comparison.

Light from the QCL is polarized perpendicular to the laser end facet, i.e. in the vertical direction for the typical laser orientation. For the photonic bandgap waveguide, bending losses are polarization dependent. As the waveguide consists of layers, which are compressed upon bending causing losses, a bend in the plane of polarization would be expected to result in higher losses. This configuration is termed the ‘high loss plane’, while light polarized perpendicular to the bend would correspond to the ‘low loss plane’. If figure 4-10 is considered a top-down view with the emitted laser radiation polarized out of the plane of the figure, this would represent the low-loss bending plane. A laser turned 90° to the side would couple into the high loss plane. The CO₂ laser radiation was circularly polarized and would be expected to provide losses that are between the two QCL polarization states for bends in the photonic bandgap waveguide.

4.5.2 Results

Table 4-4 shows a summary of the results of the bending experiments for both the glass HWG and the photonic bandgap waveguides for the CO₂ laser and both QCL polarizations.

Table 4-4: Comparison of bending results.

	QCL - High loss plane	QCL - Low loss plane	CO₂ - Circularly polarized
PBG fiber	1.69 dB	0.34 dB	0.86 dB
Glass HWG	9.85 dB		10.77 dB

The losses were calculated as the ratio of the signal transmitted through the waveguide with the bend to the signal through the straight waveguides. The losses are reported in decibels (dB) per specific bend.

As shown in table 4-4, the losses for the glass HWG were orders of magnitude higher than those of the PBG waveguide for both the QCL and the CO₂ laser. HWG bending losses are reported in literature to be approximately 1 dB for a 20 cm radius bend. This value differs significantly from the experimentally determined value reported in our studies. The difference can be attributed to defects in the HWG segments found during measurements by simultaneous imaging with an IR camera. The IR images revealed hotspots along the waveguide as radiation was transmitted, which increased significantly when bending the waveguide. Two separate segments were tested, and both of which had defects. However, even using the literature reported value of 1 dB for a 20 cm bend results in significantly higher losses than for the PBG waveguide in the low-loss bending plane.

It is of interest to note that the losses observed in the PBG waveguide follow the theory of a high loss and a low loss plane. A loss of 0.34 dB was determined for the low loss plane, while the high loss plane resulted in a loss of 1.69 dB. The circularly polarized radiation from the CO₂ laser gave a loss in between the two loss planes (0.86 dB), as predicted. In the silica HWG, the polarization state of the radiation did not make a significant difference.

4.6 Photonic Bangap Hollow Waveguide Sensing Systems

The sensing system developed in this study⁷⁵ uses an OmniGuide fiber as both a frequency selective waveguide and a miniaturized gas cell similar to the glass hollow waveguide discussed above.

4.6.1 Experimental

The system was designed providing a three-way overlap between the bandgap of the waveguide, the laser emission frequency, and the analyte absorption band as shown in Figure 4-11.

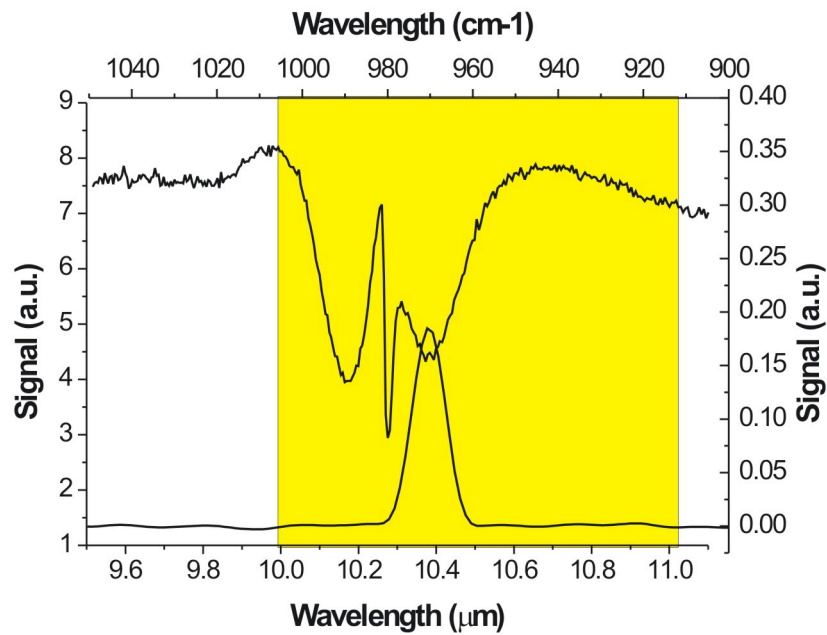


Figure 4-11: FT-IR spectra of the overlap between ethyl chloride absorption band (top) and laser emission band (bottom) with the OmniGuide fiber transmission range shown in yellow.

The QCL operating at 974 cm^{-1} ($10.3\text{ }\mu\text{m}$) with a pulse width of 40 ns, a period of 2.64 μs , a pulse amplitude voltage setting of 38 V, and an operation temperature of 5 °C was used to detect ethyl chloride gas similar to the silica HWG experiments detailed above. As shown in Figure 4-11, the QCL emission frequency matches with the absorption frequency of the C-H stretching vibration of ethyl chloride gas. The photonic bandgap of the used OmniGuide fiber also corresponds to this frequency band, as represented by the yellow area in Figure 4-11. As in the silica HWG experiments described above, the presence of ethyl chloride within the PBG hollow waveguide results in damping of the laser signal due to absorption by the gaseous molecules.

Light emitted from the QCL was coupled into a PBG fiber (OmniGuide Communications, Cambridge, MA) with a length of 1 m and an inner diameter of 700 μm using the same gas cells that were applied during the silica HWG studies, which had the same nominal outer diameter. Figure 4-12 shows microscope images of the hollow waveguide cross sections of both the OmniGuide fiber and the silica HWG used in this work.

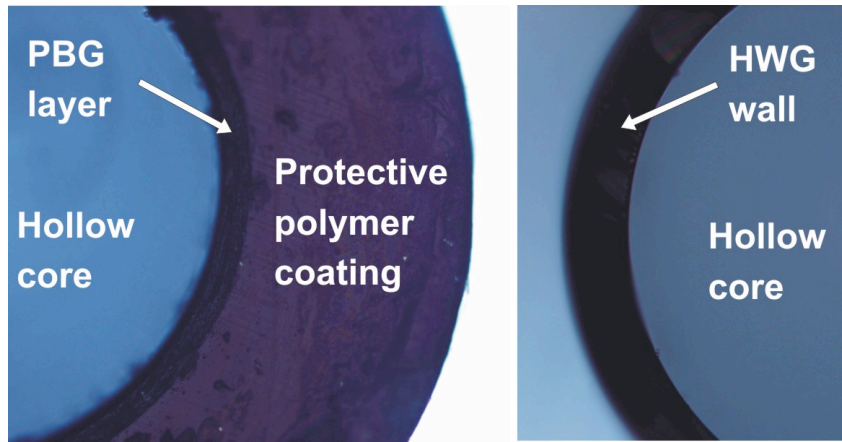


Figure 4-12: Microscope image of hollow waveguide cross sections with 10 X magnification of (left) OmniGuide fiber and (right) silica hollow waveguide.

The experimental setup for the OmniGuide fiber sensing system is shown in Figure 4-13.

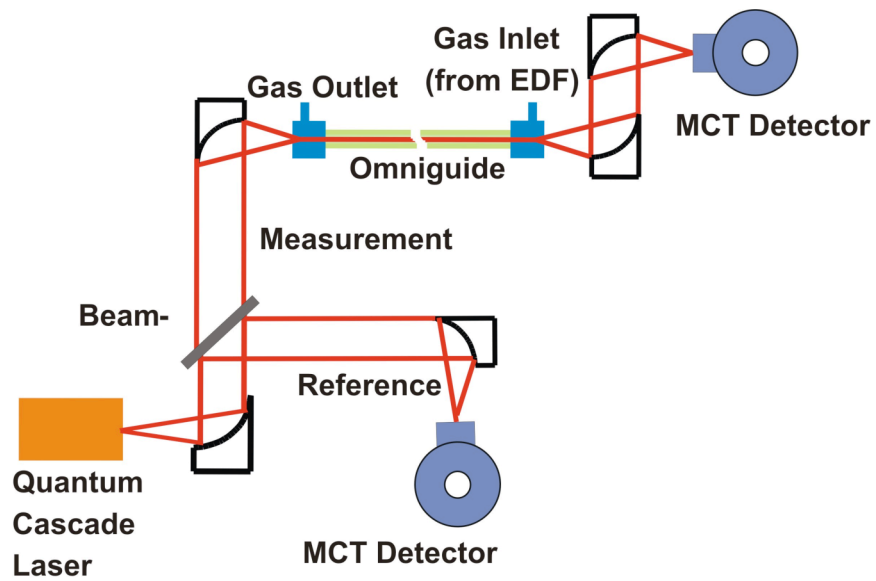


Figure 4-13: Experimental setup.

As in the case of the silica HWG, the OmniGuide fiber simultaneously acts as waveguide and miniaturized gas cell for continuous sensing inside the hollow fiber core. The laser beam was divided into a reference and measurement channel with both beam lines equipped with liquid nitrogen cooled MCT detectors (Kolmar Technologies, Newburyport, MA). While the silica HWG experiments utilized an oscilloscope to follow the signal from a single pulse of the QCL, data sets for the second generation system were recorded using a high speed data acquisition system (AMO, Aachen, Germany) enabling sampling at 100 MHz on each channel. This system allowed 10^6 pulses to be averaged, thereby significantly reducing the noise from pulse-to-pulse variations of the laser leading to an optimized signal-to-noise ratio. Each measurement of both the measurement and the reference channel required 8 s to average one million curves.

To avoid the substantial error bars due to manual sample preparation as evident in the measurements utilizing the silica HWG, gas samples for these experiments were prepared by exponential dilution, which is a technique commonly applied for trace gas calibration in gas chromatography⁷⁸. A known volume of ethyl chloride gas was injected into an exponential dilution flask⁷⁹, as shown in Figure 4-14.

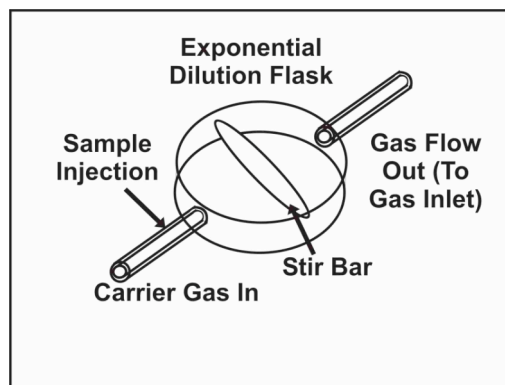


Figure 4-14: Schematic of an exponential dilution flask.

Ethyl chloride gas was then exponentially diluted by an inert carrier gas (air) flowing at a constant velocity of 39 mL/min through this chamber. Using exponential dilution, an entire calibration series is recorded with a single sample, thus minimizing the error resulting from the manual preparation of individually diluted samples. The concentration (C) of analyte diluted in the carrier gas and flowing through the PBG fiber gas cell can be calculated at any time (t) by:

$$C = C_0 e^{-\alpha t} \quad (\text{Eqn 4.3})$$

where (C_0) is the initial analyte concentration inside the exponential dilution chamber upon injection and (α) is the ratio of the carrier gas flow rate to the volume of the dilution chamber.

4.6.2 Results

The overlap between the emission frequency of the laser and the C-H absorption band of ethyl chloride gas results in absorption of radiation in the presence of analyte, which can be used for quantitative analysis based on the Beer-Lambert law. Injection of ethyl

chloride gas into the exponential dilution chamber generates a sensor response curve as shown in Figure 4-15.

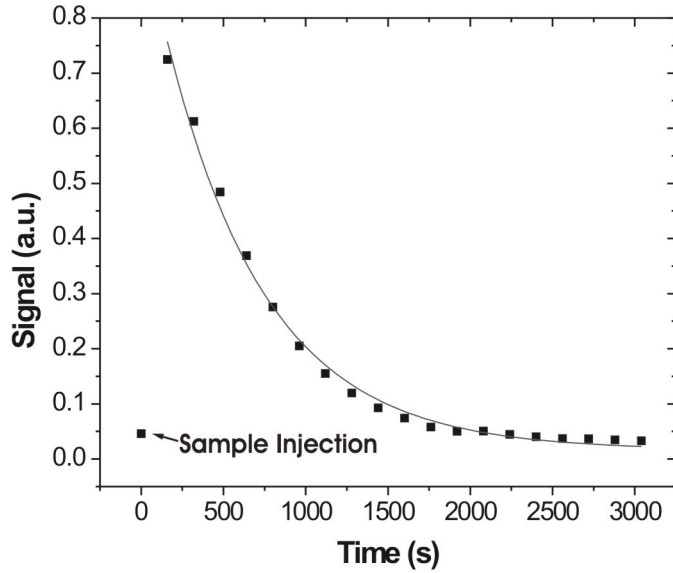


Figure 4-15: System response curve to an exponential dilution series.

The signal shown in Figure 4-15 is calculated by the ratio of the signals of the measurement channel and the reference channel subtracted from 1. Based on this analysis, in the absence of ethyl chloride gas, the two channels are approximately equal giving a ratio of 1 corresponding to a signal of 0. As gas is injected into the exponential dilution flask, the concentration inside the waveguide remains at zero generating no signal. Once gas flows into the waveguide, damping of the laser radiation occurs in the measurement channel generating a ratio < 1 . Hence, the corresponding signal increases, followed by an exponential decrease with dilution of the gas mixture.

The obtained data sets fit to a first order exponential decay curve, as predicted by exponential dilution theory, with a residual value of 0.998. The instantaneous concentration inside the photonic bandgap gas cell at any given time (t) can be calculated by Eqn 4.3. Concentration gradients inside the hollow core PBG fiber gas cell are neglected as the flow rate of 39 mL/min and the internal hollow waveguide volume of the fiber (1.5 mL) result in a sample residence time inside the hollow core of 2.3 s, which is faster than the data sampling rate of 8 s. Hence, we assume that any given data point represents an average concentration inside the waveguide for that 8 s interval.

During a dilution series measurement, the limit of detection is determined from the smallest detectable ethyl chloride concentration calculated using Eqn 4.3, which can be discriminated against the background noise following the 3σ criterion. The system noise derived by the random variations when analyte gas is not present is indicated in Figure 4-16 by the red line.

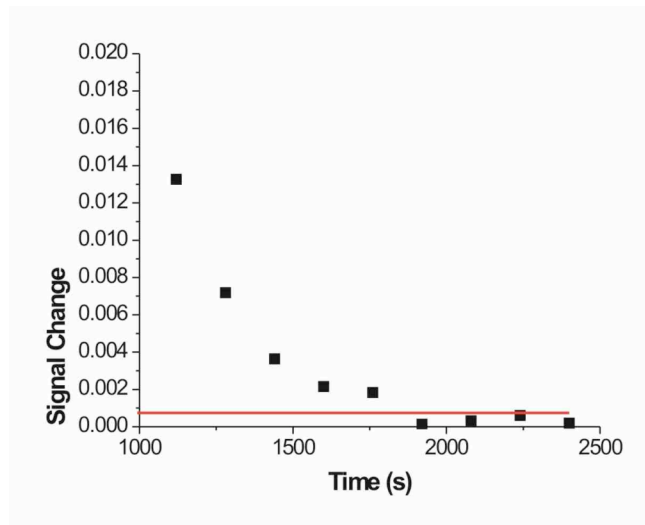


Figure 4-16: System noise level (red line) relative to signal change with time.

After 1750 s, the ethyl chloride concentration level has dropped below the level, which enables discriminating the signal change from noise indicating that the limit of detection is reached. The limit of detection for ethyl chloride gas inside the hollow photonic bandgap gas cell was determined to be 30 ± 40 ppb.

System improvements such as increased length of the PBG fiber and increased overlap between the laser and target analyte should enable limits of detection at the ppt concentration range. Furthermore, techniques such as analyte pre-concentration from the gas phase could drastically improve the sensitivity of the system. As the system utilizes a very small sample volume (1.5 mL) and is comparatively simple to operate, LODs at the ppt level would permit applications of this sensing concept in ultra-trace gas sensing and breath analysis.

4.7 Outlook

After successful demonstration of QCL gas sensing in both a silica and a photonic bandgap HWG, subsequent projects will involve improvements to the system aiming at enhanced sensitivity and further miniaturization, as discussed below.

4.7.1 Long Pathlength Coiled PBG HWG

As bending losses in the OmniGuide Fiber have been proven significantly lower than those in a conventional silica HWGs, setups including a coiled or folded waveguide can now be realized. According to the Lambert-Beer law, an increase in optical pathlength directly translates into increased sensitivity. The limit of detection for the demonstrated system with a pathlength of 1 m is 30 ppb. A waveguide length of 10 m would provide an improvement by one order of magnitude pushing the LOD into the single digit ppb range, which would be sufficient sensitivity for applications in breath analysis and atmospheric monitoring.

However, this increase in pathlength would require a system configuration including waveguide bends, as a 10 m long sensing system would be impractical. Bending losses in waveguides not only depend on the radius of curvature, but also on the length of the bend. It is therefore expected that the optimal configuration of a long waveguide would be a coiled geometry with the coil taking the shape of a square with rounded corners. Here, the bends would be discrete and occur only at the corners rather than over the entire length of the waveguide, therefore minimizing the expected losses. Characterization studies are essential in determining the bending radius and length resulting in minimal

losses, and the maximum waveguide length that can be used while maintaining sufficient signal throughput for trace measurements.

4.7.2 Miniaturization

Current setups have been demonstrated on a macro scale involving mL-sized samples of gas. While this is sufficient for applications such as breath analysis and atmospheric monitoring, other applications such as IR detection in miniaturized gas chromatography could be realized with further miniaturization and integration of IR gas sensing devices.

A potential format for a miniaturized gas sensor is to apply a small section of HWG as a gas cell with solid core fibers inserted into ends as optical coupling elements as shown in Figure 4-17. These fibers could then be pigtail-coupled to both laser and detector reducing the need for bulky optics allowing the entire setup to be mounted on a compact platform. Gas inlet and outlet ports would be created by drilling small bore holes (e.g. by focused ion beam milling) into the HWG section providing a flow through cell with an extremely small volume useful for micro gas sensing applications.

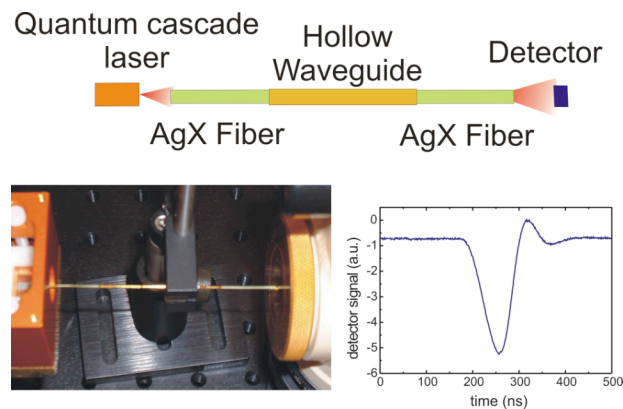


Figure 4-17: Fiber-HWG-Fiber coupling with system signal throughput.

The fiber-HWG-fiber system shown in Figure 4-17 has been tested for signal throughput and proved to be viable as light from the QCL is readily transmitted and the pulse shape of the laser pulse remains evident after coupling through the optical elements.

Miniature on-chip waveguides are another possible format for miniaturized gas sensing formats. As silica HWGs are fabricated by coating a metallic layer followed by a dielectric layer on the inside of a support tube, fabrication of these structures on-chip could be envisaged. Figure 4-18 shows first attempts at creating 500 μm wide by 500 μm deep metal coated channels on an epoxy resin substrate for testing of various bending and folding configurations of hollow waveguides.

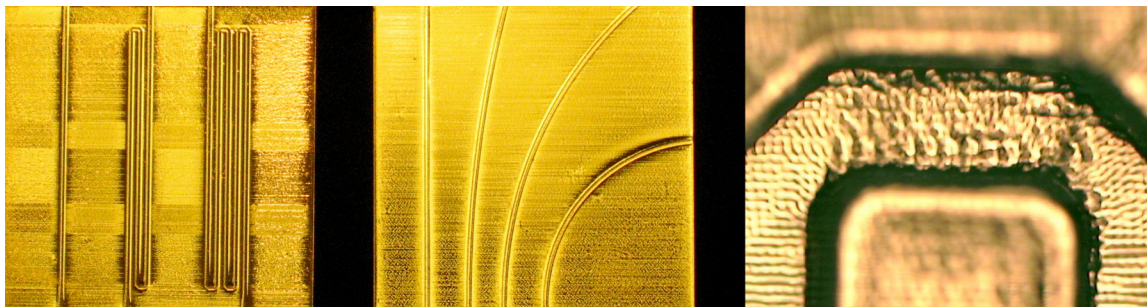


Figure 4-18: Gold coated microchannel waveguides 500 μm wide by 500 μm fabricated into epoxy resin block substrates for testing losses in folded (left) and curved (center) waveguides. (right) Channel roughness of these first prototypes.

Epoxy resin was selected due to the ease of defining and creating arbitrary patterns without the need for a mask and photolithographic processing. However, the surface roughness of the channels proved to be too high using this etching process as shown in Figure 4-18. A fabrication method such as focused ion beam milling could be used to

create the next generation of waveguides with much lower surface roughness, while still allowing arbitrary patterns to be created.

4.8 Conclusion

Trace gas sensing has been demonstrated by coupling QCLs to both conventional silica HWGs and newly developed PBG HWGs. A limit of detection of 0.5 ppm in the silica waveguide system is a significant advancement against previous works with QCLs coupled to HWGs by improving the detection scheme, data analysis, and increasing the HWG length.

In the PBG system, the limit of detection was further improved to a level of 30 ppb by using a photonic bandgap waveguide with improved transmission properties and by further refinement of the data acquisition strategy. This level of sensitivity is already in the range needed for selected target applications such as breath analysis, and can be further improved with a longer waveguide, which can be bent into a compact system due to the lower bending losses demonstrated for PBG hollow waveguides. With these improvements, limits of detection in the single ppb range or high ppt range will be possible providing sensitivities similar to or better than those of QCL gas analyzers currently emerging on the market. Furthermore, the developed gas sensing device concepts have the advantage of being more compact and using a much smaller gas sample volume than most commercial systems.

It is anticipated that the systems demonstrated in this work will lead to highly integrated and miniaturized IR gas sensing devices, which can provide the sensitivities needed for target applications in the fields of breath analysis and atmospheric monitoring.

REFERENCES

1. Miekisch, W.; Schubert Jochen, K.; Noeldge-Schomburg Gabriele, F. E., Diagnostic Potential of Breath Analysis--Focus on Volatile Organic Compounds. *Clinica chimica acta; international journal of clinical chemistry* **2004**, 347, (1-2), 25-39.
2. Kharitonov, S. A.; Barnes, P. J., Biomarkers of Some Pulmonary Diseases in Exhaled Breath. *Biomarkers* **2002**, 7, (1), 1-32.
3. Shnayderman, M.; Mansfield, B.; Yip, P.; Clark, H. a.; Krebs, M. D.; Cohen, S. J.; Zeskind, J. E.; Ryan, E. T.; Dorkin, H. L.; Callahan, M. V.; Stair, T. O.; Gelfand, J. A.; Gill, C. J.; Hitt, B.; Davis, C. E., Species-Specific Bacteria Identification Using Differential Mobility Spectrometry and Bioinformatics Pattern Recognition. *Analytical Chemistry* **2005**, 77, 5930-5937.
4. McGrath, L. T.; Patrick, R.; Silke, B., Breath Isoprene in Patients with Heart Failure. *European Journal of Heart Failure* **2001**, 3, 423-427.
5. Sehnert, S. S.; Jiang, L.; Burdick, J. F.; Risby, T. H., Breath Biomarkers for Detection of Human Liver Diseases: Preliminary Study. *Biomarkers* **2002**, 7, (2), 174-187.
6. CCSP <http://www.climate-science.gov/>
7. Holland, G. H.; Webster, P. J.; Curry, J. A., The Aerosonde Robotic Aircraft: A New Paradigm for Environmental Observations. *Bulletin of the American Meteorological Society* **2001**, 82, 889.
8. Sachse, G. W.; Hill, G. F.; Wade, L. O.; Perry, M. G., Fast-Response, High-Precision Carbon Monoxide Sensor Using a Tunable Diode Laser Absorption Technique. *Journal of Atmospheric Research* **1987**, 92, 2071.
9. Sachse, G. W.; Collins Jr., J. E.; Hill, G. F.; Wade, L. O.; Burney, L. G.; Ritter, J. A., Airborne Tunable Diode Laser Sensor for Highprecision Concentration and Flux Measurements of Carbon Monoxide and Methane. *Proc. SPIE International Symposium on Laser Spectroscopy* **1991**, 1433, (145).
10. Webster, C. R.; Sander, S. P.; Beer, R.; May, R. D.; Knollenberg, R. G.; Hunten, D. M.; Ballard, J., Tunable Diode Ir Spectrometer for in Situ Measurements of the Gas Phase Composition and Particle Size Distribution of Titan's Atmosphere. *Applied Optics* **1990**, 29, 907.
11. Scott, D. C.; Herman, R. H.; Webster, C. R.; May, R. D.; Flesch, G. J.; Moyer, E. J., Airborne Laser Infrared Absorption Spectrometer (Alias-Ii) for in Situ

- Atmospheric Measurements of N₂O, CH₄, CO, HCl, and NO₂ from Balloon or Remotely Piloted Aircraft Platforms. *Applied Optics* **1999**, 38, 4609.
12. Weinhold, F. G.; Fischer, H.; Hoor, P.; Wagner, V.; Königstedt, R.; Harris, G. W.; Anders, J.; Grisar, R.; Knothe, M.; Riedel, W. J.; Lubken, F.-J.; Schilling, T., Tristar. A Tracer in Situ TDLAS for Atmospheric Research. *Applied Physics B: Lasers and Optics* **1998**, 67, 411.
 13. Wert, B. P.; Fried, A.; Rauenbuehler, S.; Walega, J.; Henry, B., Design and Performance of a Tunable Diode Laser Absorption Spectrometer for Airborne Formaldehyde Measurements. *Journal of Geophysical Research* **2003**, 108, 4350.
 14. Herriott, D.; Kogelnik, H.; Kompfner, R., Off-Axis Paths in Spherical Mirror Interferometers. *Applied Optics* **1964**, 3, (4), 523-426.
 15. White, J. U., Long Optical Paths of Large Aperture. *Journal of the Optical Society of America* **1942**, 32, (285-291).
 16. Sigrist, M. W., Trace Gas Monitoring by Laser-Photoacoustic Spectroscopy. *Infrared Physics & Technology* **1995**, 36, (1), 415-425.
 17. O'Keefe, A.; Deacon, D. A. G., Cavity Ring-Down Optical Spectrometer for Absorption Measurements Using Pulsed Laser Sources. *Review of Scientific Instruments* **1988**, 59, (12), 2544-2551.
 18. O'Keefe, A., Integrated Cavity Output Analysis of Ultra-Weak Absorption. *Chemical Physics Letters* **1998**, 293, 331-336.
 19. Gimmetstad, G. G., *Differential-Absorption Lidar for Ozone and Industrial Emissions*. Springer GmbH: Berlin, 2005; Vol. 102, p 187-212.
 20. Gmachl, C.; Capasso, F.; Sivco, D. L.; Cho, A. Y., Recent Progress in Quantum Cascade Lasers and Applications. *Reports on Recent Progress in Physics* **2001**, 64, 1533-1601.
 21. Kosterev, A. A.; Tittel, F. K., Chemical Sensors Based on Quantum Cascade Lasers. *IEEE Journal of Quantum Electronics* **2002**, 38, 582-591.
 22. Hvozdar, L.; Gianordoli, S.; Strasser, G.; Schrenk, W.; Unterrainer, K.; Gornik, E.; Murthy, C. S. S. S.; Kraft, M.; Pustogow, V.; Mizaikoff, B., GaAs/AlGaAs Quantum Cascade Laser - a Source for Gas Absorption Spectroscopy. *Physica E: Low-Dimensional Systems & Nanostructures (Amsterdam)* **2000**, 7, (1&2), 37-39.
 23. Paldus, B. A.; Spence, T. G.; Zare, R. N.; Oomens, J.; Harren, F. J. M.; Parker, D. H.; Gmachl, C.; Capasso, F.; Sivco, D. L.; Baillargeon, J. N.; Hutchinson, A. L.;

- Cho, A. Y., Photoacoustic Spectroscopy Using Quantum-Cascade Lasers. *Optics Letters* **1999**, 24, (3), 178-180.
24. Hofstetter, D.; Beck, M.; Faist, J.; Ngele, M.; Sigrist, M. W., Photoacoustic Spectroscopy with Quantum Cascade Distributed-Feedback Lasers. *Optics Letters* **2001**, 26, (12), 887-889.
 25. Kosterev, A. A.; Bakhirkin, Y. A.; Tittel, F. K.; Blaser, S.; Bonetti, Y.; Hvozdar, L., Photoacoustic Phase Shift as a Chemically Selective Spectroscopic Parameter. *Applied Physics B: Lasers and Optics* **2004**, 78, (6), 673-676.
 26. Kosterev, A. A.; Bakhirkin, Y. A.; Tittel, F. K., Ultrasensitive Gas Detection by Quartz-Enhanced Photoacoustic Spectroscopy in the Fundamental Molecular Absorption Bands Region. *Applied Physics B: Lasers and Optics* **2004**, 80, (1), 133-138.
 27. Kosterev, A. A.; Malinovsky, A. L.; Tittel, F. K.; Gmachl, C.; Capasso, F.; Sivco, D. L.; Baillargeon, J. N.; Hutchinson, A. L.; Cho, A. Y., Cavity Ringdown Spectroscopic Detection of Nitric Oxide with a Continuous-Wave Quantum-Cascade Laser. *Applied Optics* **2001**, 40, (30), 5522-5529.
 28. Silva, M. L.; Sonnenfroh, D. M.; Rosen, D. I.; Allen, M. G.; O'Keefe, A., Integrated Cavity Output Spectroscopy Measurements of Nitric Oxide Levels in Breath with a Pulsed Room-Temperature Quantum Cascade Laser. *Applied Physics B: Lasers and Optics* **2005**, 81, (705-710).
 29. Bakhirkin, Y. A.; Kosterev, A. A.; Roller, C.; Curl, R. F.; Tittel, F. K., Mid-Infrared Quantum Cascade Laser Based Off-Axis Integrated Cavity Output Spectroscopy for Biogenic Nitric Oxide Detection. *Applied Optics* **2004**, 43, (11), 2257-2266.
 30. Kosterev, A. A.; Tittel, F. K.; Kohler, R.; Gmachl, C.; Capasso, F.; Sivco, D. L.; Cho, A. Y.; Wehe, S.; Allen, M. G., Thermoelectrically Cooled Quantum-Cascade-Laser-Based Sensor for the Continuous Monitoring of Ambient Atmospheric Carbon Monoxide. *Applied Optics* **2002**, 41, (6), 1169-1173.
 31. Shi, Q.; Nelson, D. D.; McManus, J. B.; Zahniser, M. S.; Parrish, M. E.; Baren, R. E.; Shafer, K. H.; Harward, C. N., Quantum Cascade Infrared Laser Spectroscopy for Real-Time Cigarette Smoke Analysis. *Analytical Chemistry* **2003**, 75, (19), 5180-5190.
 32. Menzel, L.; Kosterev, A. A.; Curl, R. F.; Tittel, F. K.; Gmachl, C.; Capasso, F.; Sivco, D. L.; Baillargeon, J. N.; Hutchinson, A. L.; Cho, A. Y.; Urban, W., Spectroscopic Detection of Biological NO with a Quantum Cascade Laser. *Applied Physics B: Lasers and Optics* **2001**, 72, (7), 859-863.

33. Ganser, H.; Urban, W.; Brown, J. M., The Sensitive Detection of No by Faraday Modulation Spectroscopy with a Quantum Cascade Laser. *Molecular Physics* **2003**, 101, (4-5), 545-550.
34. Nelson, D. D.; Shorter, J. H.; McManus, J. B.; Zahniser, M. S., Sub-Part-Per-Billion Detection of Nitric Oxide in Air Using a Thermoelectrically Cooled Mid-Infrared Quantum Cascade Laser Spectrometer. *Applied Physics B: Lasers and Optics* **2002**, 75, (2-3), 343-350.
35. Bakhirkin, Y. A.; Kosterev, A. A.; Roller, C.; Curl, R. F.; Tittel, F. K., Mid-Infrared Quantum Cascade Laser Based Off-Axis Integrated Cavity Output Spectroscopy for Biogenic Nitric Oxide Detection. *Applied Optics* **2004**, 43, (11), 2257-2266.
36. Fetzer, G. J.; Pittner, A. S.; Silkoff, P. E., Midinfrared Laser Absorption Spectroscopy in Coiled Hollow Optical Waveguides. *Proc. SPIE* **2003**, 4957, 124-133.
37. Weber, W. H.; Remillard, J. T.; Chase, R. E.; Richert, J. F.; Capasso, F.; Gmachl, C.; Hutchinson, A. L.; Sivco, D. L.; Baillargeon, J. N.; Cho, A. Y., Using a Wavelength-Modulated Quantum Cascade Laser to Measure No Concentrations in the Parts-Per-Billion Range for Vehicle Emissions Certification. *Applied Spectroscopy* **2002**, 56, 706-714.
38. Weidmann, D.; Kosterev, A. A.; Roller, C.; Curl, R. F.; Fraser, M. P.; Tittel, F. K., Monitoring of Ethylene by a Pulsed Quantum Cascade Laser. *Applied Optics* **2004**, 43, (16), 3329-3334.
39. Aerodyne Research, Inc. <http://www.aerodyne.com/>
40. Physical Sciences Inc. <http://www.psicorp.com/products/qcensors.shtml>
41. Cascade Technologies <http://www.cascade-technologies.com/site/GasSensingMarkets.php>
42. Harrington, J. A., A Review of Ir Transmitting, Hollow Waveguides. *Fiber and Integrated Optics* **2000**, 19, (3), 211-227.
43. Lendl, B.; Mizaikoff, B., *Optical Fibers for Mid-Infrared Spectrometry*. John Wiley and Sons Ltd.: New York, 2002; Vol. 2.
44. Sanghera, J. S.; Aggarwal, I. D., *Infrared Fiber Optics*. CRC Press: Boca Raton, FL, 1998.
45. Garmire, E.; McMahon, T.; Bass, M., Propagation of Infrared Light in Flexible Hollow Waveguides. *Applied Optics* **1976**, 15, (1), 145-150.

46. Miyagi, M.; Hongo, A.; Aizawa, Y.; Kawakami, S., Fabrication of Germanium-Coated Nickel Hollow Waveguides for Infrared Transmission. *Applied Physics Letters* **1983**, 43, (5), 430-2.
47. Matsuura, Y.; Miyagi, M.; Hongo, A., Loss Reduction of Dielectric-Coated Metallic Hollow Waveguides for Co₂ Laser Light Transmission. *Optics & Laser Technology* **1990**, 22, (2), 141-145.
48. Dahan, R.; Dror, J.; Croitoru, N., Characterization of Chemically Formed Silver Iodine Layers for Hollow Infrared Guides. *Materials Research Bulletin* **1992**, 27, (6), 761-766.
49. Abel, T.; Hirsch, J.; Harrington, J. A., Hollow Glass Waveguides for Broadband Infrared Transmission. *Optics Letters* **1994**, 19, (4), 1034-1036.
50. Fink, Y.; Winn, J. N.; Fan, S.; Chen, C.; Michel, J.; Joannopoulos, J. D.; Thomas, E. L., A Dielectric Omnidirectional Reflector. *Science (Washington, D. C.)* **1998**, 282, 1679-1682.
51. Cregan, R. F.; Mangan, B. J.; Knight, J. C.; Birks, T. A.; Russell, P. S. J.; Roberts, P. J.; Allan, D. C., Single-Mode Photonic Band Gap Guidance of Light in Air. *Science (Washington, D. C.)* **1999**, 285, 1537-1539.
52. Hart, S. D.; Maskaly, G. R.; Temelkuran, B.; Prideaux, P. H.; Joannopoulos, J. D.; Fink, Y., External Reflection from Omnidirectional Dielectric Mirror Fibers. *Science (Washington, DC, United States)* **2002**, 296, (5567), 510-513.
53. Temelkuran, B.; Hart, S. D.; Benoit, G.; Joannopoulos, J. D.; Fink, Y., Wavelength-Scalable Hollow Optical Fibers with Large Photonic Bandgaps for Co₂ Laser Transmission. *Nature (London, United Kingdom)* **2002**, 420, (6916), 650-653.
54. Katagiri, T.; Matsuura, Y.; Miyagi, M., Metal-Covered Photonic Bandgap Multilayer for Infrared Hollow Waveguides. *Applied Optics* **2002**, 41, (36), 7603-7606.
55. Barkou, S. E.; Broeng, J.; Bjarklev, A., Silica-Air Photonic Crystal Fiber Design That Permits Waveguiding by a True Photonic Bandgap Effect. *Optics Letters* **1999**, 24, (1), 46-48.
56. Laegsgaard, J.; Mortensen, N. A.; Riishede, J.; Bjarklev, A., Material Effects in Air-Guiding Photonic Bandgap Fibers. *Journal of the Optical Society of America B: Optical Physics* **2003**, 20, (10), 2046-2051.

57. Knight, J. C., Photonic Crystal Fibers. *Nature (London, United Kingdom)* **2003**, 424, 846-851.
58. Marcatili, E. A. J.; Schmeltzer, R. A., Hollow Metallic and Dielectric Waveguides for Long Distance Optical Transmission Ona Lasers. *Bell Systems Technical Journal* **1964**, 43, 1783-1809.
59. Miyagi, M.; Harada, K.; Kawakami, S., Wave Propagation and Atteuation in the General Class of Circular Waveguides with Uniform Curvature. *IEEE Transactions on Microwave Theory and Techniques* **1984**, 32, 513-521.
60. Miyagi, M.; Kawakami, S., Design Theory of Dielectric-Coated Circular Metallic Waveguides for Infrared Transmission. *Journal of Lightwave Technology* **1984**, 2, 116-126.
61. Charlton, C. M.; Thompson, B. T.; Mizaikoff, B., Hollow Waveguide Infrared Spectroscopy and Sensing. In *Springer Series on Chemical Sensing and Biosensing*, Springer-Verlag: Berlín, 2005.
62. Azarraga, L. V., Gold Coating of Glass Tubes for Gas Chromatography/Fourier Transform Infrared Spectroscopy "Light-Pipe" Gas Cells. *Applied Spectroscopy* **1980**, 34, (2), 224-225.
63. Yang, P. W. J.; Ethridge, E. L.; Lane, J. L.; Griffiths, P. R., Optimization of Gc/Ft-Ir Measurements I: Construction of Light-Pipes. *Applied Spectroscopy* **1984**, 38, (6), 813-816.
64. Saggese, S. J.; Harrington, J. A.; Sigel, J., George H., Attenuation of Incoherent Infrared Radiation in Hollow Sapphire and Silica Waveguides. *Optics Letters* **1991**, 16, (1), 27-29.
65. Saito, Y.; Kanaya, T.; Nomura, A.; Kano, T., Experimental Trial of a Hollow-Core Waveguide Used as an Absorption Cell for Concentration Measurment of Nh3 Gas with a Co2 Laser. *Optics Letters* **1993**, 18, (24), 2150-2152.
66. Yang, J.; Her, J.-W., Development of a Hollow Waveguide Sampler for Detection of Chlorinated Aromatic Compounds in Soils. *Anal. Chem.* **2000**, 72, 878-884.
67. Yang, J.; Tsui, C.-P., Detection of Chlorinated Aromatic Amines in Aqueous Solutions Based on an Infrared Hollow Waveguide Sampler. *Analytica Chimica Acta* **2001**, 442, 267-275.
68. Yang, J.; Her, J.-W.; Chen, S.-H., Development of an Infrared Hollow Waveguide as a Sensing Device for Detection of Organic Compounds in Aqueos Solutions. *Analytical Chemistry* **1999**, 71, 3740-3746.

69. De Melas, F.; Pustogow, V. V.; Wolcott, D. K.; Olson, D. C.; Inberg, A.; Croitoru, N.; Mizaikoff, B., Combination of a Mid-Infrared Hollow Waveguide Gas Sensor with a Supported Capillary Membrane Sampler for the Detection of Organic Compounds in Water. *International Journal of Environmental Analytical Chemistry* **2003**, 83, (7-8), 573-583.
70. Worrell, C. A.; Giles, I. P.; Adatia, N. A., Remote Gas Sensing with Mid-Infra-Red Hollow Waveguides. *Electronics Letters* **1992**, 28, (7), 615-617.
71. Worrell, C. A.; Gallen, N. A., Trace-Level Detection of Gases and Vapours with Mid-Infra-Red Hollow Waveguides. *Journal of Physics D: Applied Physics* **1997**, 30, 1984-1995.
72. Hvozdar, L.; Gianordoli, S.; Strasser, G.; Schrenk, W.; Unterrainer, K.; Gornik, E.; Murthy, C. S. S. S.; Kraft, M.; Pustogow, V.; Mizaikoff, B.; Inberg, A.; Croitoru, N., Spectroscopy in the Gas Phase with Gaas/Algaas Quantum-Cascade Lasers. *Applied Optics* **2000**, 39, (36), 6926-6930.
73. Fetzer, G. J.; Pittner, A. S.; Ryder, W. L.; Brown, D. A., Tunable Diode Laser Absorption Spectroscopy in Coiled Hollow Optical Waveguides. *Applied Optics* **2002**, 41, (18), 3613-3621.
74. Charlton, C.; De Melas, F.; Inberg, A.; Croitoru, N.; Mizaikoff, B., Hollow-Waveguide Gas Sensing with Room-Temperature Quantum Cascade Lasers. *IEE Proceedings - Optoelectronics* **2003**, 150, (4), 306-309.
75. Charlton, C.; Temelkuran, B.; Dellemann, G.; Mizaikoff, B., Midinfrared Sensors Meet Nanotechnology: Trace Gas Sensing with Quantum Cascade Lasers inside Photonic Band-Gap Hollow Waveguides. *Applied Physics Letters* **2005**, 86, (194102-194104).
76. Croitoru, N.; Dror, J.; Goldenberg, E.; Mendelovic, D.; Ganot, I. Hollow Fiber Waveguide and Method of Making Same. 1990.
77. Dror, J.; Inberg, A.; Elboim, A.; Dahan, R.; Croitoru, N., New Performances Andn Applications of Fused Silica and Plastic Waveguides. *Proc. SPIE* **1995**, 2396, 106-114.
78. Lovelock, J. E., Ionization Methods for the Analysis of Gases and Vapors. *Anal. Chem.* **1961**, 33, 162-78.
79. Nozoye, H., Exponential Dilution Flask. *Analytical Chemistry* **1978**, 50, (12), 1727.

CHAPTER 5

PLANAR IR WAVEGUIDE DESIGN

This chapter presents considerations on the design of planar mono-mode MIR waveguides, which will maximize the sensitivity of evanescent wave measurements in the mid-infrared spectral regime.

5.1 Beam Propagation Simulations

As discussed in Chapter 3, the fractional power of radiation guided outside the core, or evanescent field intensity, is known to increase as the waveguide thickness decreases. This work presents the use of beam propagation methods (BPM) for the simulation of optical waveguides determining an optimum waveguide thickness for QCL sensing applications.

5.1.1 BPM Method Setup

Beam propagation methods (BPM) enable the simulation of propagation of light through waveguide structures based on mode optics calculations. Simulations were performed using the Olympios software by C2V (Enschede, Netherlands).

BPM simulations were designed to calculate the mode profile for a free-standing waveguide with an analyte layer at the waveguide surface utilizing the refractive index profile shown in Figure 5-1.

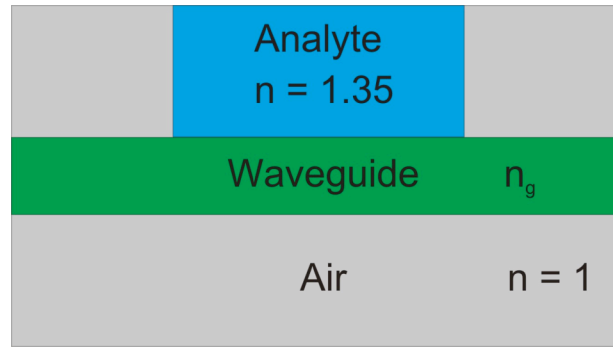


Figure 5-1: Refractive index profile for BPM simulations.

The setup shown in Figure 5-1 is treated as an infinite slab assuming that the profile into the plane is considered to be homogenous and infinite resulting in no radiation confinement in this direction. The free-standing waveguide was considered to be surrounded by air with a refractive index of 1, while the analyte layer was assigned a refractive index of 1.35, which is approximating the refractive index of an arbitrary analyte solution.

The radiation source is coupled into the waveguide at the left side of Figure 5-1, and has a Gaussian profile. To avoid coupling losses, the source is located inside the waveguide material in the simulation, and changes in size with the waveguide dimensions to completely fill the waveguide. In order to simulate the output of a QCL used in the experimental studies of this thesis, the source was defined to emit TM modes at a wavelength of 10 μm unless otherwise specified.

This profile provided a reasonable approximation of the evanescent field sensing system being utilized for measurements with a QCL coupled to a planar silver halide waveguide, which will be experimentally presented in Chapter 6.

As the waveguide thickness is varied, a visual inspection of the two-dimensional radiation intensity profile enables evaluating the ability of the waveguide to support a single or multiple modes. As an example, Figure 5-2 shows a waveguide with insufficient thickness to support even a single mode.

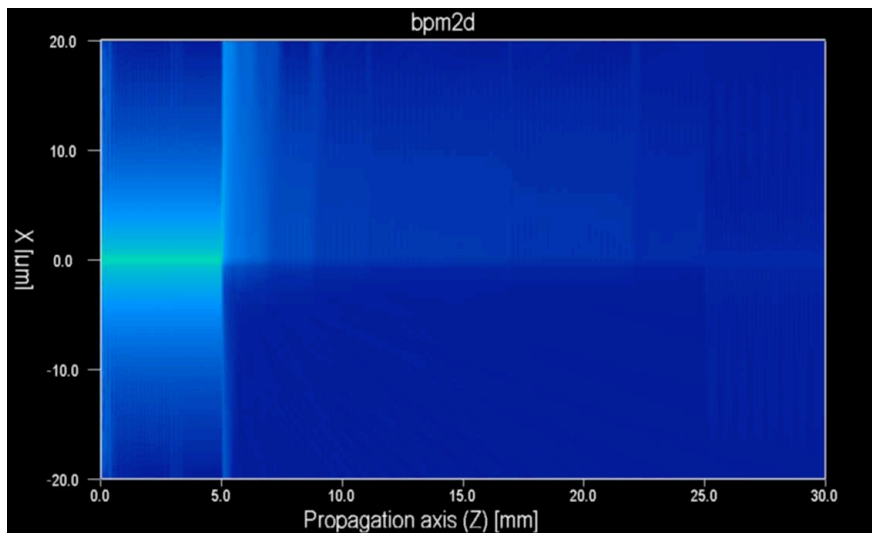


Figure 5-2: Waveguide with a thickness, which does not support any mode.

Light is coupled into the waveguide in Figure 5-2 and is able to propagate until it reaches the edge of the analyte deposition layer. Here, the refractive index of the surrounding material increases from 1 to 1.35 resulting in less contrast between the index of the waveguide and its surroundings leading to less mode confinement. Light is refracted from the waveguide at this point and lost into the surrounding matrix.

The waveguide shown in Figure 5-3 is capable of supporting only a single mode, which propagates to the end of the waveguide.

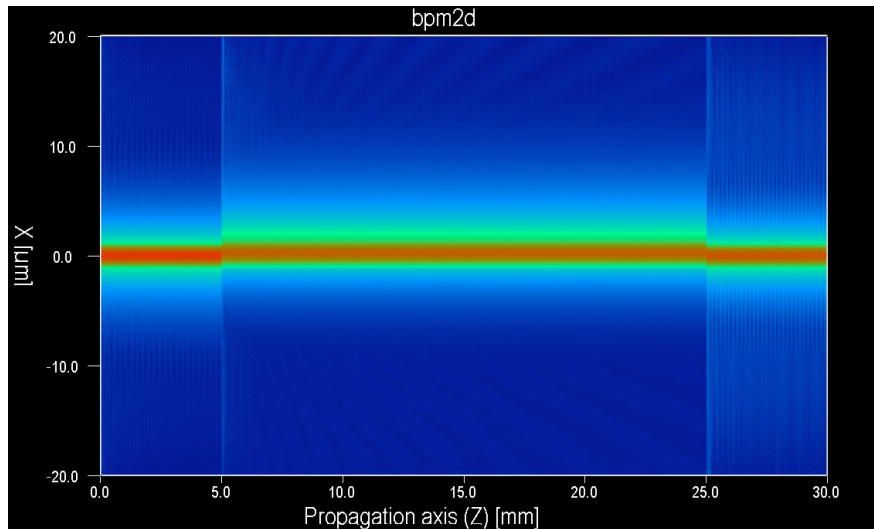


Figure 5-3: Waveguide with a thickness supporting a single mode.

The single mode character of the waveguide shown in Figure 5-3 is evident from the high radiation intensity at the waveguide core decreasing to the edges of the waveguide in a Gaussian fashion. The center of the waveguide shows a consistent high intensity without interference pattern, which would indicate the presence of additional modes.

As in the case of the thin waveguide shown in Figure 5-2, the single mode waveguide exhibits losses at the onset of the analyte layer. Again, this is due to a higher refractive index of the deposited layer, which is closer to that of the waveguide leading to less confinement of the mode. In the case of the slightly thicker waveguide shown in Figure

5-3, light is only partially lost at this interface with most of the radiation continuing to propagate through the waveguide.

The simulated analyte layer with a higher refractive index is also characterized by an increased evanescent field intensity, which would be beneficial in sensing applications due to an increased interaction between the analyte and the radiation confined in the waveguide.

Figure 5-4 shows a waveguide thick enough to support multiple modes as evident by an interference pattern.

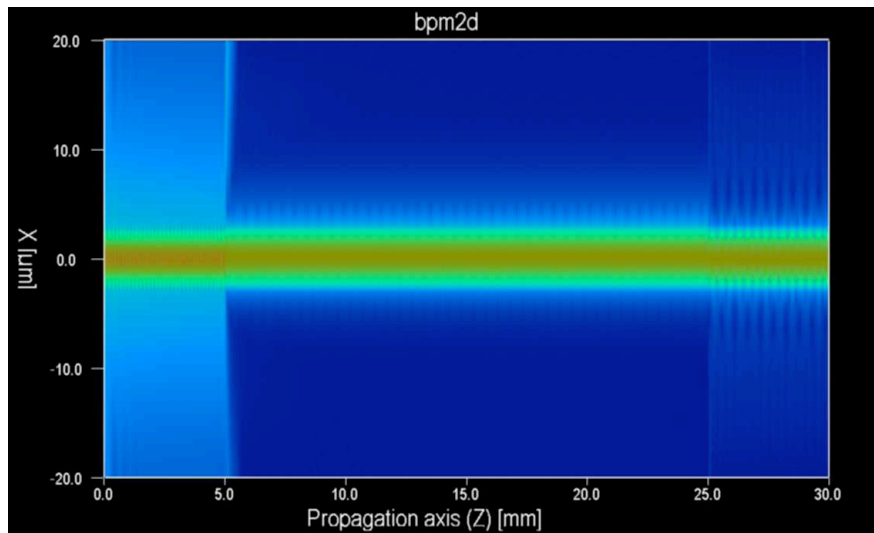


Figure 5-4: Waveguide with a thickness supporting multiple modes.

The intensity of the evanescent field was calculated by integrating the intensity outside the waveguide core across the analyte deposition area. In order to avoid considering

stray light for this integration, the intensity in area 2 shown in Figure 5-5 was subtracted from area 1.

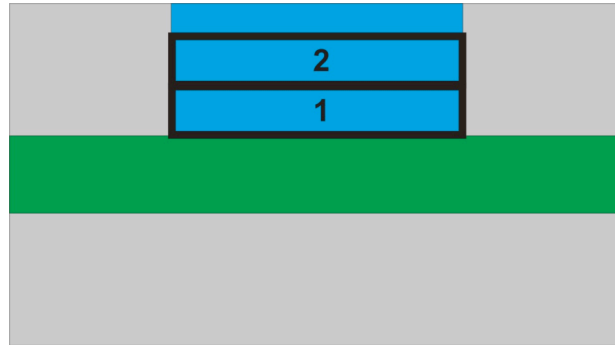


Figure 5-5: Integration regions for evanescent field intensity calculation of planar waveguides.

In Figure 5-5, area 1 stretches from the waveguide surface to a distance three times the evanescent field penetration depth. Area 2 stretches from three times to six times the penetration depth. Integrations were performed using a Matlab program shown in Appendix A.

5.1.2 BPM Results

Using the integration methods described above, system parameters such as waveguide thickness, waveguide refractive index, in-coupling angle, and wavelength of light were investigated to determine their effects on the evanescent field intensity.

The waveguide thickness producing maximum evanescent field intensity was investigated first, as shown in Figure 5-6 for a waveguide with a refractive index of 2.1.

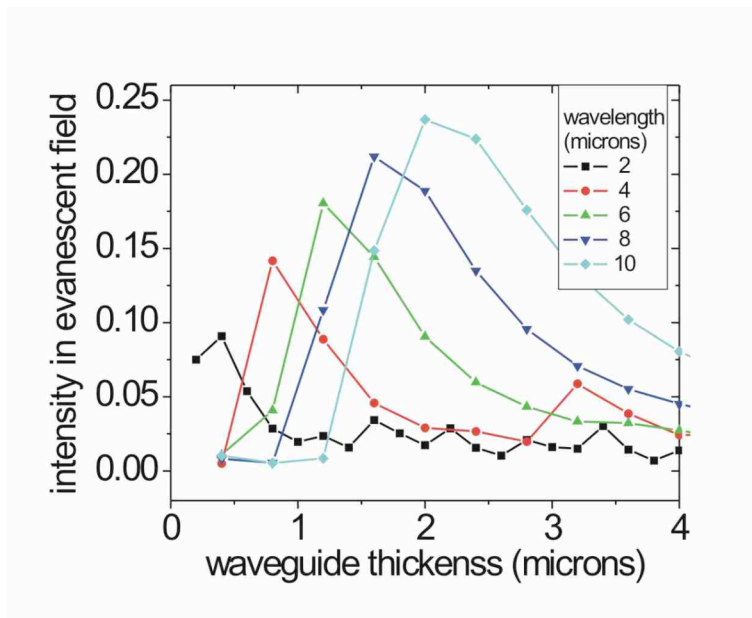


Figure 5-6: Evanescent field intensity as a function of waveguide thickness for various wavelengths of light.

As expected, the optimum thickness for maximum evanescent field intensity was found to increase linearly with increasing wavelength of light, as shown in Figure 5-7.

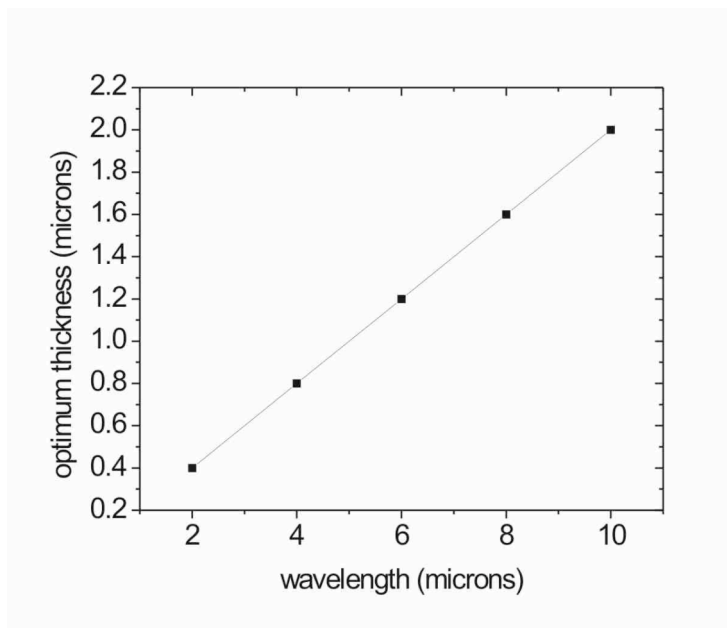


Figure 5-7: Dependence of the optimum waveguide thickness on the wavelength of light.

As the wavelength of light is increased, we also observe an increase of the intensity in the evanescent field for an ideal waveguide, as shown in Figure 5-8.

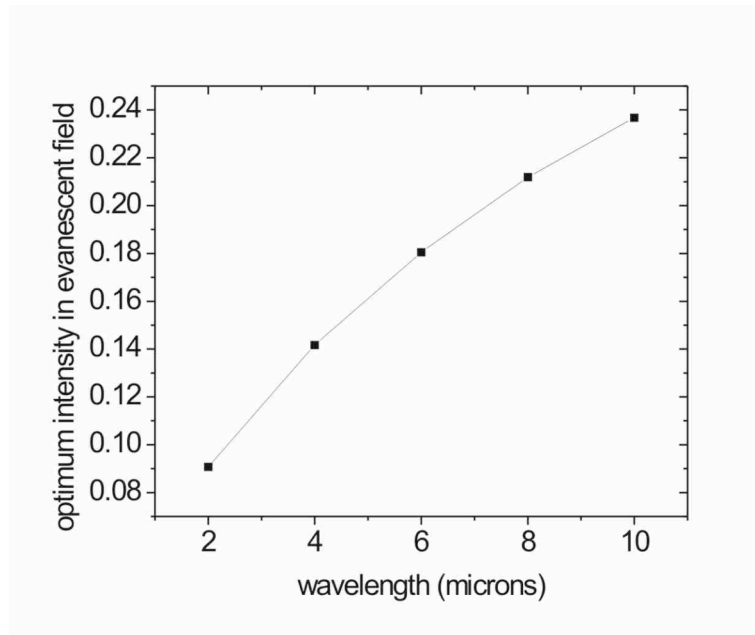


Figure 5-8: Maximum evanescent field intensity dependence on the wavelength of light.

The increase shown in Figure 5-8 is predicted by Eqn 3.3, which defines the penetration depth of the evanescent field. As the wavelength of light increases, the depth of penetration also increases implying that more energy should be guided outside the waveguide core within the leaky mode.

The effect of the in-coupling angle (θ) on the intensity in the evanescent field was investigated by changing the source tilt in the BPM setup using the scheme shown in Figure 5-9.

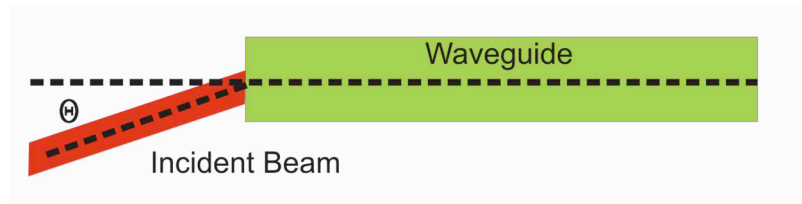


Figure 5-9: In-coupling angle.

The intensity in the evanescent field is shown in a 3-D plot as a function of both waveguide thickness and source tilt in Figure 5 -10.

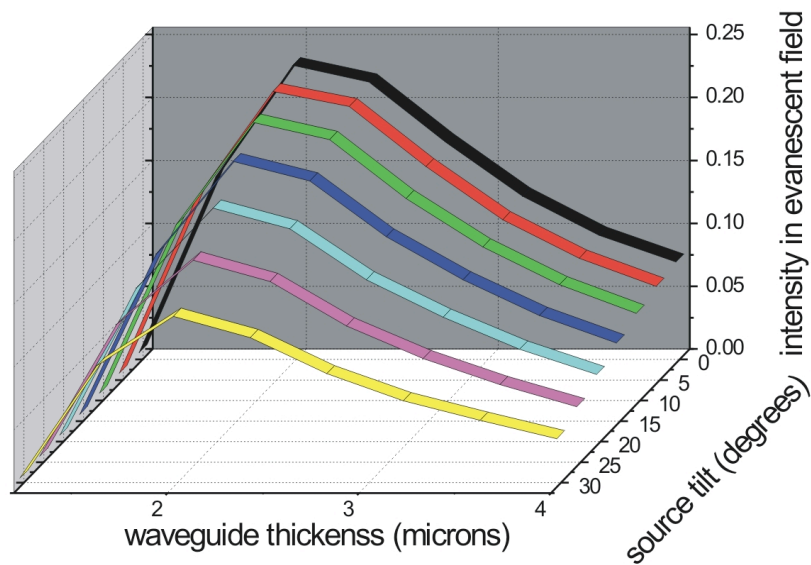


Figure 5-10: 3-D plot of intensity in the evanescent field as a function of waveguide thickness and source tilt.

The intensity in the evanescent field as a function of waveguide thickness is shown at various source tilt angles in Figure 5-11. These calculations were made considering a wavelength of 10 μm and a waveguide refractive index of 2.1.

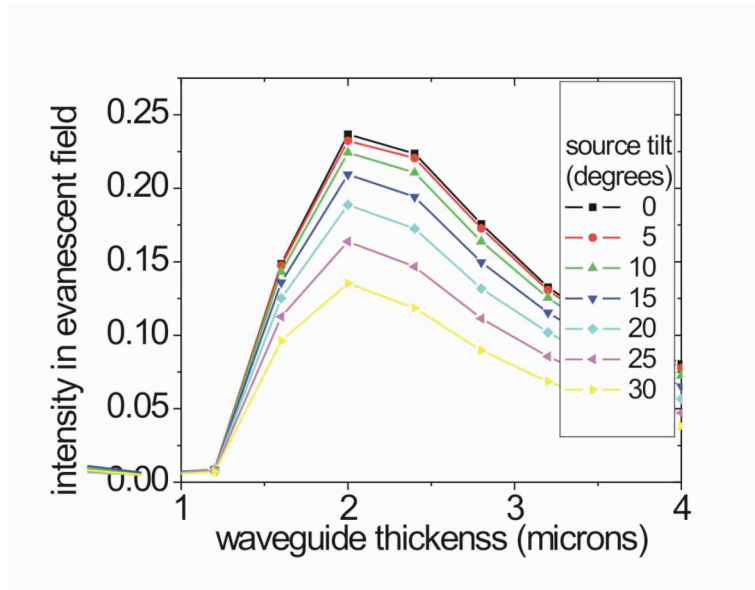


Figure 5-11: Intensity in the evanescent field as a function of the waveguide thickness for various source tilt angles.

From Figure 5-11, it is evident that the source tilt does not have an effect on the waveguide thickness providing maximum evanescent field intensity. For thin-film single mode waveguides calculated here, an increase in source tilt simply decreases the intensity in the evanescent field as shown in Figure 5-12.

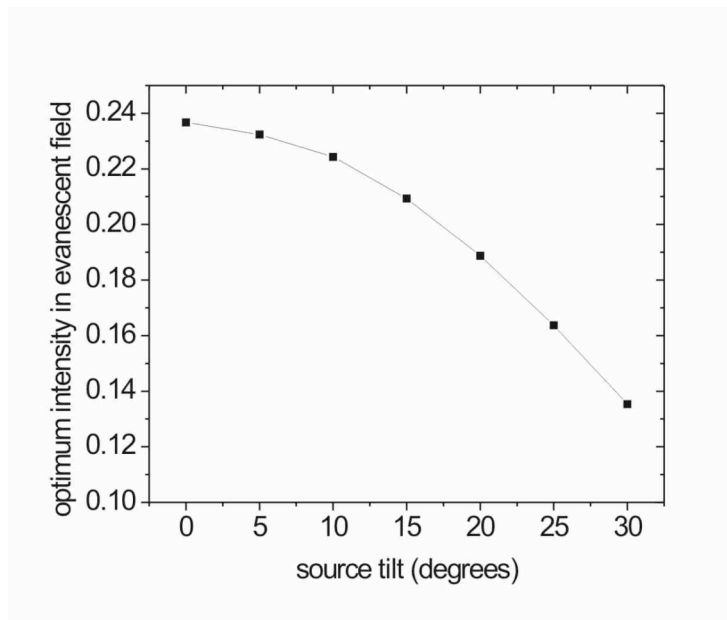


Figure 5-12: Maximum evanescent intensity dependence on source tilt angle

The decrease in evanescent field intensity with increasing source tilt shown in Figure 5-12 is expected, as the waveguide is unable to support high order modes, which would be excited by an increased in-coupling angle. Therefore, an increase in source tilt leads to a loss of radiation in the waveguide resulting in an overall decrease of evanescent field intensity.

The final parameter investigated was the effect of the waveguide refractive index on the waveguide thickness providing a maximized evanescent field intensity. The corresponding simulations are shown in Figure 5-13.

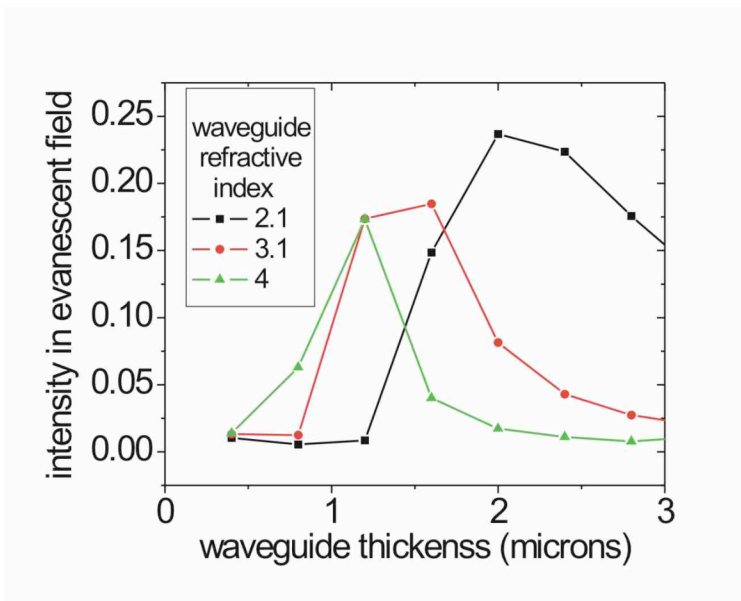


Figure 5-13: Optimum waveguide thickness by refractive index.

An increase in the refractive index of the waveguide leads to a decrease in the waveguide thickness, providing maximum evanescent field intensity as shown in Figure 5-14.

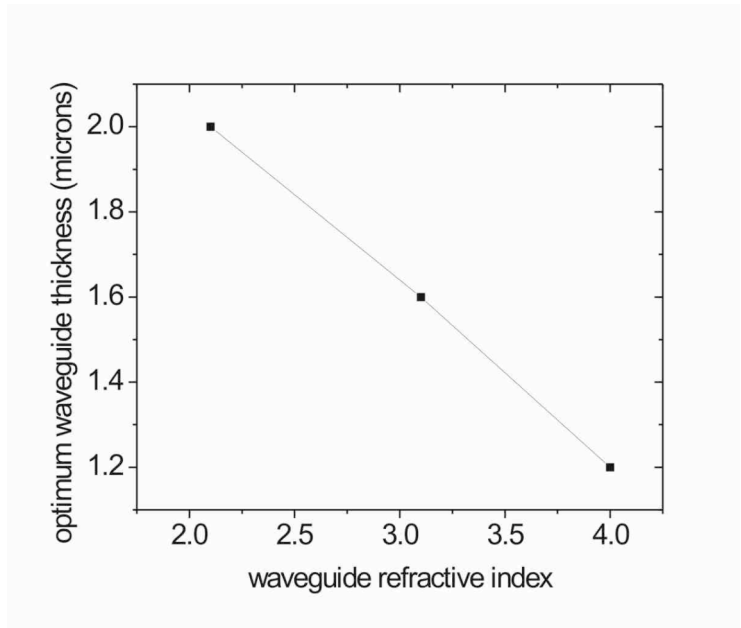


Figure 5-14: Dependence of the optimum waveguide thickness on the waveguide refractive index.

The trend shown in Figure 5-14 is expected due to waveguide confinement considerations. As the refractive index of the waveguide increases, there is an increase in the contrast between the waveguide and the surrounding material. This leads to an improved confinement of light inside the waveguide and allows radiation to be guided in a thinner waveguide. As a result, the waveguide forcing the highest intensity into the evanescent field is thinner.

A trend of decreasing evanescent field intensity in an optimized waveguide with increasing waveguide refractive index is also evident, and is shown in Figure 5-15.

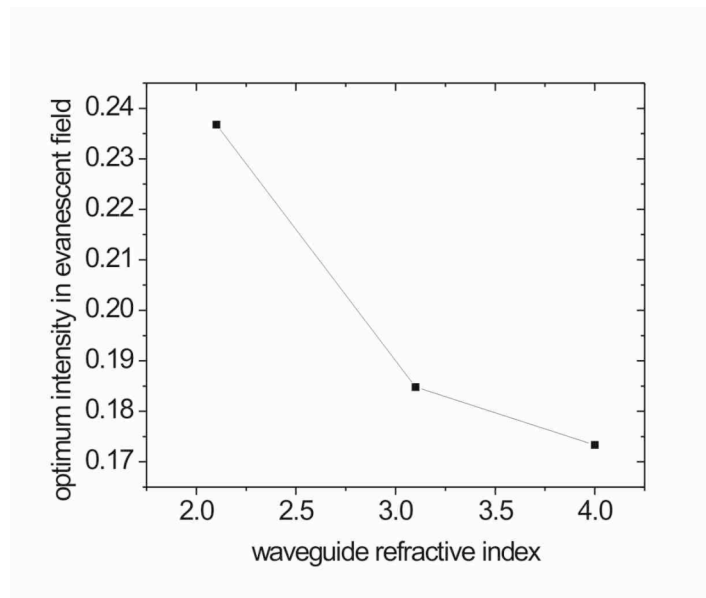


Figure 5-15: Dependence of the maximum evanescent field intensity on the waveguide refractive index.

The decrease shown in Figure 5-15 is predicted by Eqn 3.3, defining the penetration depth of the evanescent field. As the refractive index contrast of the waveguide and the

surrounding media increases (i.e. $n_1 - n_2$ increases), the depth of penetration decreases implying that the intensity of energy guided outside the waveguide core also decreases.

5.1.3 Optimizing the Signal-to-Noise Ratio

Optimization for evanescent field chemical sensing must take into account both the intensity in the evanescent field and the total amount of power transmitted through the waveguide, which would be detected at the distal end of the waveguiding structure.

As the power transmitted through a fiber decreases with decreasing diameter, optimization becomes a compromise between maximizing the fractional power in the evanescent field, and maximizing the total power received by the detector after radiation exits the fiber. This will provide an optimized signal-to-noise ratio and, therefore, optimized sensitivity for evanescent field sensing.

5.2 Silver Halide Planar Waveguides

Silver halide (AgX) fibers have a refractive index of 2.1. The calculations above show that a waveguide thickness of 2 μm would produce a maximized evanescent field intensity for a waveguide of this refractive index using radiation of 10 μm .

Cylindrical AgX fibers have been press tapered (as discussed in Chapter 6) from a circular diameter of 700 μm down to planar segments with a thickness of 100 μm . Free-standing waveguides thinner than 100 μm are very delicate to fabricate and utilize in chemical sensing applications, due to insufficient structural rigidity and mechanical stability. Planar waveguide segments with a thickness of 300 and 190 μm have successfully been used for evanescent field sensing, as discussed in Chapter 6 of this thesis.

The limitations of AgX materials have finally led to the development of novel thin-film waveguides, which have achieved single-mode confinement of radiation at 10.3 μm .

5.3 GaAs Planar Waveguides

To achieve single-mode MIR waveguides, thin-film GaAs layers were grown on an AlGaAs layer at a GaAs wafer substrate. Some structures included a Si₃N₄ layer on top of the GaAs waveguide as a surface protection. Fabrication details are discussed in Chapter 6.

The waveguide structure, refractive index profile, and mode intensity for the thin film GaAs waveguides as calculated by the collaborator on this development, Dr. Jerome Faist (University of Neuchatel, Switzerland) is depicted in Figure 5-16.

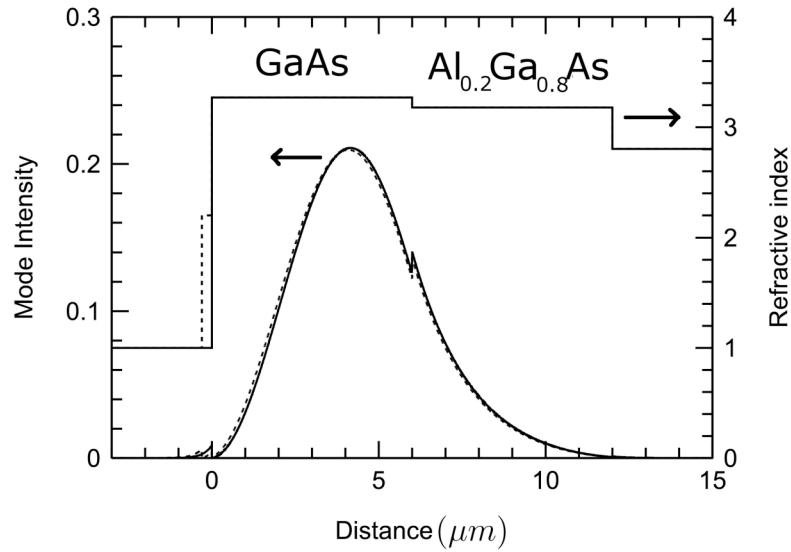


Figure 5-16: Calculated mode profile for GaAs thin film waveguides.

The computed fraction of light in the evanescent field interacting with an air layer of refractive index $n = 1$ is found to be 2.3×10^{-3} in this calculation. This value decreases to 1.6×10^{-3} with the additional Si₃N₄ overlayer. An increased evanescent field intensity could be

achieved for more tightly confined (thinner) waveguides, however, at the cost of a larger numerical aperture for the mode. In this waveguide structure, the calculated absorption is only 0.27 cm^{-1} . This absorption value is limited by leakage of the mode inside the n+ (Si) doped substrate. This low value of losses provided by this new generation of MIR waveguides enables the application of single-mode planar waveguides in sensing applications with a physical length of several centimeters at yet acceptable losses.

An experimental demonstration of thin-film single-mode GaAs waveguides for evanescent field chemical sensing applications is presented in Chapter 6.

5.4 Conclusion

The simulations presented above have shown that very thin waveguides (on the order of 2 μm for 10 μm light for a waveguide refractive index of 2.1) are needed to maximize the intensity of radiation guided in the evanescent field. Theoretical considerations based on beam propagation simulations have shown that the optimum waveguide thickness increases with increasing wavelength, and decreases with increasing refractive index of the waveguide, as predicted from theory.

As silver halide fibers cannot be fabricated at the required thicknesses ($< 10 \mu\text{m}$), a new generation of MIR waveguides has been devised based on epitaxially deposited thin-film GaAs, which provide substantially improved sensitivity for QCL based evanescent field absorption measurements. Sensing applications of this next-generation waveguide will be discussed in Chapter 6.

5.5 Outlook – Waveguide Coupling

The simulation results and loss calculations described above neglect losses due to radiation coupling into the waveguide structure. However, coupling losses becoming increasingly significant with decreasing waveguide thickness, and are of substantial concern for the thin-film waveguides discussed above. The investigation of strategies for fabricating grating couplers at the waveguide surface has led to a potential solution to circumnavigate this problem.

5.5.1 Theory on Blazed Angle Gratings

Blazed angle gratings use a diffraction grating with a sawtooth profile as shown in Figure 5-17 preferentially coupling into one order.

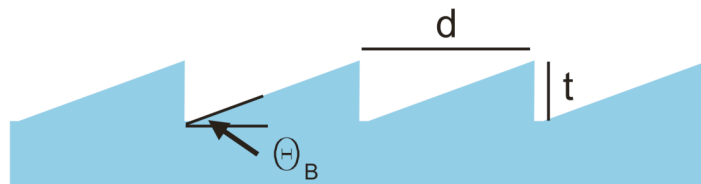


Figure 5-17: Blazed angle grating profile.

The gratings are governed by the relationship:

$$m\lambda = 2d \cdot \sin\theta_B \quad \text{Eqn 5.1}$$

where m is the diffraction order, λ is the wavelength of incident light, d is the grating period, and θ_B is the blaze angle as shown in Figure 5-17.

5.5.2 Hot Embossed Silver Halide Gratings

Gratings have been incorporated into planar AgX fibers (discussed in Chapter 6) by hot embossing. Silver halide fibers become malleable at a temperature of approximately 170 °C allowing a grating to be stamped into the surface of the material from e.g. a glass master.

A 30 mm by 30 mm master grating was purchased from O/E Land Inc. (Saint-Laurent, QC, Canada) with a period of 7 μm and a blaze angle of 52.7° designed to diffract light at 10.6 μm into the first order. As the grating was fabricated as a replica of a master ruled grating, it consists of an epoxy layer coated with a reflective aluminum film. In order to avoid damage to the soft epoxy layer during the hot embossing process, a replica of the grating was cast into a soft sol-gel material, which was then hardened by curing. This sol-gel replica was used as the master for the grating pattern transfer to the surface of the AgX fiber via hot embossing.

The results of the pattern transfer are shown in the optical profiler (Veeco, Woodbury, New York) image of the AgX planar waveguide (thickness 100 μm) surface in Figure 5-18.

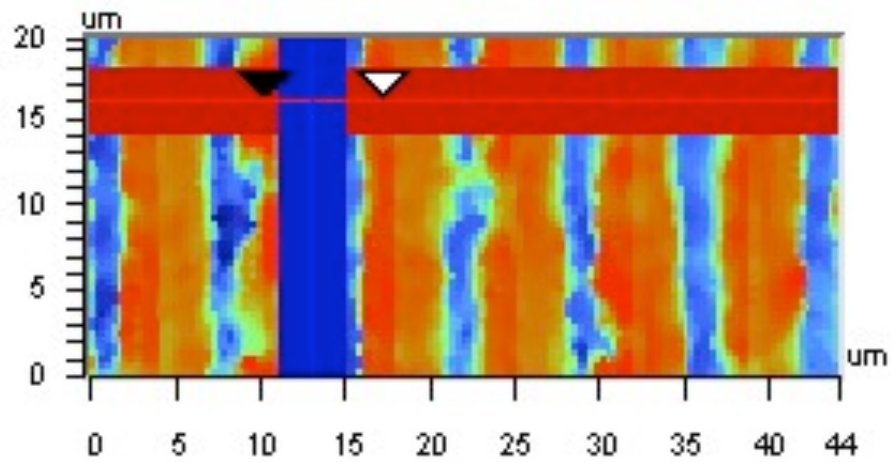


Figure 5-18: Optical profile of grating at AgX waveguide surface.

The image in Figure 5-18 shows a top view of the waveguide surface where pattern transfer occurred. We see high ridges in red decreasing towards the lowest points shown in blue. It is evident that pattern transfer has occurred and the fiber has a periodic pattern in the x-direction after embossing with no pattern in the y-direction. The period in the x-direction was then determined by the profile as shown in Figure 5-19.

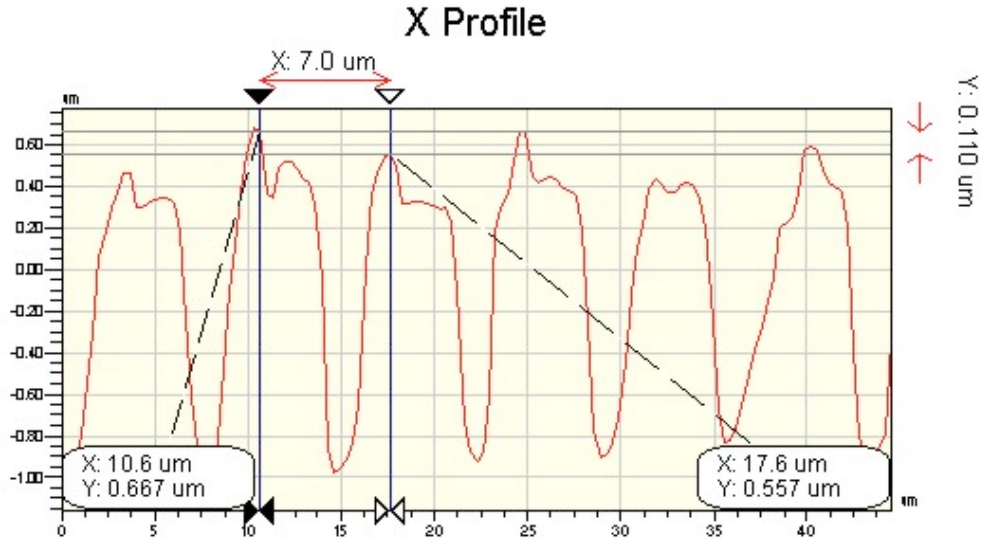


Figure 5-19: X-direction period profile of grating at the AgX fiber surface.

The determined period of 7 μm shown in Figure 5-19 matches that of the master grating used to fabricate the sol-gel embossing elements.

Currently, planar AgX waveguides with hot embossed blazed angle grating couplers are being tested for light coupling efficiency with a QCL emitting at 10.3 μm .

5.5.3 FIB Milled GaAs Gratings

The establishment of focused ion beam (FIB) technology at the FIB² Center at Georgia Tech has enabled milling arbitrary patterns into the waveguide surface.

For fabrication of grating couplers at the surface of GaAs waveguides by FIB milling, a grating was designed based on Eqn 5.1, which couples light at 10.3 μm into the first order ($m = 1$) using a blaze angle of 20 $^\circ$, a period of 5.5 μm , and a depth of 2 μm .

Figure 5-20 shows the generated bitmap file used as an input to the FIB control system to define the pattern for milling.



Figure 5-20: Bitmap pattern for FIB milling of blazed angle grating.

Given an input bitmap file, the system will completely mill any white region to the specified depth while leaving black regions entirely unmilled. For the grayscale in between, the section is partially milled with the amount of milling based on the white content in the grayscale pattern. The pattern in Figure 5-20 is used to produce a sawtooth profile with a maximum depth of 2 μm and a period of 5.5 μm resulting in the 20 $^\circ$ blaze angle needed for efficient coupling.

Structures have been milled onto GaAs thin-films using the pattern shown in Figure 5-20 and are shown in Figure 5-21 (rotated 90 $^\circ$ from the bitmap pattern).

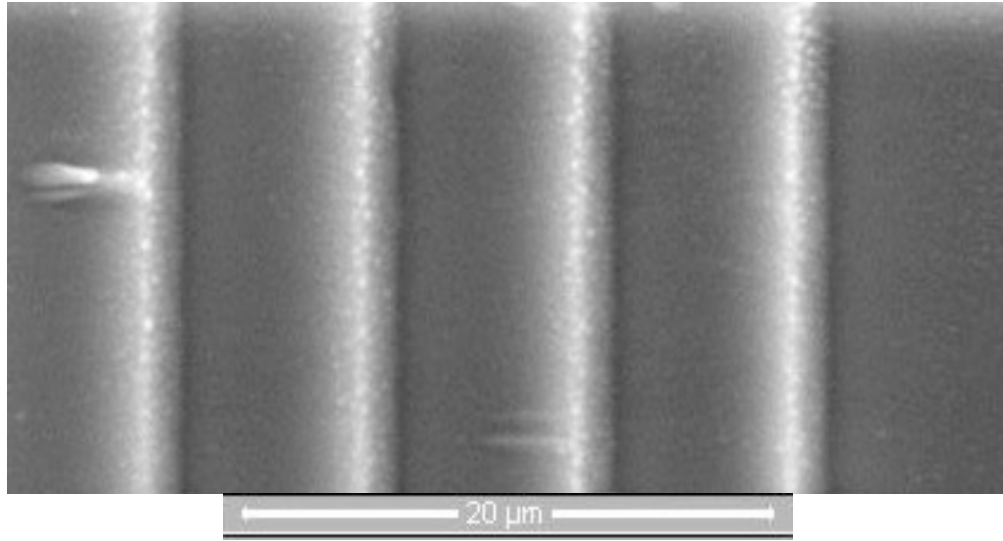


Figure 5-21: FIB milled grating structure on GaAs.

The milled structure shows the periodicity of the pattern structure created on a Quanta 3D FIB system (FEI Company, Hillsboro, Oregon). However, when viewed in cross section (see Figure 5-22), the blazed angle sawtooth structure is not correctly milled.

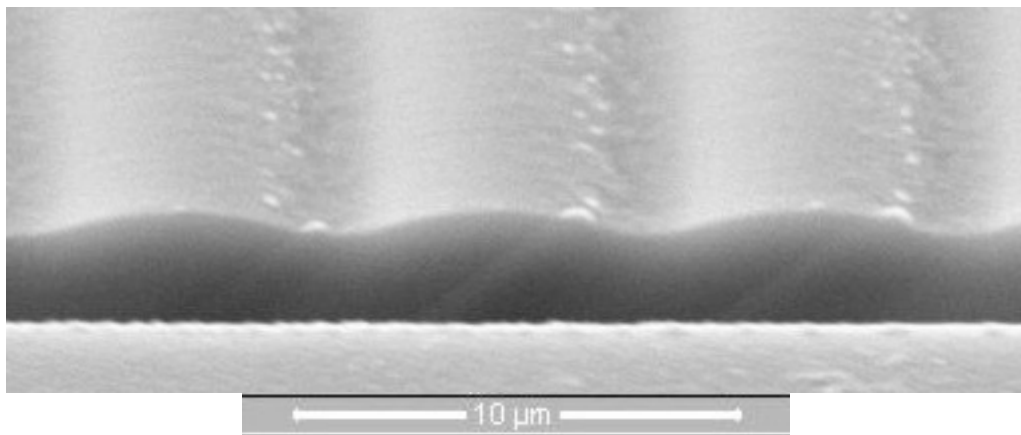


Figure 5-22: Cross sectional view of FIB milled grating structure on GaAs.

From Figure 5-22, it is evident that the sharp angles and vertical walls of the defined pattern are not correctly milled. This is likely caused by a re-deposition of material due to the large area and deep cuts needed to replicate the pattern. Alternative milling techniques, which would allow the structure to be fabricated in a number of consecutive layers thereby minimizing the material being removed at any given time, are currently being investigated.

CHAPTER 6

QCL-BASED LIQUID PHASE SENSING

In this chapter, liquid phase sensing systems based on evanescent field measurements using silver halide and GaAs planar waveguides are presented along with background on applications of liquid sensing, the state-of-the-art techniques, and the development and theory of the waveguides used.

6.1 Motivation

QCL-based liquid phase sensing is particularly suited to applications requiring high sensitivity and integrated, robust systems such as environmental monitoring and biological measurements.

6.1.1 Environmental

Evanescent field sensing is a well established technique for quantitative liquid phase analysis and in particular environmental monitoring^{1, 25}, and process analysis⁶, due to the opportunity of obtaining spectra from dissolved organic analytes. ATR-FTIR is routinely used for environmental monitoring of organics in water and process monitoring with sensitivities in the ppm to ppb range.^{1, 3, 7-19}

To avoid large absorbance due to water and as a preconcentration for organic analytes of interest, environmental applications often use membrane coated ATR waveguides. Coatings are typically polymer membranes which have hydrophobic properties allowing

organic compounds to be preferentially enriched over water. Enrichment layers which are thicker than the evanescent penetration depth transport the organic analytes of interest into contact with the evanescent field near the ATR element surface while preventing water from entering into this region²⁰. ATR coatings such as Teflon AF²¹, polyisobutylene²², low-density polyethylene²², and chemically modified poly vinyl chlorides²³ and polystyrenes²⁴ have been used to detect chlorinated hydrocarbons in water down to ppm levels. Ethylene propylene copolymer layers have been applied to sensing of benzene, toluene, and xylene at ppb levels⁵.

6.1.2 Biological

Transmission absorption measurements are frequently of limited utility due to the presence of scattering particles or agglomerates in biological applications^{25,26-28}, and since the penetration depth of IR radiation is restricted due to the strongly absorbing water background. Infrared spectroscopic measurements have substantial potential for biological applications due to the inherent molecular selectivity²⁹⁻³³, but have not been extensively used to date due to the achievable detection limits.

Among the biological applications attracting interest currently is detection of prion diseases or transmissible spongiform encephalopathies (TSEs) characterized by a misfolded protein known as a prion. The detection of prion protein folding has been demonstrated in the MIR using complex chemometric techniques in regions of the IR spectrum where absorption is specific to the folding conformation³⁴⁻³⁶. Table 6-1 shows

specific frequencies where MIR absorption in proteins is determined by the conformation.

Table 6-1: Absorption band positions for protein conformation³³.

Band Position (cm⁻¹)	Conformational Assignment
1693 and 1683	Turn/ β sheet
1654	α helix
1645	Hydrated β sheet
1635	β sheet (intramolecular)
1622	β sheet (intermolecular)

Changes in the conformation of a protein (or protein folding) causes a substantial change in the MIR spectra³⁷, which could be used for the detection of such diseases using a laser source matched to the spectral bands associated with the representative protein conformations. However, detection limits in the ng/mL (ppb m/v) range are needed for the detection of proteins in serum³⁶ rendering this a viable technique for protein analysis³⁸. In this thesis, a novel evanescent field waveguide was developed, which should provide the sensitivity levels required for diagnostic applications of IR evanescent field absorption spectroscopy.

6.2 State-of-the-art

Fiber optic evanescent field liquid sensing in the MIR is a well-established technique using a variety of techniques, sources, and materials, which will be discussed in the following.

6.2.1 ATR Waveguide Development

Decreasing the thickness of MIR waveguides has been investigated as a parameter for increasing the sensitivity of evanescent field measurements. Studies have achieved improved sensitivity via mechanical and chemical tapering of cylindrical fibers³⁹⁻⁴¹, and by thinning of planar waveguides^{28, 31, 42-44}. The theory of increased evanescent field sensitivity by decreasing waveguide thickness is discussed in Chapter 3.

6.2.2 IR Lasers in Liquid Sensing

While the majority of published research in the field of MIR evanescent field sensing utilizes FT-IR technology^{1,2,4,5,25,27,28}, only few contributions report on the applications of tunable diode lasers (TDLs)^{8,11}, light emitting diodes (LEDs)⁴⁵, CO₂ lasers²⁶ and synchrotron IR radiation⁴⁴ to improve the sensitivity. QCLs are of particular interest in this respect, as they promise a significant improvement in sensitivity over FT-IR due to their high spectral density. In addition, QCLs represent the only MIR laser light source, which can be tailored to the wavelengths needed to match absorption bands of a wide variety of analytically relevant molecules in environmental, process analytical, clinical, and security sensing applications.

6.2.3 QCLs in Liquid Sensing

Liquid phase spectroscopy with QCLs has received much less attention than gas phase sensing, and has been reported for transmission measurements in flow injection analysis⁴⁶ and for CO₂ measurement in aqueous solution⁴⁷. The study with silver halide waveguides demonstrated in this thesis presents the first application of QCL technology for evanescent field sensing, which is the most promising optical format for miniaturized liquid phase sensing in the MIR spectral region^{48,49}. Evanescent field-based chemical sensing with QCLs has since been demonstrated also by the Gmachl group for detection of organics with 300 μm cylindrical silver halide fibers⁵⁰.

6.3 IR Solid Core Fibers

Solid core MIR transmitting fibers⁵¹ are fabricated from a variety of materials such as polycrystalline silver halides ($\text{AgCl}_x\text{Br}_{1-x}$), amorphous chalcogenide glasses (As_2S_3 or As_2Se_3), single crystal sapphire (Al_2O_3), and fluoride glasses (fluorozirconate or fluoroaluminate). Table 6-2 summarizes the most common MIR fiber materials along with their transmission range and typical attenuation values.

Table 6-2: Infrared fiber materials (adapted from⁵²).

Material	Transmission Range (μm)	Attenuation (dB/m @ μm)
SiO_2	0.25 – 2	0.0004 @ 1.32
Sapphire	0.4 – 2.5	5 @ 2.9
Fluoride	0.5 – 3.1	0.015 @ 2.5
Chalcogenide	4 – 11	0.04 @ 6
Tellurium Halide	3 – 13	1 @ 9
Silver Halide	3 – 18	0.5 @ 11
Hollow Waveguides	0.9 – 25	0.5 - 1.5 @ 10.6

Silver halides^{1, 2, 5, 26, 53}, chalcogenide glasses^{4, 25, 40, 41,54} and other materials^{45, 55}, have been extensively applied for MIR liquid phase fiber optic sensing applications.

6.3.1 Silver Halide Fibers

Silver halides are polycrystalline materials transmitting radiation from 400 - 25000 cm^{-1} (0.4 - 25 μm) in dependence on their composition and have typical attenuation losses in the range of 0.5 dB/m at 10.6 μm ⁵⁶ rendering them ideal for MIR sensing applications. Silver halide fibers are a composite of silver chloride and silver bromide materials. Individual crystals of these materials are grown by the Bridgeman-Stockbarger method⁵⁷ where crystals are formed at high temperatures in a molten state

and cooled to form solid particles. Cylindrical ingots used in the production of solid core silver halide fibers are typically about 0.7 cm in diameter⁵⁷. Silver chloride and silver bromide are molten together and extruded into fibers of varying composition. Fiber properties such as refractive index, bulk absorption, and sensitivity to light are dependent on the material composition⁵⁷.

6.4 Planar Silver Halide Waveguide Sensing Systems

In this study, planar free-standing silver halide waveguides were developed and coupled to a QCL for the first demonstration of evanescent field sensing with these lasers.

6.4.1 Waveguide Preparation

The waveguides used in this work are of the composition $\text{AgCl}_{0.4}\text{Br}_{0.6}$ and have a refractive index of 2.1 and typical losses of 1 dB/m. Planar waveguides (PWGs) were created by press tapering unclad cylindrical silver halide fiber^{58,31} segments with a 700 μm diameter by our collaborators (A. Katzir, Tel-Aviv University, Israel). Fiber segments were heated to approx. 170 $^{\circ}\text{C}$ to increase malleability and pressed to form free-standing thin film waveguides with a thickness ranging from 300 μm to 190 μm , a width of 3 mm and a length of 35 mm as shown in Figure 6-1.

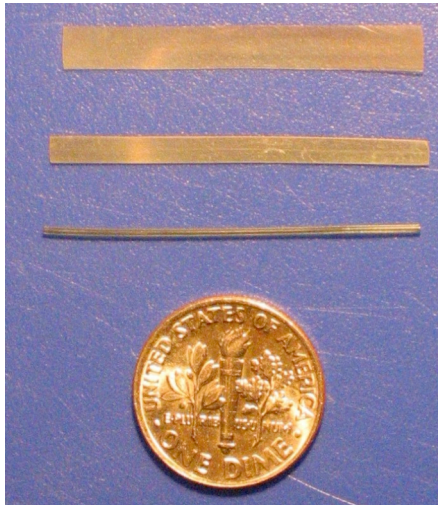


Figure 6-1: Planar silver halides with a thickness of 100 μm (top), 300 μm (middle), and a cylindrical fiber with diameter of 700 μm .

Sufficient optical quality of the planar waveguide end facets was achieved by cleaving the ends with a sharp blade followed by sequential polishing with diamond slurries of 3, 1, and 0.5 μm grain size at our laboratory (results shown in Figure 6-2).

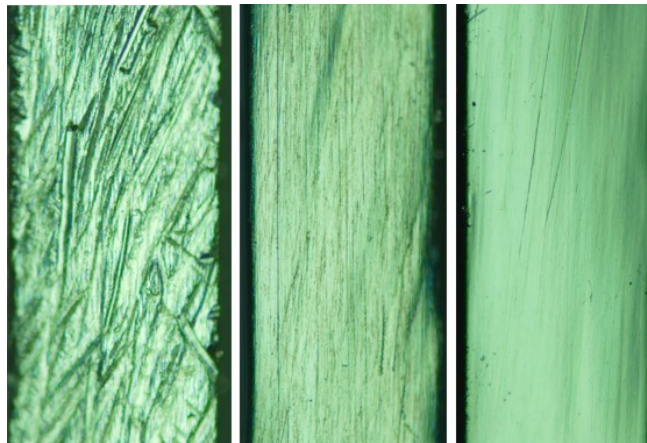


Figure 6-2: Planar silver halide fiber end facet after polishing with a) 3 μm , b) 1 μm , and c) 0.5 μm diamond slurries.

Planar waveguides were positioned on a copper holder, which clamped the waveguide strip near the ends providing a free-standing waveguide. The copper mount was plated with gold where in contact with the waveguide surface to avoid corrosion of the silver halide material by contact with base metals.

6.4.2 Urea Experiments

FT-IR measurements were performed by focusing the external collimated IR beam from a Bruker 66 spectrometer (Bruker Optics, Billerica, MA, USA) via a gold-coated off-axis parabolic mirror (OAPM, focal length: 25.4 mm; Janos Optics, Townshend, VT, USA) onto the end facet of a planar waveguide. Light from the distal end of the waveguide was

focused onto a liquid nitrogen cooled photoconductive mercury-cadmium-telluride (MCT) detector as schematically shown in Figure 6-3.

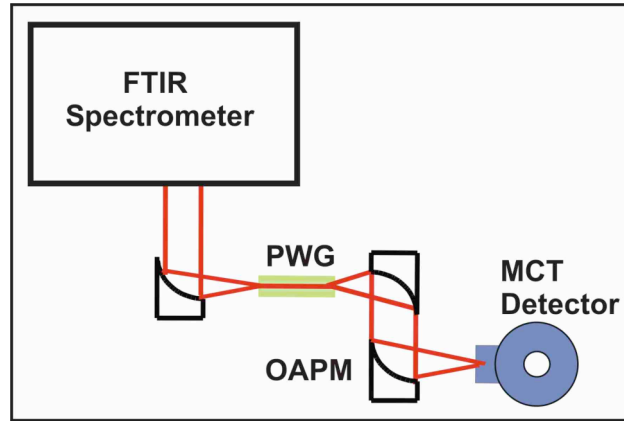


Figure 6-3: FTIR PWG experimental setup.

All spectra were recorded with a total of 100 averaged scans and a spectral resolution of 1 cm^{-1} at frequencies of $400 - 4000 \text{ cm}^{-1}$ using the Blackman-Harris-3-Term apodization function.

QCL measurements were recorded by dividing the laser beam into a measurement channel and a reference channel to enable pulse-by-pulse referencing of the laser signal. The measurement channel was focused onto the planar waveguide using OAPMs of focal length 25.4 mm while the reference beam was focused directly onto the MCT detector as schematically shown in Figure 6-4.

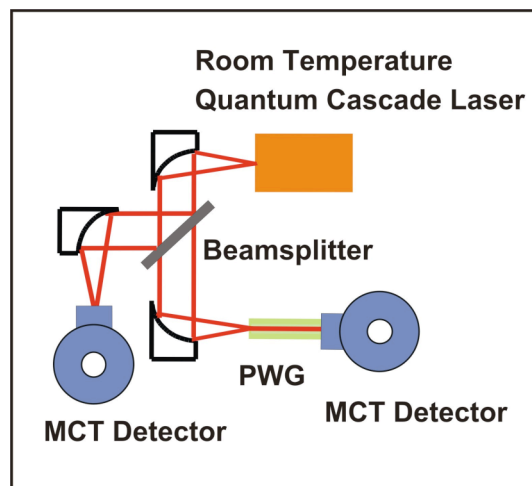


Figure 6-4: QCL-PWG experimental setup.

Light emanating from the distal end of the planar waveguide was pigtailed to the MCT detector.

The QCL (laser S1869e10, Alpes Lasers, Neuchâtel, Switzerland) was stabilized via Peltier cooling (temperature controller TC51, Alpes Lasers, Neuchâtel, Switzerland) at a temperature of 20 °C resulting in an emission frequency of 1650 cm^{-1} . The laser was modulated with a pulse duration of 200 ns at a period of 25.8 μs (TPG128 pulse generator, Alpes Lasers, Neuchâtel, Switzerland) and amplitude was controlled by an external power supply set to 20 V avoiding saturation of the detectors. Data was recorded with an oscilloscope (Tektronix, TDS 3032, Beaverton, OR, USA) evaluating the MCT signals.

Solutions were prepared by dissolving urea (Sigma Aldrich, Milwaukee, WI, USA, 99.5% pure) crystals in methanol (Fisher Scientific, Fairlawn, NJ, USA, reagent grade)

for deposition onto the waveguide surface. Sensitivity of FT-IR and QCL measurements to the amount of urea at the planar waveguide surface was tested by depositing a 10 μL droplet of a methanol with dissolved urea solution (1.6023 g urea dissolved in 50 mL methanol) onto the waveguide surface. Methanol was then evaporated causing urea crystals to precipitate at the waveguide surface. A measurement was recorded followed by an additional solution droplet added to the previously formed urea crystals at the waveguide surface. Repetition of this procedure resulted in an accumulation of urea crystals at the waveguide surface as shown in Figure 6-5 leading to an increase of the evanescent field absorption signal.

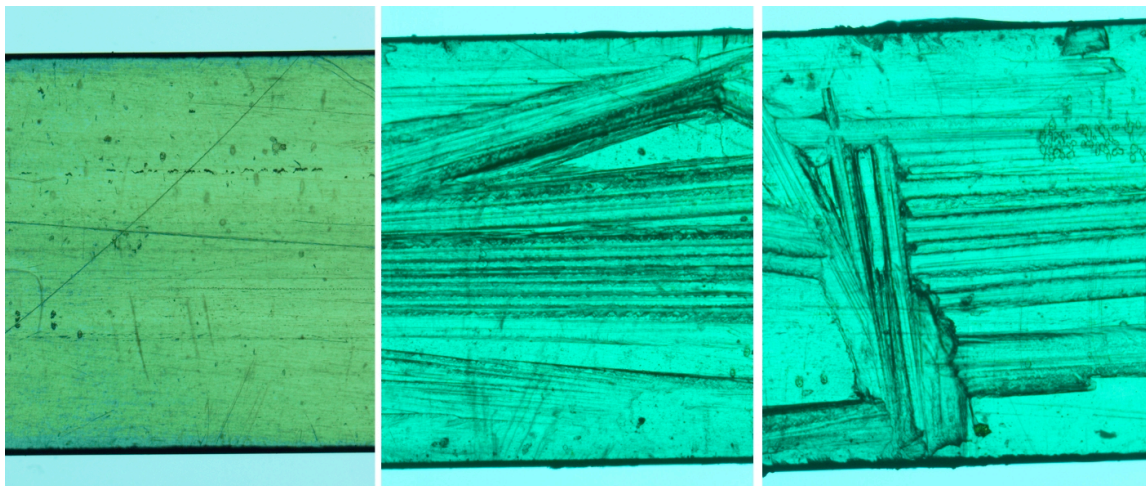


Figure 6-5: Bare AgX fiber surface (left) and urea crystals at AgX waveguide surface after deposition and evaporation of 30 μL and 40 μL of methanol-urea solution, respectively.

Measurements with the planar silver halide waveguide coupled to a FT-IR spectrometer yielded an increase of the amide stretch absorption band centered at 1600 cm^{-1} with

increasing amounts of urea precipitated at the waveguide surface as shown in Figure 6-6. Ten droplets of 10 μL each were deposited on the waveguide surface, each resulting in 0.32 mg of urea precipitate after evaporation. Spectra were collected after methanol had evaporated resulting in evanescent field absorbance features of 0.32 mg to 3.20 mg of urea at the waveguide surface.

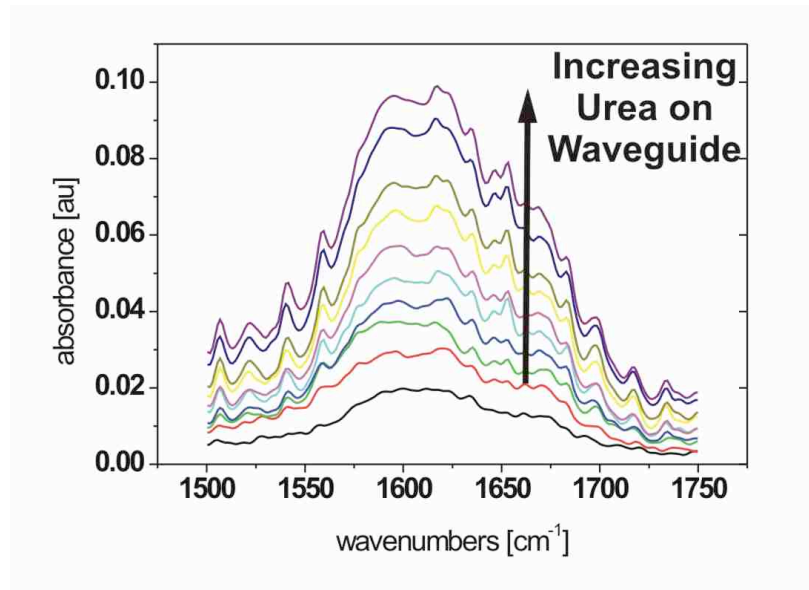


Figure 6-6: FT-IR urea band increases with increasing deposition of material.

The spectrum of urea recorded during FT-IR PWG evanescent field absorption experiments was used to verify the spectral overlap between the radiation emitted from the 1650 cm^{-1} QCL and the urea absorption band as shown in Figure 6-7.

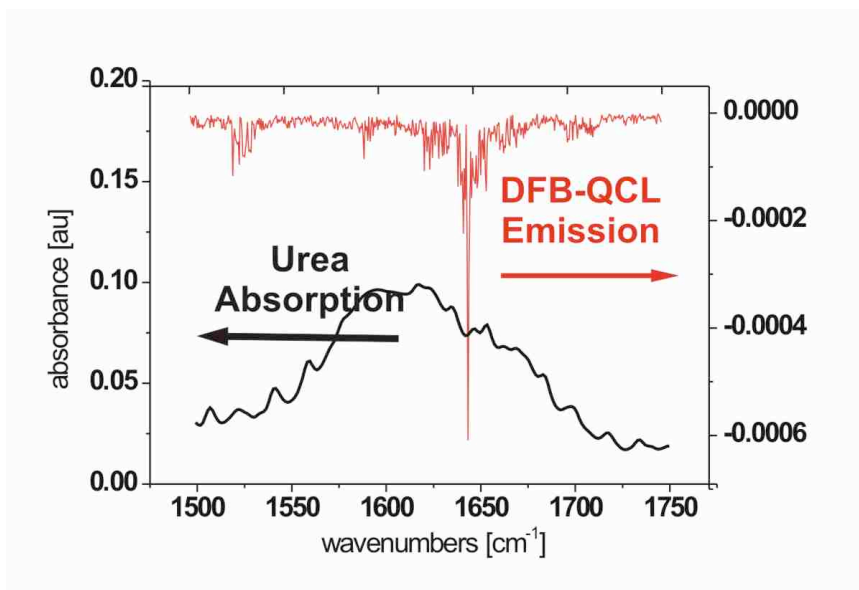


Figure 6-7: Overlap of QCL emission and urea absorption frequency.

The overlap shown in Figure 6-7 occurs only at a side band of the laser causing the QCL evanescent field absorption measurements to not take full advantage of the radiant power provided by the laser.

Urea deposition at the waveguide surface for QCL PWG evanescent field absorption measurements used the same procedure applied during the FT-IR PWG experiments. Damping of the QCL signal as the amount of precipitated urea at the PWG surface increases from 0 mg to 2.88 mg in increments of 0.32 mg is shown in Figure 6-8.

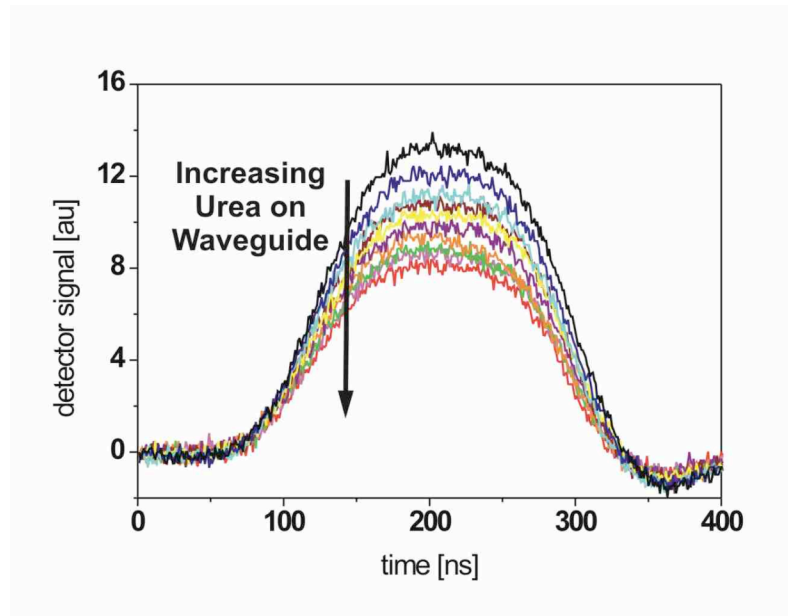


Figure 6-8: QCL pulse damping due to urea absorption.

Individual laser pulses are shown as signal as a function of time with decreasing amplitude as the amount of urea precipitate on the waveguide surface increases.

The system response is shown in Figure 6-9 where the signal damping generated by integrating the area under each curve shown in Figure 6-8 is plotted as a function of urea deposited at the waveguide surface in mg.

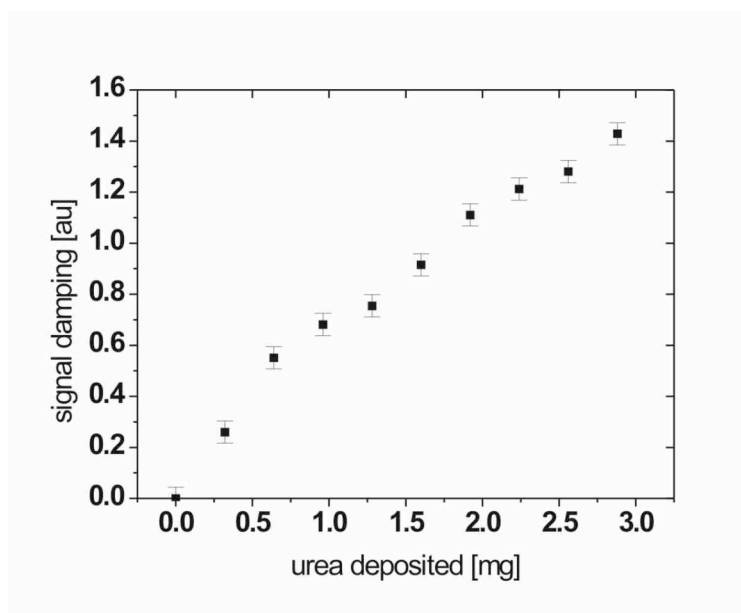


Figure 6-9: Response curve to urea surface deposition.

The limit of detection of the system was found to be 80.7 μg of urea, based on the 3σ criterion providing an improvement by a factor of 4 compared to the limit of detection (LOD) achieved for the corresponding FT-IR PWG measurements, despite only a side band of the laser overlapping with the urea amide absorption.

6.4.3 Acetic Anhydride Experiments

The experimental setup and measurement conditions for the FT-IR acetic anhydride measurements are identical to those used for the urea measurements described above. QCL measurements again utilized the 2-channel setup shown in Figure 6-10.

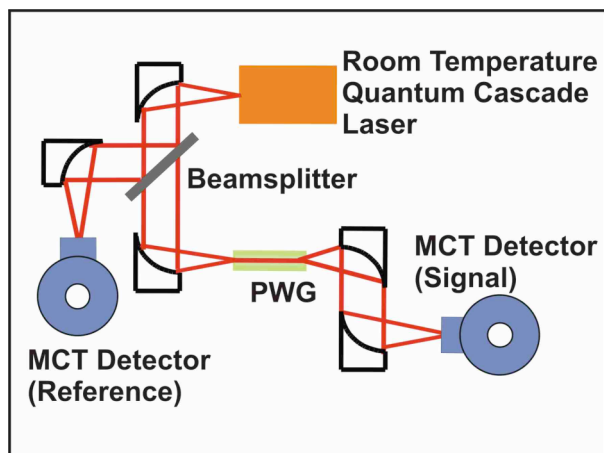


Figure 6-10: Acetic anhydride QCL experimental setup.

The QCL (laser s1537, Alpes Lasers, Neuchâtel, Switzerland) was operated at a temperature of 0 °C providing an emission frequency of 974 cm^{-1} and modulated at a pulse duration of 40 ns with a period of 2.64 μs . The amplitude was controlled by an external power supply set to 20 V giving the maximum signal possible while avoiding saturation of the detector.

The emission of the QCL overlaps with the $\text{CH}_3\text{-C}$ bending absorption of acetic anhydride causing damping of the laser radiation in the presence of analyte, while the solvent acetonitrile has a spectral window in this wavelength range. Transmission measurements were performed using transmission cell (Pike Technologies, Madison, WI, USA) with NaCl windows and a 200 μm pathlength to verify the overlap of the QCL emission frequency with the analyte absorption.

Acetic anhydride QCL data was collected using a high-speed data acquisition system (Saturn, AMO, Aachen, Germany) providing a simultaneous dual-channel sampling rate of 100 MHz averaging 10^6 data curves.

Acetic anhydride (Sigma Aldrich, Milwaukee, WI, USA, 99.9% pure) was dissolved in acetonitrile (VWR, West Chester, PA, USA, HPLC grade) providing a calibration series with various concentrations of acetic anhydride. The sensitivity of evanescent field absorption measurements to the volume of acetic anhydride solution at the waveguide surface was tested by deposition of 1 μ L droplets with concentrations of 0.11, 0.85, 2.12, 4.24, and 10.59 M (corresponding to 10.8, 86.4, 216, and 432 μ g of acetic anhydride, respectively) onto the waveguide surface using an Eppendorf pipette (Brinkmann, Westbury, NY, USA). FT-IR absorption spectra were recorded via evanescent field measurements against the bare waveguide as a reference. Drops were deposited over a controlled area at the waveguide center 1cm long and spanning the width of the waveguide as shown in Figure 6-11.

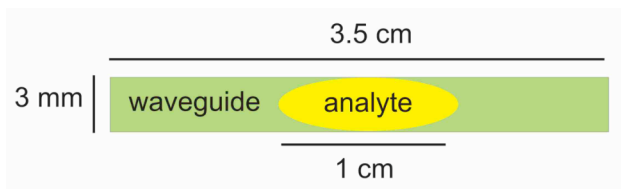


Figure 6-11: Acetic anhydride deposition at the waveguide surface.

Spectra of acetic anhydride were recorded with the solution phase present at the waveguide surface.

Spectra of 1 μL droplets with concentrations of 0.11, 0.85, 2.12, 4.24, and 10.59 M of acetic anhydride in acetonitrile resulting in a total acetic anhydride volume of 0.01, 0.08, 0.2, 0.4, and 1 μL respectively (corresponding to 10.8, 86.4, 216, and 432 μg) deposited at the waveguide surface are shown in Figure 6-12.

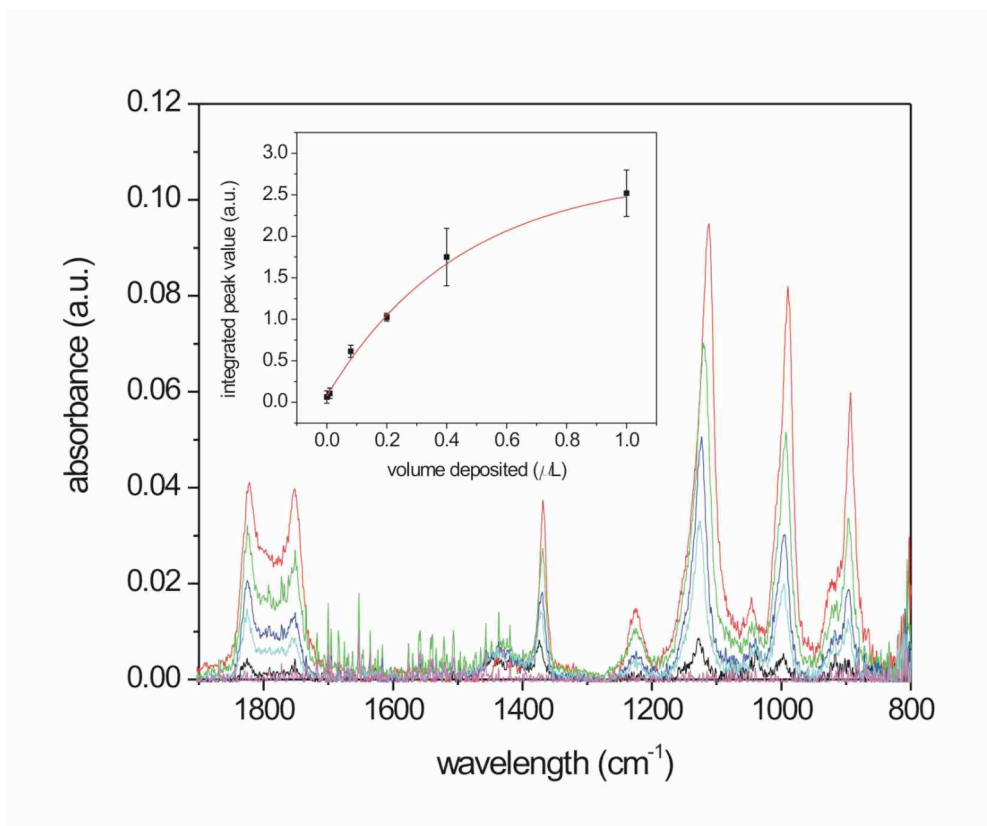


Figure 6-12: FT-IR evanescent absorption spectra for acetic anhydride.

The acetic anhydride spectrum can be clearly identified by the increase in the intensity of absorption features with increasing volume of acetic anhydride solution deposited at the waveguide surface. The inset of Figure 6-12 shows the evanescent field absorption response, which was fit with an exponential function with an R^2 value exceeding 0.99 indicating Lambert-Beer behavior. The error associated with these measurements can be

attributed to small variations resulting from manual deposition of the droplets at the waveguide surface. The lowest volume detectable during FT-IR PWG experiments was determined to be 0.01 μL based on the 3σ criterion.

Figure 6-13 shows the overlap between the acetic anhydride absorption band and the QCL emission frequency.

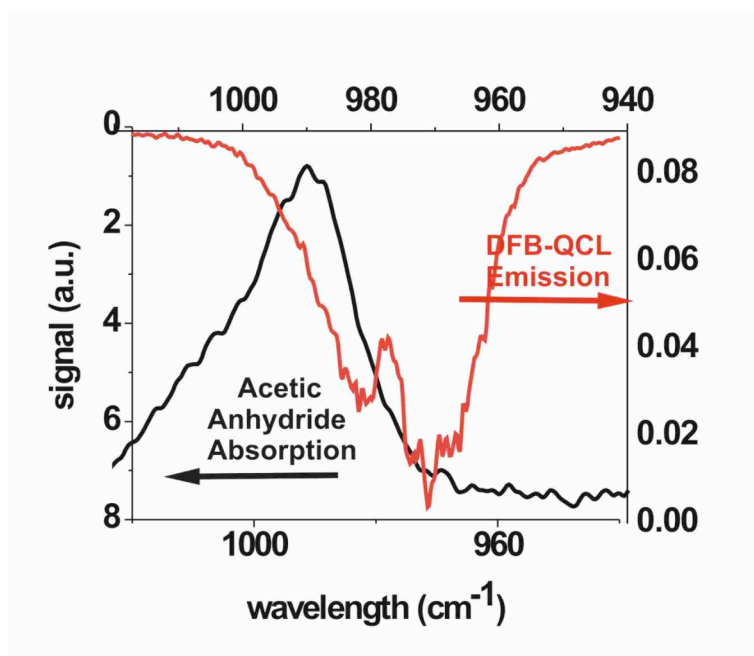


Figure 6-13: Overlap of QCL emission and acetic anhydride absorption band.

Transmission absorption measurements were performed verifying overlap between an absorption band characteristic for acetic anhydride and the emission frequency of the QCL at 974 cm^{-1} . Collimated radiation from the QCL passed through a thin film transmission cell with a layer thickness of 200 μm filled first with acetonitrile (Figure 6-

14, dotted line), then with a solution of 1 % acetic anhydride in acetonitrile (dashed line), and finally with pure acetic anhydride (solid line).

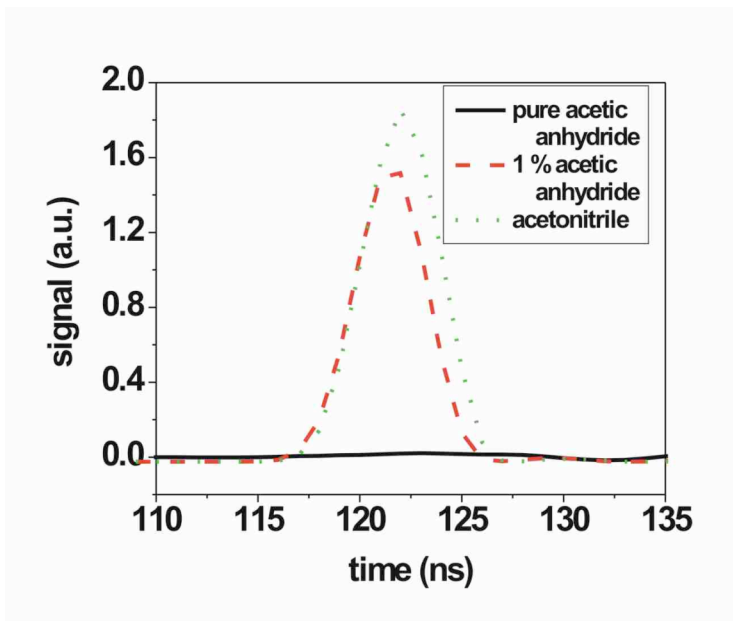


Figure 6-14: Transmission cell measurements.

Increased damping of the radiation emitted from the QCL in the presence of increasing amounts of acetic anhydride verified overlap between the laser emission frequency and an absorption feature characteristic for acetic anhydride.

Acetic anhydride solutions were deposited onto the PWG surface using the same procedure as for FT-IR measurements causing damping of the QCL signal with respect to the reference signal due to molecule specific evanescent field absorption. As shown in Figure 6-15, laser pulses have decreasing amplitude as the amount of acetic anhydride is increased.

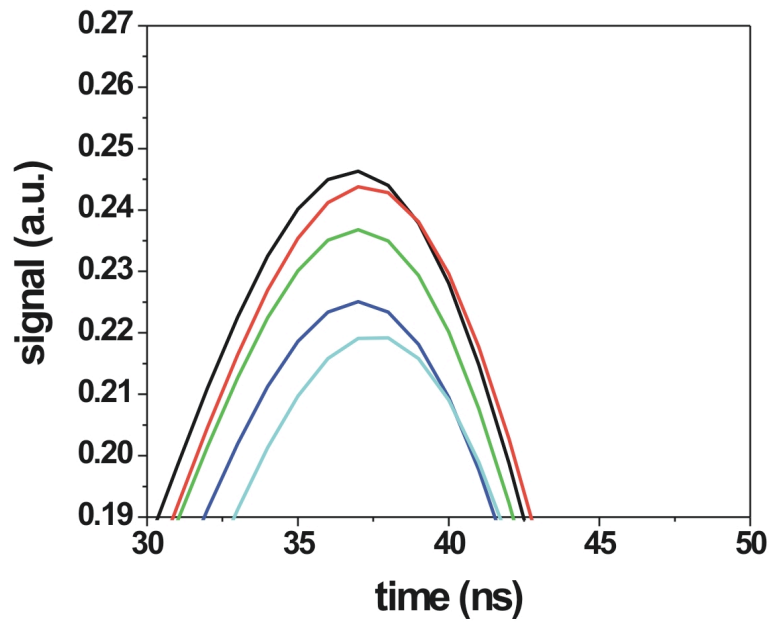


Figure 6-15: QCL Damping due to acetic anhydride absorption due to: from the top 0, 0.01, 0.1, 0.2, and 1 μL droplets at the waveguide surface.

Figure 6-16 shows the system response curve revealing the same trend as a function of deposited volume at the waveguide surface as previously determined during the FT-IR PWG experiments (inset Figure 6-12).

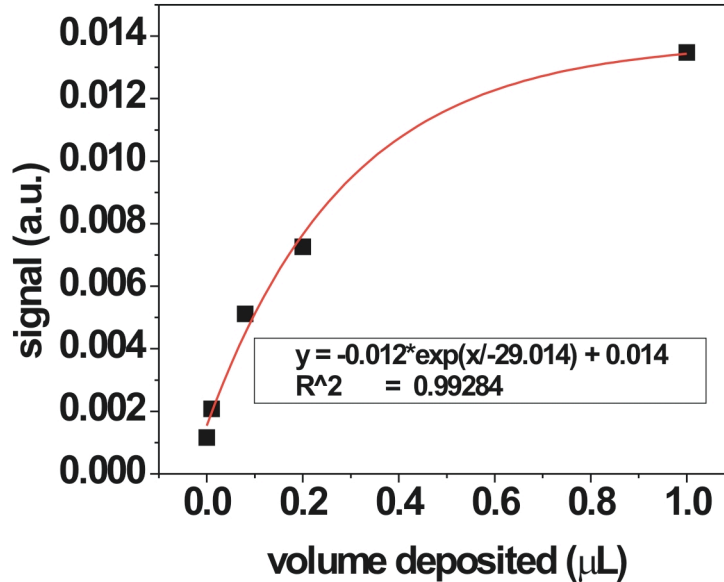


Figure 6-16: QCL response curve for acetic anhydride surface deposition.

The data was again fitted with an exponential function resulting in an R^2 value of greater than 0.99. QCL PWG evanescent field absorption measurements gave a limit of detection of 0.01 μL (10.8 μg) of solution deposited at the waveguide surface. In this case, the LOD for the QCL PWG measurements corresponds to that achieved during the FT-IR PWG experiments. The limit of detection for the QCL system could be significantly improved with a stronger overlap between the laser emission frequency and the analyte absorption feature as Figure 6-13 clearly shows that the emission of the currently available QCL overlaps only in the side mode region with the acetic anhydride absorption feature. A laser emitting at 990 cm^{-1} rather than 974 cm^{-1} would provide a better match to the absorption maximum promising a significant improvement of the LOD comparable or beyond the improvement seen in the urea case.

6.4.4 Results

Results achieved with the first QCL PWG evanescent field absorption measurements correspond well to measurements with conventional FT-IR evanescent field sensing in both urea and acetic anhydride measurements. The obtained results demonstrate the potential of mid-infrared QCL evanescent field sensing achieving limits of detection that are at least similar – and in the case of urea already significantly improved in a simpler and more compact sensing system.

In both the urea and acetic anhydride measurements, the achievable sensitivity of QCL PWG measurements would benefit from a better match between the QCL emission frequency and the spectral position of the analyte absorption feature. The limited commercial availability of QCLs at relevant emission frequencies currently prohibits ideal overlaps. An ideally matched laser emission frequency would provide sensitivity improvements of at least an order of magnitude in contrast to FT-IR PWG measurements. Additional sensitivity improvements are anticipated for thinner waveguides due to increased intensity in the evanescently guided modes. However, PWG end coupling becomes increasingly difficult with planer waveguide strips of a thickness $< 300 \mu\text{m}$ and requires other coupling methods.

Pigtail coupling, where the waveguide is brought in close proximity to the laser end facet, was investigated and found to be a far more efficient end coupling method between the QCL and planar waveguide. Figure 6-17 compares the two coupling methods by showing the laser output as a function of applied pulse amplitude along with the point on

this curve where the laser saturates the detector through the planar waveguide for each method.

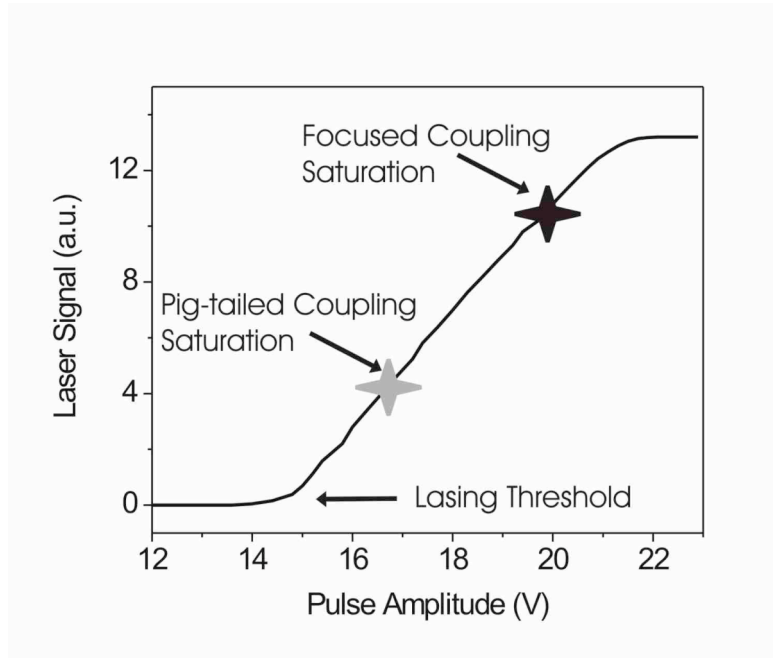


Figure 6-17: Coupling efficiency.

The focused coupling method requires a higher laser output for detector saturation through the waveguide than the pigtail coupling.

The pigtail method also shows a much higher sensitivity due to the higher throughput. The damping of a QCL pulse due to a 1 μL drop of acetic anhydride on the fiber surface is shown in Figure 6-18 for both methods with a much larger change for pigtailling (bottom set of curves) than focusing with OAPM (top set of curves).

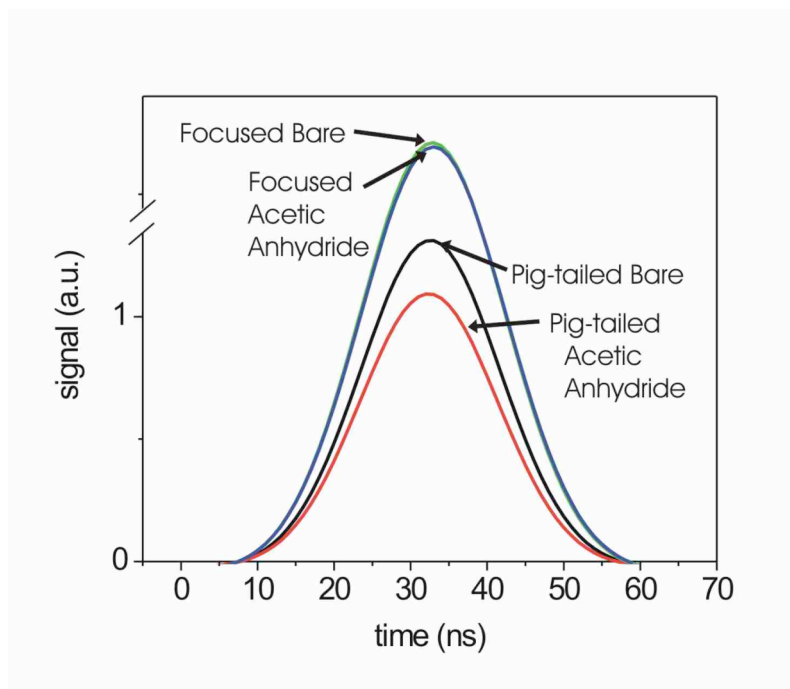


Figure 6-18: QCL damping by different coupling methods. The scale for these two sets of curves does not correspond; and they have been placed on the same graph only for comparison.

Pigtail coupling has the inherent disadvantage that it cannot be split into two separate channels to allow for referencing and has therefore not been used for analytical measurements. The QCL has a high degree of variation between pulses as well as drift causing sensitive quantitative analysis to be impossible without referencing.

6.5 Planar Single-Mode GaAs Waveguides

This study demonstrates MIR evanescent field sensors based on novel single-mode GaAs thin-film planar waveguides (design discussed in Chapter 5). These waveguides are designed to improve the sensitivity of evanescent field absorption measurements providing a platform for the development of highly integrated and miniaturized MIR liquid phase sensing system aiming at incorporating a QCL and waveguide on a single chip.

6.5.1 Waveguide Preparation

The waveguides were jointly designed by ASL, Georgia Tech and the Mesoscopic Physics group, Univ. Neuchâtel, and were deposited at the University of Neuchâtel by molecular beam epitaxial growth of GaAs on a Si-doped GaAs wafer substrate. This substrate was selected to effectively absorb stray light in the material causing light passing outside the optical waveguide to be suppressed. The Si-doped GaAs has an absorption due to free carriers of over 300 cm^{-1} at $l = 10.3 \text{ mm}$.

The GaAs material making up the waveguiding layer has the advantage of exhibiting very low absorption across the entire mid-infrared to a wavelength of $16 \mu\text{m}$. At this wavelength, the first multiphonon absorption features are present. The Reststrahlen band will completely eliminate radiation for wavelengths of approximately $25 - 40 \mu\text{m}$ ⁵³. To achieve low loss waveguides, an $\text{Al}_x\text{Ga}_{1-x}\text{As}$ layer is grown providing a relatively large refractive index step between the GaAs waveguide and its surrounding materials.

The waveguide consisted of the GaAs wafer and a 6 μm $\text{Al}_{0.2}\text{Ga}_{0.8}\text{As}$ cladding layer, followed by a 6 μm GaAs core layer fabricated by epitaxial growth as shown in Figure 6-19.



Figure 6-19: Waveguide composition.

As shown in Figure 6-19, a 300 nm Si_3N_4 layer was deposited by chemical vapor deposition on some waveguide samples to protect the surface against etching by the sample solution.

Strip waveguides were created from the wafer by scoring along the crystal axis with a diamond knife and breaking along the score. The waveguides created were each 0.5 cm wide and varied in length from 1 to 2.5 cm as shown in Figure 6-20.

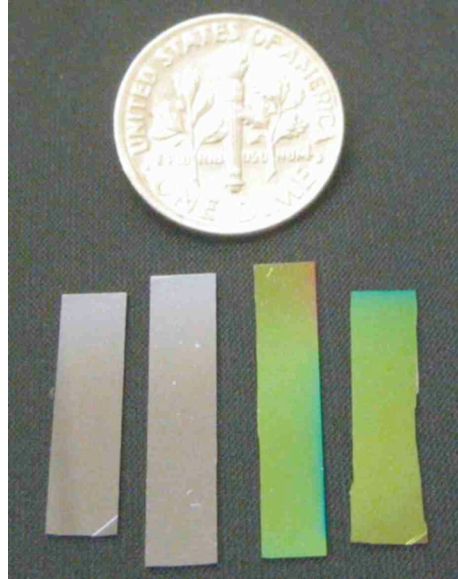


Figure 6-20: GaAs thin-film strip waveguides with silicon nitride protective overlayer (right), and without (left).

Scanning electron microscopy (SEM) images shown in Figure 6-21 were used to verify the optical quality of the waveguide end facets.

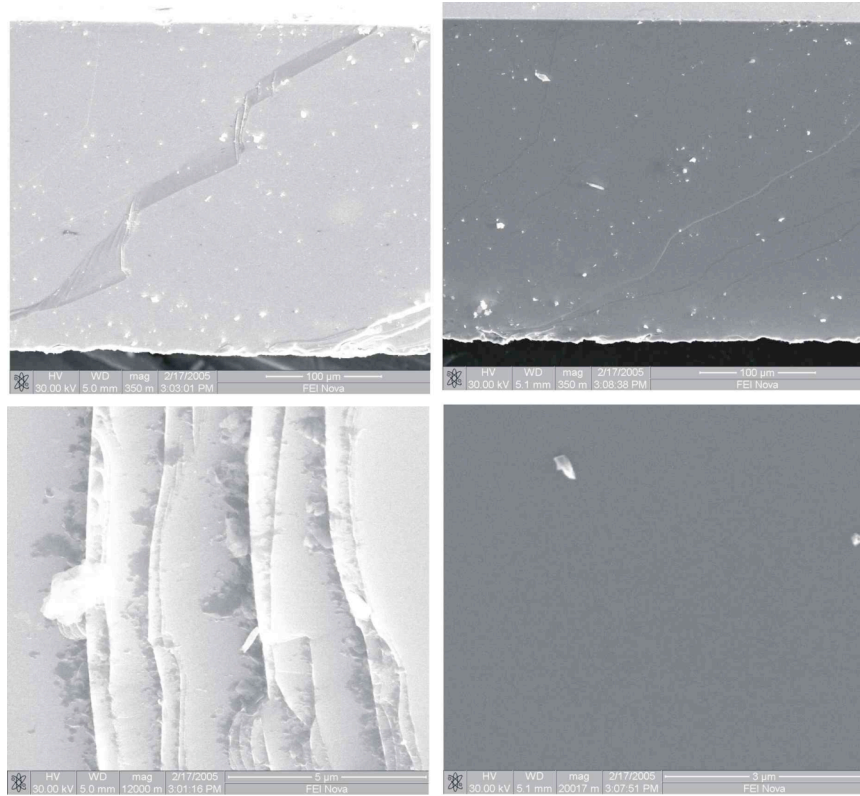


Figure 6-21: SEM images of a GaAs waveguide end facet.

The top images in Figure 6-21 show the entire wafer thickness with the left image capturing a fault-like defect while the right image is defect free. The bottom left image shows a defect up close with plate features approx. 2 μm in width. The bottom right image shows a defect free section.

Defects found at waveguide end facets were most likely due to off-axis breaks in the wafer and were large enough to cause scattering at IR wavelengths. However, these defects were confined to discrete fault lines with large sections of defect free waveguide between. In most cases, defects were not severe enough to prevent coupling and sufficient optical quality is achieved at the waveguide end facets.

6.5.2 Experimental

FT-IR spectra were recorded using waveguides with a length of 1 cm and a width of 0.5 cm. Coupling was achieved by focusing collimated radiation from an FT-IR spectrometer (Bruker IFS 66, Bruker Optics, Billerica, MA) onto the waveguide end facet using an off-axis parabolic mirror with a focal length of 3 inches. Light from the distal end of the waveguide was collected by pigtail coupling of the waveguide to the ZnSe window of a liquid nitrogen cooled MCT detector (Kolmar Technologies, Newburyport, MA).

Quantitative evanescent field measurements with GaAs waveguides were demonstrated by coupling laser s1537 emitting at 974 cm^{-1} ($10.3\text{ }\mu\text{m}$), which overlaps with the $\text{CH}_3\text{-C}$ bending vibration of acetic anhydride. The laser was operated at a temperature of $10\text{ }^\circ\text{C}$, a pulse duration of 40 ns, and a period of $2.64\text{ }\mu\text{s}$, and a pulse amplitude of 22 V. The QCL was pigtail coupled to the waveguide as shown in Figure 6-22 and radiation from the distal end of the waveguide was collected by an MCT detector, similar to the FT-IR experiments.

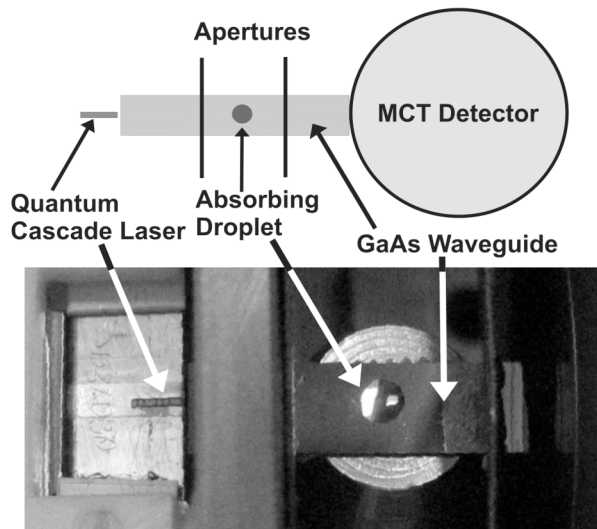


Figure 6-22: Experimental setup of QCL coupled to GaAs thin-film waveguide.

Acetic anhydride obtained from Sigma Aldrich (Milwaukee, WI, USA) at 99.9% purity was deposited at the waveguide surface in 0.5 μL droplets, each covering a length of 3 mm at the center of the waveguide surface as shown in Figure 6-22. Acetonitrile was obtained from VWR (West Chester, PA, USA) at HPLC grade serving as a control experiment with a non-absorbing medium.

6.5.3 Results

Figure 6-23 shows single beam FT-IR transmission spectra recorded by coupling radiation through the long axis of different waveguides with and without silicon nitride overlayer, respectively. For reference, a detector response curve without waveguide is provided.

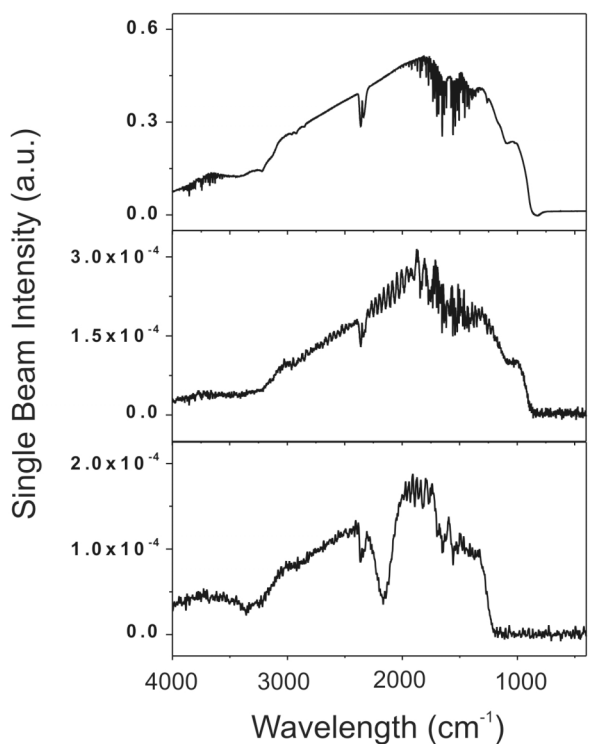


Figure 6-23: FTIR single beam spectra through GaAs thin-film waveguides showing reference without waveguide (top), waveguide without silicon nitride overlayer (middle) and waveguide with silicon nitride overlayer (bottom).

Characteristic absorption features for gaseous CO_2 at approx. 2300 cm^{-1} , and water vapor at approx. 1600 cm^{-1} and 3700 cm^{-1} resulting from the ambient environment can be seen in all spectra. Spectra recorded through the waveguides are characterized by much lower signal-to-noise ratios, due to the comparatively small amount of radiation coupled into these thin film planar waveguide structures. Besides the decrease in transmitted light energy, no change of the spectral transmission window occurs in comparison between the GaAs waveguide (middle spectrum in Figure 6-23) and the detector response curve (top spectrum in Figure 6-23). These spectra reveal that broadband IR light is able to

propagate despite waveguide being optimized to transmit light at 10.3 μm . The spectra for the waveguide overcoated with silicon nitride clearly reveal additional solid state absorption features centered at 2150 cm^{-1} , and a transmission cut-off at 1250 cm^{-1} resulting from the additional Si_3N_4 layer (bottom spectrum in Figure 6-23).

The response of the bare GaAs waveguide to evanescent absorption was tested with FT-IR using the coupling setup described above. Acetic anhydride droplets of 5 μL and 10 μL were deposited on the waveguide surface as described for silver halide fiber measurements. The evanescent absorption spectra are shown below in Figure 6-24.

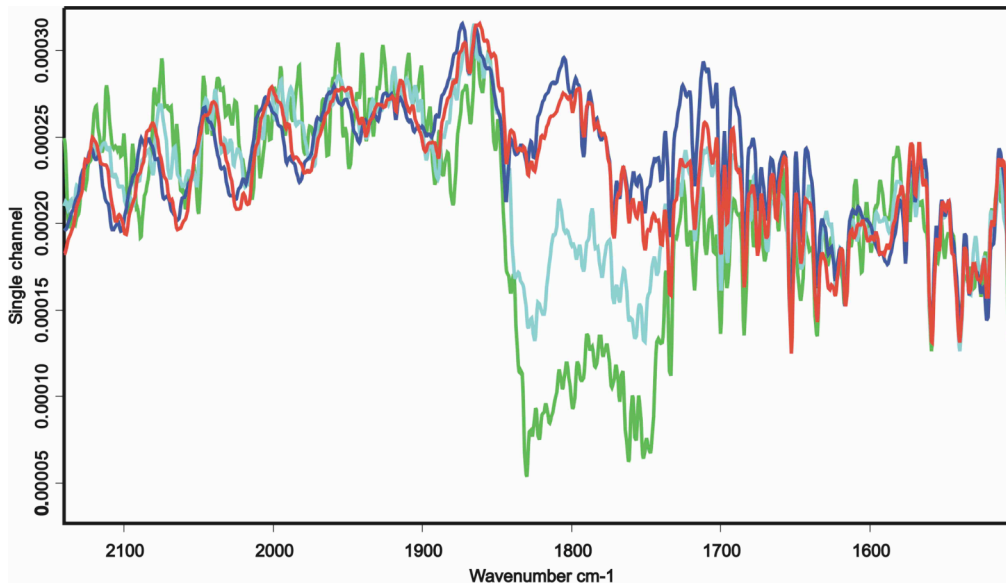


Figure 6-24: FT-IR coupled to GaAs thin-film waveguides absorption spectra for bare waveguide (dark blue), 5 μL drop of acetic anhydride on waveguide surface (light blue), 10 μL drop of acetic anhydride on waveguide surface (green) and surface drops evaporated (red).

The high level of noise in Figure 6-24 illustrates the very small amount of light coupled through the waveguide during these measurements. Despite the minimal signal in the measurements, the 10 μL drop was detected with a signal-to-noise ratio of 10 based on peak integration.

With the QCL-GaAs sensing system, a response curve for the change in intensity through the waveguide (I/I_0) as a function of the length of the waveguide covered by absorbing analyte was generated through sequential addition of three droplets of the same volume and surface area. Evanescent field absorption measurements were performed at the surface of both single-mode GaAs thin-film waveguides and a multimode silver halide planar waveguide with a thickness of 300 μm (width: 3 mm; length: 35 mm). This allowed a direct comparison between the two waveguides. Light was coupled into the silver halide waveguide at or near the critical angle giving the most sensitive evanescent field measurements achievable with this waveguide.

Figure 6-25 shows response curves for both waveguides with the circular symbols representing the response obtained with the GaAs waveguide fitted with a linear regression function (solid line). The response for the silver halide waveguide is indicated with triangular symbols and a dashed linear regression fit.

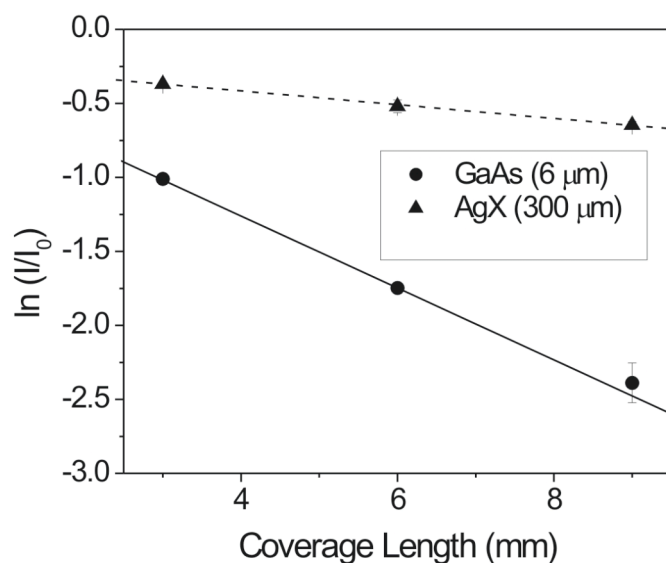


Figure 6-25: System response for GaAs and AgX waveguides coupled to QCL.

The linear fit of the GaAs response function in Figure 6-25 has a slope of 0.24, while the slope of the response function for the silver halide waveguide is 0.05. This demonstrates an improvement in evanescent field sensitivity by a factor of 5 for the single mode GaAs waveguide. The sensitivity increase obtained from the thin film GaAs waveguide is attributed to an increase in r , which is the fractional power guided outside the core of the single mode waveguide as discussed in Chapter 3. As the current waveguide structure is optimized for low loss rather than maximum fractional power outside the waveguide core, it is expected that by increasing r an improved sensitivity by one order of magnitude or more can be obtained.

In order to evaluate the accuracy of these measurements, the theoretical change in transmission due to evanescent absorption was calculated. The value of the molar

absorptivity for acetic anhydride at a wavelength of 974 cm^{-1} ($10.3\text{ }\mu\text{m}$) was determined experimentally. An FT-IR transmission absorption measurement was obtained with pure acetic anhydride and a pathlength of $15\text{ }\mu\text{m}$ was used giving a molar absorptivity value of $2.69\text{ L/mol}\cdot\text{mm}$ as calculated from the Lambert-Beer law (Eqn. 3.1).

By substituting the absorbance (A) for 1 minus the change in transmission in Eqn. 3.1, the theoretical change in transmission due to evanescent absorption of a single drop at the surface of the GaAs waveguide was calculated to be 0.803. This value is based on an extinction coefficient for acetic anhydride of $2.69\text{ L/mol}\cdot\text{mm}$, a pathlength of 3 mm (the diameter of a single drop, and a fractional evanescent power of $2.3\text{ e-}3$, as discussed in Chapter 5. The experimentally obtained value of the change in transmission due to a single drop at the GaAs waveguide surface is 0.638. The difference between the calculated and the experimentally obtained value of approximately 20 % is attributed to edge effects such as scattering resulting from the confined droplet at the waveguide surface.

In addition to the sensitivity improvement, single mode GaAs waveguides also provide improved control on the evanescent field leading to more quantitative measurements at the waveguide surface. As discussed in Chapter 3, the penetration depth and strength of the evanescent field is dependent on the coupling angle and therefore the mode. As each individual mode propagating through a waveguide gives a different evanescent field profile, multimode waveguides give a distribution of evanescent field intensities and profiles. A waveguide supporting only a single mode gives a well-defined evanescent

field independent of coupling. Figure 6-26 shows the mode profile calculated by our collaborators at the University of Neuchâtel for the GaAs waveguide, as well as profiles for a high order and the fundamental mode in a multi-mode silver halide waveguide.

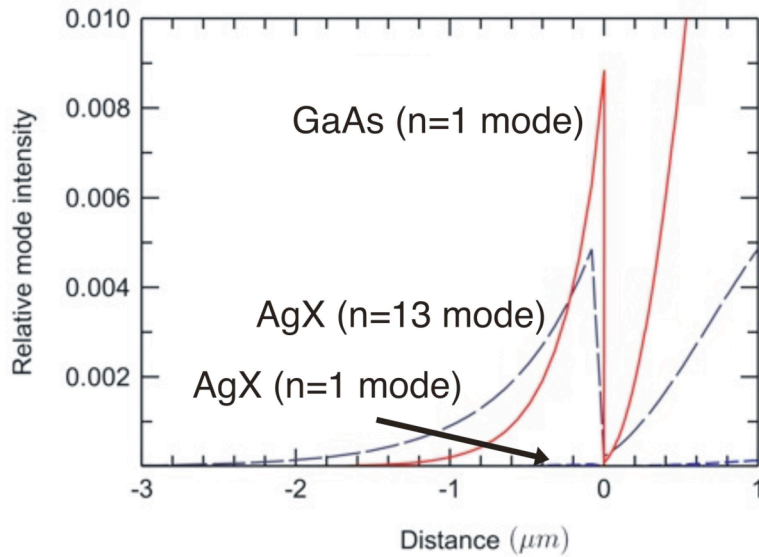


Figure 6-26: Mode profile for GaAs and AgX waveguides.

The profiles shown in Figure 6-26 show the relative mode intensity as a function of position along in the waveguide perpendicular to the direction of propagation. On this distance scale, zero corresponds to the surface of the waveguide. The distance from zero in the negative direction corresponds to the surrounding material, and the light in this region is the evanescent field. The profile shown in red is for the single mode supported by the GaAs waveguide developed in this work while the profile shown in the black long dashed line corresponds to a high order mode ($n = 13$) and the short dashed black line a low order mode ($n = 1$) for a multimode AgX fiber. The AgX low order mode profile is

very near the axis due to its low intensity relative to the other modes showing the large deviation between evanescent intensities in multimode waveguides.

As the experiments discussed above comparing the evanescent sensitivity with the GaAs and AgX were performed with light coupled into the AgX waveguide at high angles, we can expect primarily high order modes to be excited. Based on the similar intensities between the high order AgX mode and the GaAs mode, our five times sensitivity improvement for the GaAs over AgX waveguide is consistent with the theoretically expected improvement.

In the multimode waveguide, both of the AgX modes shown as well as all modes in between would be supported and the evanescent field would clearly be a distribution of intensities. The GaAs waveguide supporting only a single mode would therefore provide more quantitative measurements as compared to the AgX waveguide due to superior modal control.

It is also of interest to note the high evanescent intensity of the GaAs waveguide near the surface in Figure 6-26 compared with any mode of the AgX waveguide. This would particularly allow for sensitive measurements of molecular monolayers at the waveguide. This high intensity at the waveguide surface and sharp decay into the surrounding material is due to the large refractive index contrast between the waveguide and surface layer probed. In a next step, these waveguides will be tested for studies on protein conformation to reveal their full potential for biological IR analysis.

6.6 Conclusions and Outlook

Liquid sensing has been demonstrated by coupling QCLs to planar AgX waveguides as well as novel GaAs thin-film single-mode waveguides. Measurements with planar AgX waveguides demonstrate the first evanescent field sensing applications of QCLs and measurements with GaAs waveguides demonstrate the first MIR evanescent field measurements with a single-mode waveguide.

Planar AgX evanescent field absorption measurements revealed limits of detection in the range of 80.7 μg for urea and 0.01 μL for acetic anhydride present at the waveguide surface. Limits of detection would be significantly decreased with laser emissions better matched to selective molecular absorption features.

Evanescent field absorption measurements with newly fabricated GaAs single-mode waveguides reveal a five times increase in sensitivity in contrast to multimode silver halide waveguides. These waveguides also give a well-defined evanescent field at the waveguide surface leading to improved quantitative measurements. The evanescent field profile shows a high intensity at the waveguide surface with a sharp decrease into the surrounding material making these waveguides ideal for sensitive and quantitative measurements of monolayer films deposited on the waveguide.

The planar IR waveguides developed in this work show substantial promise toward on-chip infrared chemical sensing platforms combining a single mode-matched thin film

waveguide ideally grown on the same substrate as the QCL for highly integrated MIR liquid phase sensing platforms.

REFERENCES

1. Krska, R.; Taga, K.; Kellner, R., New Ir Fiber-Optic Chemical Sensor for in Situ Measurements of Chlorinated Hydrocarbons in Water. *Applied Spectroscopy* **1993**, *47*, 1484.
2. Mizaikoff, B.; Goebel, R.; Krska, R.; Taga, K.; Kellner, R.; Tacke, M.; Katzir, A., Infrared Fiber-Optical Chemical Sensors with Reactive Surface Coatings. *Sensors and Actuators, B: Chemical* **1995**, *29*, (1-3), 58-63.
3. Walsh, J. E.; MacCraith, B. D.; Meany, M.; Vos, J. G.; Regan, F.; Lancia, A.; Artjushenko, S., Sensing of Chlorinated Hydrocarbons and Pesticides in Water Using Polymer Coated Mid-Infrared Optical Fibers. *Analyst* **1996**, *121*, 789.
4. Michel, K.; Bureau, B.; Boussard-Pledel, C.; Jouan, T.; Adam, J. L.; Staubmann, K.; Baumann, T., Monitoring of Pollutant in Wastewater by Infrared Spectroscopy Using Chalcogenide Glass Optical Fibers. *Sensors and Actuators, B: Chemical* **2004**, *B101*, (1-2), 252-259.
5. Karlowatz, M.; Kraft, M.; Mizaikoff, B., Simultaneous Quantitative Determination of Benzene, Toluene, and Xylenes in Water Using Mid-Infrared Evanescent Field Spectroscopy. *Analytical Chemistry* **2004**, *76*, (9), 2643-2648.
6. Janotta, M.; Vogt, F.; Voraberger, H.-S.; Waldhauser, W.; Lackner, J. M.; Stotter, C.; Beutl, M.; Mizaikoff, B., Direct Analysis of Oxidizing Agents in Aqueous Solution with Attenuated Total Reflectance Mid-Infrared Spectroscopy and Diamond-Like Carbon Protected Waveguides. *Analytical Chemistry* **2004**, *76*, (2), 384-391.
7. Regan, F.; Meaney, M.; Vos, J. G.; MacCraith, B. D.; Walsh, J. E., Determination of Pesticides in Water Using Atr-Ftir Spectroscopy on Pvc/Chloroparaffin Coatings. *Analytica Chimica Acta* **1996**, *334*, (1-2), 85-92.
8. Krska, R.; Kellner, R.; Schiessl, U.; Tacke, M.; Katzir, A., Fiber Optic Sensor for Chlorinated Hydrocarbons in Water Based on Infrared Fibers and Tunable Diode Lasers. *Applied Physics Letters* **1993**, *63*, (14), 1868-70.
9. Goebel, R.; Seitz, R. W.; Tomellini, S. A.; Krska, R.; Kellner, R., Infrared Attenuated Total Reflection Spectroscopic Investigations of the Diffusion Behavior of Chlorinated Hydrocarbons into Polymer Membranes. *Vibrational Spectroscopy* **1995**, *8*, (2), 141-9.

10. Jakusch, M.; Mizaikoff, B.; Kellner, R.; Katzir, A., Towards a Remote Ir Fiber-Optic Sensor System for the Determination of Chlorinated Hydrocarbons in Water. *Sensors and Actuators, B: Chemical* **1997**, B38, (1-3), 83-87.
11. Kastner, J. F.; Tacke, M.; Katzir, A.; Edl-Mizaikoff, B.; Goebel, R.; Kellner, R., Optimizing the Modulation for Evanescent-Wave Analysis with Laser Diodes (Ewald) for Monitoring Chlorinated Hydrocarbons in Water. *Sensors and Actuators, B: Chemical* **1997**, B38, (1-3), 163-170.
12. Janotta, M.; Katzir, A.; Mizaikoff, B., Sol-Gel-Coated Mid-Infrared Fiber-Optic Sensors. *Applied Spectroscopy* **2003**, 57, (7), 823-828.
13. Kraft, M.; Mizaikoff, B., A Mid-Infrared Sensor for Monitoring of Chlorinated Hydrocarbons in the Marine Environment. *International Journal of Environmental Analytical Chemistry* **2000**, 78, (3-4), 367-383.
14. Kraft, M.; Karlowatz, M.; Mizaikoff, B.; Stuck, R.; Steden, M.; Ulex, M.; Amann, H., Sensor Head Development for Mid-Infrared Fiber-Optic Underwater Sensors. *Measurement Science and Technology* **2002**, 13, (8), 1294-1303.
15. Kraft, M.; Jakusch, M.; Karlowatz, M.; Katzir, A.; Mizaikoff, B., New Frontiers for Mid-Infrared Sensors: Towards Deep Sea Monitoring with a Submarine Ft-Ir Sensor System. *Applied Spectroscopy* **2003**, 57, (6), 591-599.
16. Voraberger, H.; Ribitsch, V.; Janotta, M.; Mizaikoff, B., Application of Mid-Infrared Spectroscopy: Measuring Hydrogen Peroxide Concentrations in Bleaching Baths. *Applied Spectroscopy* **2003**, 57, (5), 574-579.
17. deHaseth, J. A.; Andrews, J. E.; McClusky, J. V.; Priester, R. D.; Harthcock, M. A.; Davis, B. L., Characterization of Polyurethane Foams by Mid-Infrared Fiber/Ft-Ir Spectrometry. *Applied Spectroscopy* **1993**, 47, 173.
18. Beyer, T.; Hahn, P.; Hartwig, S.; Konz, W.; Scharring, S.; Katzir, A.; Steiner, H.; Jakusch, M.; Kraft, M.; Mizaikoff, B., Mini Spectrometer with Silver Halide Sensor Fiber for in Situ Detection of Chlorinated Hydrocarbons. *Sensors and Actuators, B: Chemical* **2003**, B90, (1-3), 319-323.
19. Mizaikoff, B., Infrared Optical Sensors for Water Quality Monitoring. *Water Science and Technology* **2003**, 47, (2, Automation in Water Quality Monitoring), 35-42.
20. Karlowatz, M. From the Lab to the Field - Recent Developments in Polymer Coated Atr Sensing for the Determination of Volatile Organic Compounds. Georgia Institute of Technology, Atlanta, GA, 2004.

21. Murphy, B.; McLoughlin, P., Determination of Chlorinated Hydrocarbon Species in Aqueous Solution Using Teflon Coated Atr Waveguide/Ftir Spectroscopy. *International Journal of Environmental Analytical Chemistry* **2003**, 83, (7-8), 653-662.
22. Acha, v.; Meurens, M.; Naveau, H.; Agathos, S. N., Atr-Ftir Sensor Development for Continuous on-Line Monitoring of Chlorinated Aliphatic Hydrocarbons in a Fixed-Bed Bioreactor. *Biotechnology and Bioengineering* **2000**, 68, (5), 473-487.
23. Yang, J.; Hon, H.-H., Infrared Chemical Sensor for Detection of Chlorinated Phenols in Aqueous Solutions on a Atr Waveguide Coated with Structural Designed Polymers. *Journal of the Chinese Chemical Society* **2001**, 48, (2), 159-166.
24. Yang, J.; Lin, H.-C., Ir Chemical Sensor for Detection of Chlorinated Anilines in Aqueous Solutions Based on Atr Waveguides Coated with Derivatized Polystyrene. *Analyst* **2000**, 125, (9), 1605-1610.
25. Taga, K.; Kellner, R.; Kainz, U.; Sleytr, U. B., In Situ Attenuated Total Reflectance Ft-Ir Analysis of an Enzyme-Modified Mid-Infrared Fiber Surface Using Crystalline Bacterial Surface Proteins. *Analytical Chemistry* **1994**, 66, (1), 35-9.
26. Gotshal, Y.; Ido, A.; Katzir, A., Glucose Measurements in Solutions Using Fiberoptic Evanescent Wave Spectroscopy and Tunable Co2 Laser. *Proc. SPIE* **1998**, 3262, 192-196.
27. Spielvogel, J.; Lobik, L.; Nissenkorn, I.; Hibst, R.; Gotshal, Y.; Katzir, A., Cancer Diagnostic Using Fourier Transform Fiberoptic Infrared Evanescent Wave Spectroscopy (Ftir-Fews). *Proc. SPIE* **1998**, 3262, 185-191.
28. Plunkett, S. E.; Jonas, R. E.; Braiman, M. S., Vibrational Spectra of Individual Millimeter-Size Membrane Patches Using Miniature Infrared Waveguides. *Biophysical Journal* **1997**, 73, (4), 2235-2240.
29. Diem, M.; Boydston-White, S.; Chiriboga, L., Infrared Spectroscopy of Cells and Tissues: Shining Light onto a Novel Subject. *Applied Spectroscopy* **1999**, 53, 248A.
30. Goormaghtigh, E.; Raussens, V.; Ruyschaert, J., Attenuated Total Reflection Infrared Spectroscopy of Proteins and Lipids in Biological Membranes. *Biochimica et Biophysica Acta* **1999**, 1422, 105.
31. Bindig, U.; Meinke, M.; Gersonde, I.; Spector, O.; Vasserman, I.; Katzir, A.; Muller, G., Ir-Biosensor: Flat Silver Halide Fiber for Bio-Medical Sensing? *Sensors and Actuators, B: Chemical* **2001**, B74, (1-3), 37-46.

32. Binding, U.; Gersonde, I.; Meinke, M.; Becker, Y.; Muller, G., Fibre-Optic Ir-Spectroscopy for Biomedical Diagnostics. *Spectroscopy* **2003**, 17, 323.
33. Kerslake, E. D. S.; Wilson, C. G., Pharmaceutical and Biomedical Applications of Fiber Optic Biosensors Based on Infra Red Technology. *Advanced Drug Delivery Reviews* **1996**, 21, 205-231.
34. Schmitt, J.; Beekes, M.; Brauer, A.; Udelhoven, T.; Lasch, P.; Naumann, D., Identification of Scrapie Infection from Blood Serum by Fourier Transform Infrared Spectroscopy. *Analytical Chemistry* **2002**, 74, 3865-3868.
35. Lasch, P.; Schmitt, J.; Beekes, M.; Udelhoven, T.; Eiden, M.; Fabian, H.; Petrich, W.; Naumann, D., Antemortem Identification of Bovine Spongiform Encephalopathy from Serum Using Infrared Spectroscopy. *Analytical Chemistry* **2003**, 75, 6673-6678.
36. Martin, T. C.; Moecks, J.; Belousov, A.; Cawthraw, S.; Dolenko, B.; Eiden, M.; von Frese, J.; Koehler, W.; Schmitt, J.; Somorjai, R.; Udelhoven, T.; Verzhakov, S.; Petrich, W., Classification of Signatures of Bovine Spongiform Encephalopathy in Serum Using Infrared Spectroscopy. *Analyst* **2004**, 129, 897-901.
37. Gallego-Nicasio, J.; Lopez-Rodriguez, G.; Martinez, R.; Tarancon, M. J.; Fraile, M. V.; Carmona, P., Structural Changes of Low Density Lipoproteins with Cu²⁺ and Glucose Induced Oxidation. *Biopolymers (Biospectroscopy)* **2003**, 72, (514-520).
38. Vigano, C.; Ruyschaert, J.; Goormaghtigh, E., Sensor Applications of Attenuated Total Reflection Infrared Spectroscopy. *Talanta* **2005**, 65, 1132-1142.
39. Karlowatz, M.; Kraft, M.; Eitenberger, E.; Mizaikoff, B.; Katzir, A., Chemically Tapered Silver Halide Fibers: An Approach for Increasing the Sensitivity of Mid-Infrared Evanescent Wave Sensors. *Applied Spectroscopy* **2000**, 54, (11), 1629-1633.
40. Le Coq, D.; Michel, K.; Fonteneau, G.; Hocde, S.; Boussard-Pledel, C.; Lucas, J., Infrared Chalcogen Glasses: Chemical Polishing and Fiber Remote Spectroscopy. *International Journal of Inorganic Materials* **2001**, 3, (3), 233-239.
41. MacDonald, S.; Michel, K.; LeCoq, D.; Boussard-Pledel, C.; Bureau, B., Optical Analysis of Infrared Spectra Recorded with Tapered Chalcogenide Glass Fibers. *Optical Materials (Amsterdam, Netherlands)* **2004**, 25, (2), 171-178.
42. Plunkett, S. E.; Propst, S.; Braiman, M. S., Supported Planar Germanium Waveguides for Infrared Evanescent-Wave Sensing. *Applied Optics* **1997**, 36, (18), 4055-4061.

43. Vongsvivut, J.; Shilov, S. V.; Ekgasit, S.; Braiman, M. S., Symmetrically Tapered <30-Mm-Thick Quasi-Planar Germanium Waveguides as Chemical Sensors for Microanalysis. *Applied Spectroscopy* **2002**, 56, (12), 1552-1561.
44. Vongsvivut, J.; Fernandez, J.; Ekgasit, S.; Braiman, M. S., Characterization of Supported Cylinder-Planar Germanium Waveguide Sensors with Synchrotron Infrared Radiation. *Applied Spectroscopy* **2004**, 58, (2), 143-151.
45. McCabe, S.; MacCraith, B. D., Novel Mid-Infrared as a Source for Optical Fiber Gas Sensing. *Electronics Letters* **1993**, 29, (19), 1719-1721.
46. Lendl, B.; Frank, J.; Schindler, R.; Mueller, A.; Beck, M.; Faist, J., Mid-Infrared Quantum Cascade Lasers for Flow Injection Analysis. *Analytical Chemistry* **2000**, 72, (7), 1645-1648.
47. Schaden, S.; Haberkorn, M.; Frank, J.; Baena, J. R.; Lendl, B., Direct Determination of Carbon Dioxide in Aqueous Solution Using Mid-Infrared Quantum Cascade Lasers. *Applied Spectroscopy* **2004**, 58, (6), 667-670.
48. Mizaikoff, B., Mid-Infrared Fiber Optic Sensors. Potential and Perspectives. *Proceedings of SPIE-The International Society for Optical Engineering* **1999**, 3849, (Infrared Optical Fibers and Their Applications), 7-18.
49. Mizaikoff, B.; Lendl, B., *Handbook of Fiber Optic Sensing Technology: Principles and Application*. John Wiley & Sons, Ltd.: New York, 2002.
50. Chen, J. Z.; Liu, Z.; Gmachl, C. F.; Sivco, D. L., Silver Halide Fiber-Based Evanescent-Wave Liquid Droplet Sensing with Room Temperature Mid-Infrared Quantum Cascade Lasers. *Optics Express* **2005**, 13, (16), 5953-5960.
51. Harrington, J. A., *Infrared Fibers and Their Applications*. SPIE Press: Bellingham, Washington, 2004.
52. Lopez-Higuera, J. M., *Handbook of Optical Fibre Sensing Technology*. John Wiley and Sons, Ltd.: New York, 2002.
53. Palik, E. D., *Handbook of Optical Constants of Solids*. Academic Press: New York, 1985.
54. Hocde, S.; Boussard-Pledel, C.; Fonteneau, G.; Lucas, J., Chalcogens Based Glasses for Ir Fiber Chemical Sensors. *Solid State Sciences* **2001**, 3, (3), 279-284.
55. Le Neindre, L.; Smektala, F.; Le Foulgoc, K.; Zhang, X. H.; Lucas, J., Tellurium Halide Optical Fibers. *Journal of Non-Crystalline Solids* **1998**, 242, (2,3), 99-103.

56. Sa'ar, A.; Moser, F.; Akselrod, S.; Katzir, A., Infrared Optical Properties of Polycrystalline Silver Halide Fibers. *Applied Physics Letters* **1986**, 49, (6), 305-7.
57. Nagli, L.; Bunimovich, D.; Shmilevich, A.; Kristianpoller, N.; Katzir, A., Optical Properties of Mixed Silver Halide Crystals and Fibers. *Journal of Applied Physics* **1993**, 74, (9), 5737-41.
58. Hahn, P.; Tacke, M.; Jakusch, M.; Mizaikoff, B.; Spector, O.; Katzir, A., Detection of Hydrocarbons in Water by Mir Evanescent-Wave Spectroscopy with Flattened Silver Halide Fibers. *Applied Spectroscopy* **2001**, 55, (1), 39-43.

CHAPTER 7

CONCLUSION AND OUTLOOK

The objective of this thesis was the development of sensing systems, which demonstrate the full potential of quantum cascade lasers for mid-infrared spectroscopy and sensing on miniaturized platforms. QCLs have been demonstrated for both gas and liquid phase sensing in highly integrated and optimized systems.

7.1 Gas Sensing Summary

The application of QCLs to gas sensing in this work includes the demonstration of gas sensing inside conventional hollow waveguides, and inside photonic bandgap waveguides (Chapter 4). Gas sensing inside a photonic bandgap material has been demonstrated for the first time in the course of this thesis.

Proof-of-concept gas sensing systems developed in this work have demonstrated remarkable sensitivities in the low ppb range, fast response times (8 s), and very small sample volumes (1.5 mL). These properties allow the system to meet the criteria needed for medical breath diagnostics and environmental trace sensing applications.

7.2 Liquid Sensing Summary

The liquid sensing applications in this work demonstrate the first evanescent field measurements with a quantum cascade laser (chapter 6), which are a particularly useful for trace environmental and biomedical analysis.

Resulting from the needs in liquid phase QCL based evanescent field sensing, a new generation of IR waveguides was developed and characterized providing single-mode thin-film waveguides for evanescent field sensing grown by molecular beam epitaxy (chapters 5 and 6). In combination with these waveguides, the first MIR evanescent field sensing experiments with QCL and single-mode waveguides were demonstrated.

This sensing system enabled measuring μL volumes of liquid at the waveguide surface reaching critical sensitivities for applications in environmental groundwater trace analysis and for biological measurements such as e.g. protein conformational studies. Furthermore, GaAs thin-film waveguides developed and characterized in this work show particularly high sensitivities at the waveguide surface and a well-controlled evanescent field intensity leading to substantial potential for IR monolayer sensing applications such as the label free detection of protein and DNA.

7.3 Outlook for QCLs in Chemical Sensing

The first QCL was demonstrated in 1994, and after nearly a decade of development the technology is well established with lasers providing sufficient power (tens of mW average power) and narrow linewidths (> 150 MHz) for chemical sensing applications.

Lasers have been extensively demonstrated in both gas and liquid chemical sensing applications as discussed in chapters 4 and 6. However, due to a lack of commercial availability of lasers at a large selection of wavelengths, they have not been applied to wide variety of target analytes. Rather, these systems have been utilized as a chemical sensing proof-of-concept demonstration.

The field of QCL-based chemical sensing is currently in a critical phase of development. From an application perspective, the lack of availability of lasers makes molecule (target) specific applications difficult to demonstrate. However, from a fabrication perspective a demonstration of specific applications is crucial to guide the selection of wavelengths produced by QCL manufacturers. The field is in critical need of a “killer application”, which would allow lasers to be produced at useful wavelengths in large quantities making the technology less expensive. However, as lasers operating at wavelengths which overlap an absorption band in the analyte of interest are crucial to the demonstration of specific application, this problems parallels the “chicken and egg” syndrome. Which comes first – the application, or the lasers?

The proof-of-concept systems presented in this work represent a key step in advancing the field of QCL-based chemical sensors. Sensing systems demonstrated are able to achieve ppb sensitivities with fast response times (s) and small sample volumes (mL for gas and μL for liquids) needed for target applications in medical breath diagnostics, atmospheric monitoring, environmental groundwater monitoring, and biological protein analysis. These demonstrations bring the field of QCL-based chemical sensors closer to finding the “killer application”.

The next step in this dynamic research field would be to obtain lasers that match absorption bands for useful analytes in the target applications such as acetone, formaldehyde, and isoprene for breath diagnostics or benzene, toluene, ethylbenzene, and xylene for ground and drinking water trace monitoring. Lasers at these wavelengths can be substituted into the systems and technology developed in this work to demonstrate sensor systems with a large market demanding the enabling lasers technology to be produced at the quantity levels needed to reduce the laser source and overall sensor system costs. Continuous progress in this direction will translate QCL-based chemical sensor technology into mainstream applications, and allow the field to diversify into a prosperous future in chemical sensing.

After a decade of establishing QCLs as the future dominant light source in the mid-infrared regime, the next decade will be characterized by the establishment of useful chemical and biological sensing applications, along with compact and highly integrated device platforms which take full advantage of this technology.

APPENDIX A

MATLAB PROGRAMS FOR BPM SIMULATIONS

Program to calculate the intensity in the evanescent field:

```
Format short
[M] = xl2mat (name, 256, 1038)
wgsectiontop = find (M(:,1) < - wgloop & M(:,1) > (-wgloop - 0.000006))
wgbound1a = wgsectiontop (1,1)
wgbound1b = wgsectiontop (size(wgsectiontop(:,1),1))
inwg = find (M(:,1) > -wgloop & M(:,1) < wgloop)
inwg1 = inwg (2,1)
inwg2 = inwg (size(inwg(:,1),1))
zmat = 0
for x = 1:1:size(M(1,:),2), zmat(x) = M(1,x); end;
zmatsection = find (zmat > 0.005 & zmat < 0.025)
zmatlower = zmatsection (1,1)
zmatupper = zmatsection(1,size(zmatsection(1,:),2));
for count = zmatlower:1:zmatupper, count1 = count - zmatlower + 1, pevan(count1) =
100*trapz(M(wgbound1a:wgbound1b,1), M(wgbound1a:wgbound1b,
count))/trapz(M(inwg1:inwg2,1),M(inwg1:inwg2,count));
end
avg = mean(pevan);
clear wgsectiontop;
clear wgbound1a;
clear wgbound1b;
clear inwg
clear inwg1
clear inwg2;
```

contents of xl2mat.m:

```
function [data]=XL2MAT(nom,row,col)

'FILE IS BEING CONVERTED'

cd C:\Documents and Settings\Christy\Desktop;
fid=fopen(nom);
for ii=1:col;
for jj=1:row;
data(jj,ii)=fscanf(fid,'%e',1);
end;
end;
fclose(fid);
cd C:\Documents and Settings\Christy\Desktop\matlab;
```


Program to calculate to total power transmitted through the waveguide:

```
[M] = power('1.txt', 2, 1200)
```

```
wgsectiontop = find(M(:,1) < - 0.00005)
```

```
wgbound1 = size(wgsectiontop(:,1),1)+1
```

```
wgsectionbot = find(M(:,1) > 0.00005)
```

```
wgbound2 = wgsectionbot(1,1)
```

```
M(wgbound1:wgbound2 -1,1)
```

```
wgpower = trapz(M(wgbound1:wgbound2,1),M(wgbound1:wgbound2,2))
```